

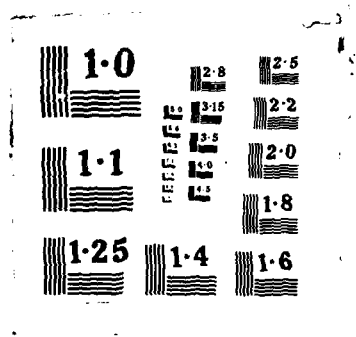
AD-A168 003

DEVELOPMENT OF FRACTURE MECHANICS MAPS FOR COMPOSITE
MATERIALS VOLUME 2(0) DEUTSCHE FORSCHUNGS- UND
VERSUCHSANSTALT FUER LUFT- UND RAUMF... H W BERGMANN
DEC 85 AFMAL-TR-85-4150-VOL-2 F/G 11/4

1/3

UNCLASSIFIED

NL



AD-A168 003

AFWAL-TR-85-4150
Volume 2

DEVELOPMENT OF FRACTURE MECHANICS MAPS
FOR COMPOSITE MATERIALS

Dr. H. W. Bergmann

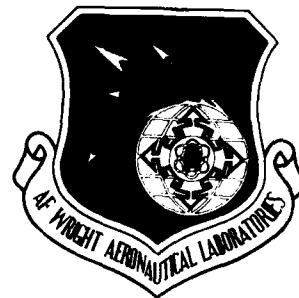
DFVLR - Institute for Structural Mechanics
Braunschweig, West Germany

December 1985

Final Report for Period January 1982 - January 1985

Approved for public release; distribution unlimited.

MATERIALS LABORATORY
AIR FORCE WRIGHT AERONAUTICAL LABORATORIES
AIR FORCE SYSTEMS COMMAND
WRIGHT-PATTERSON AIR FORCE BASE, OHIO



DTIC FILE COPY

ASD 86 Q926

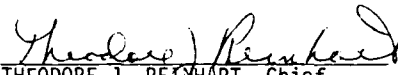
NOTICE

When Government drawings, specifications, or other data are used for any purpose other than in connection with a definitely related Government procurement operation, the United States Government thereby incurs no responsibility nor any obligation whatsoever; and the fact that the government may have formulated, furnished, or in any way supplied the said drawings, specifications, or other data, is not to be regarded by implication or otherwise as in any manner licensing the holder or any other person or corporation, or conveying any rights or permission to manufacture use, or sell any patented invention that may in any way be related thereto.

This report has been reviewed by the Office of Public Affairs (ASD/PA) and is releasable to the National Technical Information Service (NTIS). At NTIS, it will be available to the general public, including foreign nations.

This technical report has been reviewed and is approved for publication.

FOR THE COMMANDER


THEODORE J. REIXHART, Chief
Materials Engineering Branch
Systems Support Division

UNCLASSIFIED

SECURITY CLASSIFICATION OF THIS PAGE

REPORT DOCUMENTATION PAGE				
1. REPORT SECURITY CLASSIFICATION UNCLASSIFIED		1b. RESTRICTIVE MARKINGS NONE		
2a. SECURITY CLASSIFICATION AUTHORITY N/A		3. DISTRIBUTION/AVAILABILITY OF REPORT Approved for Public Release Distribution unlimited		
2b. DECLASSIFICATION/DOWNGRADING SCHEDULE N/A				
4. PERFORMING ORGANIZATION REPORT NUMBER(S) None		5. MONITORING ORGANIZATION REPORT NUMBER(S) AFWAL-TR-85-4150, Vol 2		
5a. NAME OF PERFORMING ORGANIZATION DFVLR - Institute for Structural Mechanics		5b. OFFICE SYMBOL (If applicable) N/A		7a. NAME OF MONITORING ORGANIZATION AFWAL/Materials Laboratory (AFWAL/MLSE)
6a. ADDRESS (City, State and ZIP Code) Braunschweig, West Germany		7b. ADDRESS (City, State and ZIP Code) Wright-Patterson AFB, OH 45433		
8a. NAME OF FUNDING/SPONSORING ORGANIZATION European Space Technology Comm		8b. OFFICE SYMBOL (If applicable) N/A		9. PROCUREMENT INSTRUMENT IDENTIFICATION NUMBER ESTEC/Contract No 4825/81/ML/AK(SC)
8c. ADDRESS (City, State and ZIP Code) Brussels, Belgium		10. SOURCE OF FUNDING NOS.		
		PROGRAM ELEMENT NO.	PROJECT NO.	TASK NO.
		N/A	N/A	N/A
11. TITLE (Include Security Classification) Development of Fracture Mechanics Maps for Composite Materials				
12. PERSONAL AUTHOR(S) Editor (Dr. H. W. Bergmann)				
13a. TYPE OF REPORT Final		13b. TIME COVERED FROM Jan 82 TO Jan 85		14. DATE OF REPORT (Yr., Mo., Day) 1985 Dec
15. PAGE COUNT see below (16)				
16. SUPPLEMENTARY NOTATION Vol 1 (216) Vol 2 (204) Vol 3 (265) Vol 4 (192)				
17. COSATI CODES			18. SUBJECT TERMS (Continue on reverse if necessary and identify by block number)	
FIELD	GROUP	SUB. GR.		
11	04		Fiber Reinforced Composites, Dynamic Test, Thermal Cycling,	
01	03		Quality Control, Static Test, Stress Concentrations	
19. ABSTRACT (Continue on reverse if necessary and identify by block number) The Institute for Structural Mechanics of the German Aerospace Research Establishment (DFVLR) has conducted a research program aimed at the characterization of the fracture behavior of carbon-fiber-reinforced epoxy resins. The research effort encompassed a comprehensive experimental and analytical investigation of the response of test specimens under a broad range of material, loading and environmental parameters. By combining an evaluation of global laminate properties with an investigation of micro- and macroscopic modes of failure, the understanding of the fracture and fatigue behavior of carbonfiber-reinforced composites was enhanced. It is expected that the results of the research program and their representation in the form of tables, figures, graphs and maps will assist the design engineer and lead to improved engineering concepts.				
20. DISTRIBUTION/AVAILABILITY OF ABSTRACT UNCLASSIFIED/UNLIMITED <input checked="" type="checkbox"/> SAME AS RPT. <input type="checkbox"/> DTIC USERS <input type="checkbox"/>			21. ABSTRACT SECURITY CLASSIFICATION UNCLASSIFIED	
22a. NAME OF RESPONSIBLE INDIVIDUAL THEODORE J. REINHART			22b. TELEPHONE NUMBER (Include Area Code) 513/255-3691	22c. OFFICE SYMBOL AFWAL/MLSE

DD FORM 1473, 83 APR

EDITION OF 1 JAN 73 IS OBSOLETE.

SECURITY CLASSIFICATION OF THIS PAGE

DEVELOPMENT OF FRACTURE MECHANICS MAPS
FOR COMPOSITE MATERIALS

Final Report

ESTEC/Contract No. 4825/81/NL/AK(SC)

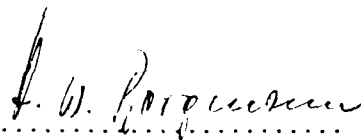
Compiled and
Edited by:

Dr. H.W. Bergmann, DFVLR

ESA Technical
Management:

Dr. C. Stavrinidis, ESTEC

Authorized by:


.....

Dr. H.W. Bergmann
Director, Institute for
Structural Mechanics, DFVLR

January 1985

GERMAN AEROSPACE RESEARCH ESTABLISHMENT (DFVLR)

ABSTRACT

The Institute for Structural Mechanics of the German Aerospace Research Establishment (DFVLR) has conducted a research program aimed at the characterization of the fracture behavior of carbon-fiber-reinforced epoxy resins. The research effort encompassed a comprehensive experimental and analytical investigation of the response of test specimens under a broad range of material, loading and environmental parameters. By combining an evaluation of global laminate properties with an investigation of micro- and macroscopic modes of failure, the understanding of the fracture and fatigue behavior of carbonfiber-reinforced composites was enhanced. It is expected that the results of the research program and their representation in the form of tables, figures, graphs and maps will assist the design engineer and lead to improved engineering concepts. Volume 2 includes the following.

STUDY MANAGEMENT

The research program involved a wide range of different disciplines and required the definition and coordination of a large number of subtasks. Dr. H.W. Bergmann, director of the DFVLR Institute for Structural Mechanics, served as Program Manager for the entire duration of the program from January 1982 to December 1984 and compiled and edited the final report.

ACKNOWLEDGEMENTS

The DFVLR Research Team acknowledges the assistance of ESTEC personnel in the conduct of the research program and in maintaining current awareness of ongoing developments in this field. Special appreciation is due the ESTEC Contract Manager, Dr. C. Stavriniadis, who conceived the request for proposal, supervised the contractual performance and provided helpful guidance at critical

stages of the research program. In this context the assistance through Engineering Systems International (ESI), supporting some of the analytical aspects of the contract, is specially appreciated.

The Program Manager acknowledges the responsiveness and cooperation of the numerous scientists and technicians, of the Institute for Structural Mechanics in the pursuit of the overall research effort. Appreciation is also expressed to the Section Heads of the Institute for Structural Mechanics Dr. Geier, Dr. Prinz and Dr. Niederstadt for their supervisory activities, and to the secretarial and drafting staff for the preparation of the document.

The authors of the individual sections of the final report are listed below:

Executive Summary : Dr.-Ing. H.W. Bergmann

Technical Report,

- Section 1 : Dr.-Ing. H.W. Bergmann
- Section 2 : Dr.-Ing. R. Prinz, Dipl.-Ing. K. Schmidt
- Section 3 : Dipl.-Ing. M. Gädke
- Section 4 : Dipl.-Ing. R. Schütze, Dipl.-Phys. J. Block
- Section 5 : Dr.-Ing. H. Eggers, Dipl.-Ing. L. v. Bonin
- Section 6 : Dipl.-Ing. M. Gädke
- Section 7 : Dr.-Ing. L. Kirschke, Dr.-Ing. H. Eggers
- Section 8 : Dipl.-Phys. H.C. Goetting
- Section 9 : Dipl.-Ing. G. Kress, Dr.-Ing. L. Kirschke
- Section 10 : Dipl.-Ing. W. Hartung
- Section 11 : Dipl.-Ing. H. Twardy, Dipl.-Phys. J. Block
- Section 12 : Dr.-Ing. G. Niederstadt
- Section 13 : Dipl.-Phys. P. Nitsch
- Section 14 : Dr.-Ing. H. Eggers, Dr.-Ing. K. Rohwer
- Section 15 : Dr. J. Awerbuch
- Section 16 : Dr.-Ing. R. Prinz

This Report consists of four Volumes:

- Volume 1 - I. Executive Summary
II. Technical Report (Sections 1 - 8)
- Volume 2 - II. Technical Report (Sections 9 - 16)
- Volume 3 - Appendices A - E
- Volume 4 - Appendices F - K

VOLUME 1 - CONTENTS

I. EXECUTIVE SUMMARY

II. TECHNICAL REPORT

1. INTRODUCTION

- 1.1 State of the Art
- 1.2 Scope of Research Program
- 1.3 Documentation of Results

2. TEST FACILITIES

- 2.1 Summary
- 2.2 Thermal Cycling Facility
- 2.3 Static Test Machine
- 2.4 Servohydraulic Test Machines
- 2.5 Environmental Simulation

3. TEST SPECIMENS

- 3.1 Summary
- 3.2 Quality Control
- 3.3 Manufacturing Process
- 3.4 Traceability

Accession For	
NTIS GRA&I	<input checked="checked" type="checkbox"/>
DTIC TAB	<input type="checkbox"/>
Unannounced	<input type="checkbox"/>
Justification	
By	
Distribution/	
Availability Codes	
Dist	Avail and/or Special
A11	



4. NONDESTRUCTIVE EVALUATION

- 4.1 Summary
- 4.2 Radiography
- 4.3 Ultrasonic Techniques
- 4.4 Acoustic Emission Analysis
- 4.5 Grating Reflection Techniques
- 4.6 References

5. ANALYSIS TOOLS

- 5.1 Summary
- 5.2 Statistical Data Treatment
- 5.3 Computer Program ASKA
- 5.4 Computer Program LAMINA
- 5.5 References

6. RESPONSE OF STATICALLY TESTED UN-NOTCHED SPECIMENS

- 6.1 Summary
- 6.2 Test Program
- 6.3 Influence of Moisture
- 6.4 Influence of Temperature
- 6.5 Properties of Unidirectional Laminates
- 6.6 Properties of Crossplied Laminates
- 6.7 Interlaminar Shear Tests
- 6.8 Prediction of Properties of Multidirectional Laminates
- 6.9 Mechanisms of Damage
- 6.10 References

7. RESPONSE OF STATICALLY TESTED NOTCHED SPECIMENS

- 7.1 Summary
- 7.2 Test Program
- 7.3 Types of Damage Progression
- 7.4 Characteristic Quantities
- 7.5 Analytical Approach
- 7.6 Results of Analysis
- 7.7 Observations
- 7.8 References

8. RESPONSE OF MECHANICALLY FATIGUED UN-NOTCHED SPECIMENS

- 8.1 Summary
- 8.2 Scope of Test Program
- 8.3 Effects of Temperature and Moisture on Fatigue Life
- 8.4 Mechanisms of Damage
- 8.5 References

VOLUME 2 - CONTENTS

Cont'd

9. RESPONSE OF MECHANICALLY FATIGUED NOTCHED SPECIMENS

- 9.1 Summary
- 9.2 Test Program
- 9.3 Unidirectional Laminate with Notches
- 9.4 Multidirectional Laminates with Central Holes
- 9.5 References

10. RESPONSE OF THERMALLY FATIGUED UN-NOTCHED SPECIMENS

- 10.1 Summary
- 10.2 Test Program
- 10.3 Strength and Stiffness Degradations
- 10.4 Mechanisms of Damage
- 10.5 Additional Observations
- 10.6 References

11. STRAIN CAPABILITIES AND STRAIN RATE EFFECTS IN EPOXY RESINS AND LAMINATES

- 11.1 Summary
- 11.2 Material Choice and Test Specimen Configurations
- 11.3 Test Procedure for Epoxy Resins
- 11.4 Test Results for Epoxy Resins
- 11.5 Test Procedure for NOL-Rings
- 11.6 Test Results on Mechanical Properties for NOL-Rings
- 11.7 Test Procedure for Acoustic Emission Analysis
- 11.8 Acoustic Emission Results
- 11.9 References

12. RADIATIVE AND OXIDATIVE EFFECTS

- 12.1 Summary
- 12.2 Effect of Electron Irradiation
- 12.3 Effect of UV-Irradiation
- 12.4 Effect of Oxidation
- 12.5 References

13. FRACTOGRAPHICAL INVESTIGATIONS

- 13.1 Summary
- 13.2 Description of Test Equipment
- 13.3 Investigation of Epoxy Resins
- 13.4 Investigation of Statically Loaded Laminates
- 13.5 Investigation of Dynamically Loaded Laminates
- 13.6 Characteristic Values in Micromechanics
- 13.7 References

14. FRACTURE MECHANICS ASPECTS

- 14.1 Summary
- 14.2 Limits of Fracture Mechanics
- 14.3 Concepts of Damage Mechanics
- 14.4 References

15. EVALUATION OF FRACTURE MODELS

- 15.1 Summary
- 15.2 Discussion of Relevant Fracture Models
- 15.3 Survey of Experimental Data
- 15.4 Correlation between Notch Sensitivity and Fracture Model Parameters
- 15.5 References

16. MECHANISMS OF FRACTURE

- 16.1 Summary
- 16.2 Introduction
- 16.3 Test Procedure
- 16.4 Microcracks
- 16.5 Edge Delaminations
- 16.6 Stress Analysis
- 16.7 Fatigue and Residual Strength Model
- 16.8 Central Delaminations
- 16.9 Fiber Breaks and Fiber Debonds
- 16.10 References

Handwritten notes:
towards Fiber Reinforced Composites
Dynamic tests - fatigue, Cycling, Quasi static
Central static tests, Stress concentration

- viii -

VOLUME 3 - CONTENTS

APPENDIX A

Charakterisierung von Schadensfortschritten in CFK-Laminaten
mittels Schallemissionsanalyse

APPENDIX B

On-Line Measurement of Onset and Growth of Edge Delaminations in
CFRP-Laminates by an Optical Grating Reflection Method

APPENDIX C

Eine effektive Teilstrukturtechnik angewendet auf Bruchprobleme

APPENDIX D

Crack Conditions for Statically Loaded Notched UD-Laminates
of Carbon Fiber Reinforced Plastic. Part 2:
Fitting Curves for the Test Results

APPENDIX E

Einfluss von Temperatur und Feuchte auf die Schwingfestigkeit
ungekerbter CFK - Lamine

VOLUME 4 - CONTENTS

APPENDIX F

Fatigue Response of Notched Graphite-Epoxy Laminates

APPENDIX G

Influence of Simulated Space Environment on Carbon Fiber Reinforced Plastic (CFRP)

APPENDIX H

Notched Strength of Composite Laminates

APPENDIX I

Growth of Delaminations under Fatigue Loading

APPENDIX K

Zur Auswahl eines CFK-Mehrschichtenlaminats für Versuche im Zugbereich

DEVELOPMENT OF FRACTURE MECHANICS MAPS
FOR COMPOSITE MATERIALS

Final Report
- Volume 2 -

II. TECHNICAL REPORT
SECTIONS 9 - 16

9. RESPONSE OF MECHANICALLY FATIGUED NOTCHED SPECIMENS

9.1 Summary

In fiber-reinforced laminates containing notches or holes the formation of cracks and their subsequent progression are caused by stress concentrations in the vicinity of the discontinuities. The residual strength and stiffness of such laminates under cyclic loading was the primary aim of this investigation. In a preparatory study the nature of damage progression in on-axis unidirectional test specimens with two symmetrical edge notches under increasing numbers of load cycles with $R = 0.1$ was determined. The majority of the test effort was conducted with multidirectional laminates containing unloaded circular holes at the center of the test section. Matrix cracks and delaminations in and between adjacent plies of the laminates were observed and monitored by contrast-enhanced radiography. The strength and stiffness measurements after prescribed numbers of load cycles with $R = 0.1$ showed that the global stiffness of the test specimens diminished whereas the residual static strength continued to increase until shortly before failure. The strength increase is attributed to the relief of local stress concentrations due to the crack formation and progression in the plies of the laminate around the hole. A more detailed representation of the investigation of laminates containing circular holes is given in Appendix F "Fatigue Response of Notched Graphite-Epoxy Laminates".

9.2 Test Program

The unidirectional $[0]_g$ -laminates were made of T300/914C material. Two 5 mm deep notches were introduced by diamond saw cuts at the edges of the 50 mm wide and 380 mm long test specimens. For the multidirectional laminates T300/5208 material was used. The test specimens were 36 mm wide, 240 mm long and contained drilled circular holes of 19 mm diameter. Three different stacking orders, namely $[+45, 90, -45, 0]_g$, $[+45, -45, 0, 90]_g$ and $[0, 90, +45, -45]_g$, were investigated.

The fatigue tests were performed in servo-hydraulic test machines at a stress ratio of $R = 0.1$ and with different stress amplitudes and frequencies ranging from 1-10 Hz. For the unidirectional notched specimens the crack initiation, the crack length and the global stiffness were recorded as functions of load cycles. In the case of the multidirectional test specimens the global stiffness and the residual tensile strength were registered after prescribed numbers of load cycles. Most of the specimens were tested to failure in order to obtain life over load level curves. The tests were supported by radiographic and fringe pattern evaluations after different loading intervals.

9.3 Unidirectional Laminate with Notches

The tests aimed to establish the number of load cycles at which the first hairline cracks at the notch tip could be observed, and to relate the length of the subsequently developing matrix crack to the increasing numbers of load cycles. The crack lengths were measured by following the moving crack front with the cross-hairs of a microscope. The results of this study, performed for stress amplitudes from $\sigma_0 = 100 \text{ N/mm}^2$ to $\sigma_0 = 160 \text{ N/mm}^2$, are summarized in Fig. 9.1. The shown crack lengths are sums of the lengths of the two cracks emanating from one of the notch tips. For test technique-related reasons the specimens were cycled with $f=1 \text{ Hz}$ up to 1000 load cycles, and with $f=6 \text{ Hz}$ thereafter. It is apparent from Fig. 9.1 that most of the crack-length curves exhibit a kink at 1000 load cycles indicating that the crack progression may be frequency-dependent. It is also noteworthy that for $\sigma_0 > 120 \text{ N/mm}^2$ the crack initiation occurs already during the initial load cycle. In comparison, in static tests with extremely low loading rates, cracks were not observed for $\sigma_0 < 160 \text{ N/mm}^2$. The conclusion is warranted that crack initiation and progression during cyclic loading may depend on the frequency as well as on the loading rate and on the absolute duration of the test.

Some of the curves in Fig. 9.1 exhibit on occasional horizontal response which is indicative of misaligned fibers acting as temporary crack stoppers.

Fig. 9.2 displays curves of equal crack length as functions of load cycles for different σ_0 . In logarithmic representation they tend to be linear for load cycles larger than 10^2 .

9.4 Multidirectional Laminates with Central Holes

The knowledge of the fatigue response of notched composite laminates is much less complete than that of unnotched laminates. The reason is that the models predicting fatigue damage and residual strength and stiffness of unnotched laminates are based on uniform distributions of damage that are reflected by terms such as characteristic damage state, for instance. These uniformities of damage, however, do not apply to notched specimens. [9.1], [9.2], [9.3].

9.4.1 Initial Properties

The previously mentioned stacking orders of $[+45, 90, -45, 0]_s$, $[+45, -45, 0, 90]_s$ and $[0, 90, +45, -45]_s$ will be referred to as type A-, B- and C-laminates, respectively.

Tensile strength tests were performed on five specimens each of notched A- and B-type laminates and of unnotched C-type laminates. The individual failure loads of the specimens and the average failure loads are represented in Fig. 9.3. The dashed horizontal lines indicate the averaged load levels at which major discontinuities in the strain-load curves, accompanied by strong acoustic emissions, occurred.

Stiffness data were taken from the linear part of the strain-load curves recorded during the tensile strength tests by means of an extensometer centered with respect to the whole. Each vertical line in Fig. 9.4 represents the stiffness of a specimen while the average stiffnesses, based on the area of an unnotched cross-section, are given by the horizontal lines.

A-type specimens loaded at $R = 0.1$ to 80%, and B-type specimen loaded to 70% of their static strength, sustained at least 10^6

loading cycles. Corresponding tensile load versus life curves for the two laminates are shown in Fig. 9.5. A-type specimens cycled at 95%, and B-type specimens cycled at 85% of their static strength survived at least 10^5 cycles [9.4].

9.4.2 Stiffness Degradation

Fig. 9.6 contains stiffness data for B-type laminates cycled at the 85% level. The two curves show the stiffness degradations established by displacement measurements with extensometers of 1.0 in and 3.6 in gage lengths. The stiffness changes based on the former are larger and more nearly realistic unless the damage zone spreads beyond the 1.0 in gage length.

The limits of the indicated regions I, II and III in Fig. 9.6 reflect somewhat arbitrarily transitions in the damage growth process as represented by stiffness changes. In region I, with increasing load cycles the stiffness decreases at a decreasing rate as small matrix cracks develop near the hole. In region II, the stiffness continues to degrade more or less linearly with increasing load cycles. The matrix cracks in the zero and 45-degree plies extend away from the hole while delaminations form in the region damaged by the matrix cracks. Region III begins as the rate of stiffness degradation increases. In this region, the sharp decrease in stiffness is associated with further extension of the cracks in the 45-degree plies, and the growth of the delaminations along the 45-degree matrix cracks. Early in the life of the laminate (region I) the damage is confined to the approximate zone of stress concentration around the hole. In later stages of life, the stresses around the hole are redistributed and the stress concentration around the hole is relaxed due to the growth of the damage zone away from the hole. X-ray records of damaged A- and B-type specimens showing these damage zones are presented in Fig. 9.7 and Fig. 9.8.

Fig. 9.9 shows regions II and III of the stiffness degradation in A- and B-type specimens during fatigue loading at 90% of static failure load. The time axis is logarithmically scaled. In this representation, region II appears as an almost linear line lead-

ing into a sharp knee which connects region II with region III. Immediately behind the knee, the degradation rate appears to be highly increased. At the end of region III, the stiffness decay accelerates again until failure. Comparing the two curves shown in Fig. 9.9, the B-type laminate shows a lower stiffness degradation before the knee, a later and more distinct formation of the knee, and a higher degradation rate after the knee than the A-laminate. The stiffness loss at the end of the fatigue life is 18 percent for the B-type and 40 percent for the A-type specimen.

9.4.3 Residual Strength

A number of the cyclic tests was interrupted at various loading stages for the nondestructive inspection of the damage zone and for residual strength measurements. This series of tests provided the characteristic curves of the change in residual strength throughout the loading history given in Fig. 9.10 for a load level of 85% in the B-type laminates. It is apparent that the actual strength increase depends on the cyclic stress level such that higher stress levels produce slightly higher strength increases than lower stress levels.

During the first few cycles the damage, primarily matrix cracks, reduces the effect of the stress concentrations at the hole. The residual strength increase is on the order 10%.

The second region of the residual strength curves is characterized by a slow, but constant increase in residual strength over a logarithmic cycle scale. At the end of the region II, the increase in residual strength is 15 to 20%. The limits of regions I and II for residual strength are approximately the same as those observed for stiffness changes.

The region III of the residual strength curve is marked by a further increase in strength. Although the data in this region is scant, it appears that the maximum residual strength is reached between 50 and 80% of the specimen lifetime. The largest measured increases in residual strength are 26 and 42% for the A- and B-type laminates, respectively. During the final region of the

fatigue life, the residual strength decreases until the strength equals the level of maximum cyclic stress.

9.4.4 Mechanisms of Damage

Static damage starts with matrix cracks, usually in the surface plies, at ca. 60% of maximum load in the A-type laminates and at ca. 50% in the B-type laminates. At higher load levels cracks appear in all directions. The A-type laminates develop more well-defined 0-degree cracks tangent to the hole while the B-type laminates develop more well-defined 45-degree cracks. 0-degree cracks in the A-type laminate grow to a length of more than five hole diameters. When the tangent 0-degree cracks approach their maximum length, cracks in 45-degree and 90-degree direction are also initiated on the straight edges. In the final stages of lifetime, a regular pattern of matrix cracks is formed between the tangent 0-degree cracks and the straight edges. The uniformity of these cracks is similar to damage patterns observed in unnotched laminates, the so-called characteristic damage state (CDS).

The delamination zone visible in the X-ray records in Fig. 9.7 and Fig. 9.8 consists of the superimposed images of the delaminations between the various laminate interfaces. It seems as if the tangent 0-degree cracks in both the A- and the B-laminates cause delaminations on adjacent interfaces. These delaminations have the largest continuously connected area of all delaminations in the laminates. In general, while the A-type laminates develop a much larger delamination along its tangent 0-degree cracks, the more confined delaminations of the B-type laminates spread along the 45-degree direction and reach the straight edges of the test specimens.

Fig. 9.11 shows the delamination surfaces between layers produced with the aid of the deply technique. The spatial distributions, the characteristic shapes as well as the proper magnitude of the delamination zones are easily recognizable. The extent of the delaminations on all interfaces is higher for A-type specimens than for B-type specimens, which is consistent with the previous

observation that the A-type specimens experienced much higher stiffness losses during their fatigue life.

Fig. 9.12 contains fringe patterns for cycled laminates under a static load. The tangent 0-degree cracks are visible and it can be seen that they have a strong redistribution effect upon the strain field near the hole, resulting in the reduction of the maximum strain concentration in the x-direction at the hole edge. Except for the crack tips, the strain distribution along the cracks is almost uniform.

Fig. 9.13 represents the average strain concentrations as a function of the length of the tangent cracks at various fatigue stages for an A-type specimen. After 6×10^5 cycles, which correspond to approximately 50% of the expected lifetime, the strain concentration is reduced to $K = 1.46$.

Fig. 9.14 shows the decrease of strain concentrations versus the logarithmically scaled number of cycles. The rate of decrease is very high during the first cycles of fatigue loading. Recalling that the rate of increase of residual strength of both laminates is also very high at the beginning of the fatigue life, it seems likely that the tangent 0-degree cracks are a main factor influencing residual strength.

Fig. 9.15 finally shows the results of two strength tests performed on an A-type specimen and on a B-type specimen versus the length of the tangential cracks obtained from X-ray photos taken after applying the fatigue load. Cracks of equal length in A- and B-type specimen seem to influence their strength increases differently. A linear curve fit of the data points indicates strength increases of 23% for the A-type laminat and of 44% for the B-type laminate.

9.5 References

- | | | |
|-------|--|--|
| [9.1] | Ramani, S.V.
Williams, D.P. | Notched and Unnotched Fatigue Behavior of
Angle-Ply Graphite/Epoxy Laminates.
ASTM STP 636 (1977) pp.27-46 |
| [9.2] | Walter, R.W.
Johnson, R.W.
June, R.R.
McCarty, J.E. | Designing for Integrity in Long-Live Com-
posite Aircraft Structures.
ASTM STP 636 (1977) pp. 228-247 |
| [9.3] | Konishi, D.Y.
Lo, K.H. | Flaw Criticality of Graphite/Epoxy Struc-
tures. ASTM STP 696 (1979) pp. 125-144. |
| [9.4] | Kress, G. | Fatigue Response of notched Graphite-Epoxy
Laminates. DFVLR IB-131-84/04 |

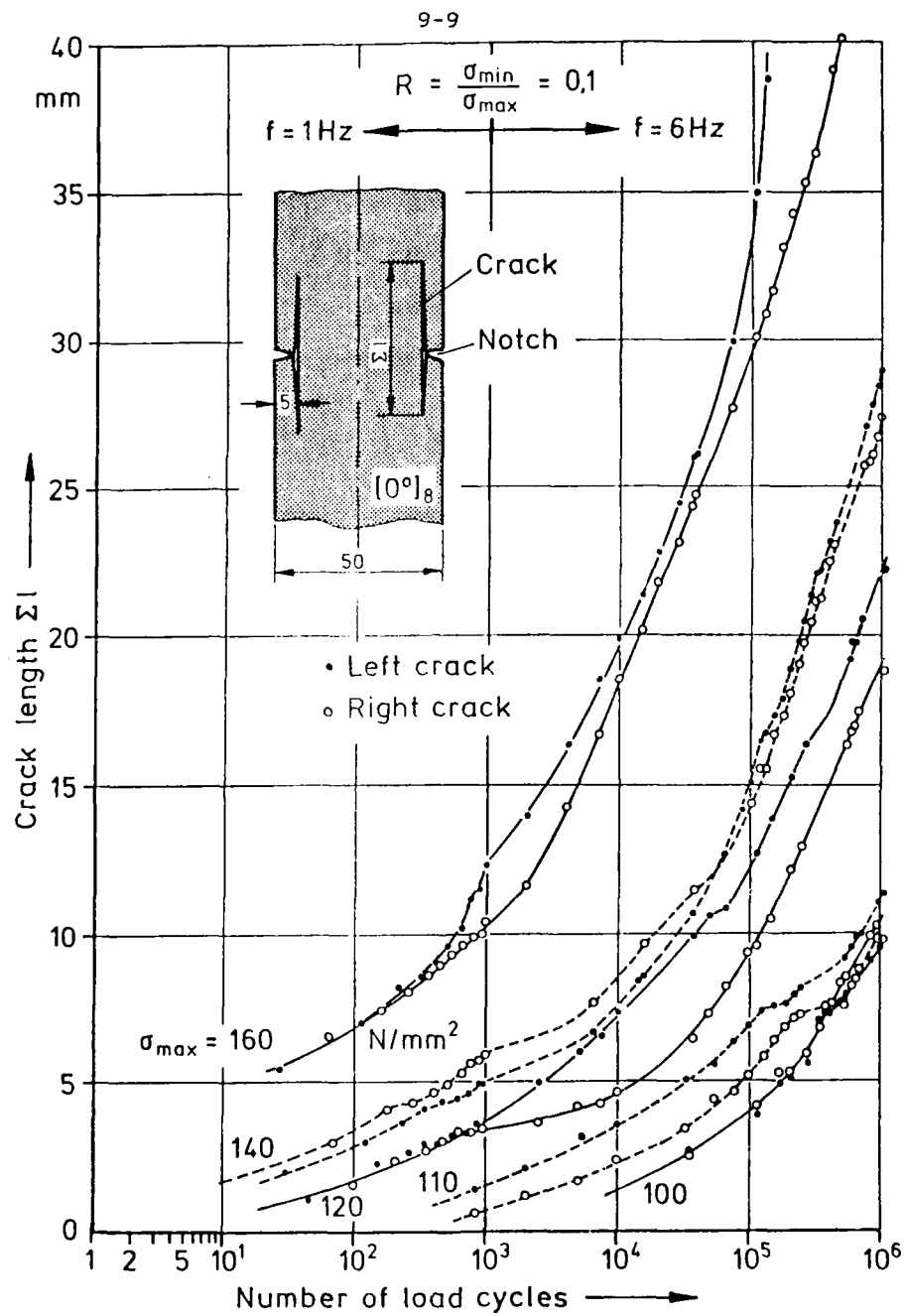


Fig. 9.1 Crack propagation in notched unidirectional CFRE-laminates under tension-tension-fatigue load.

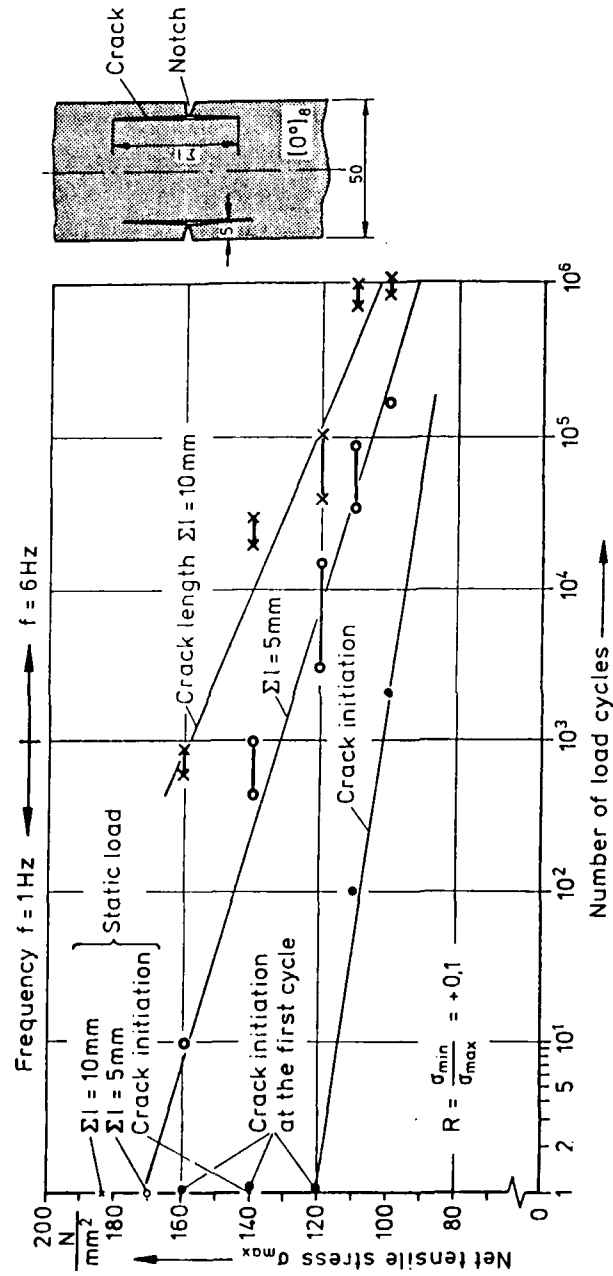


Fig. 9.2 Crack initiation and crack propagation in notched unidirectional CFRE-laminates under static and tension-tension fatigue loads.

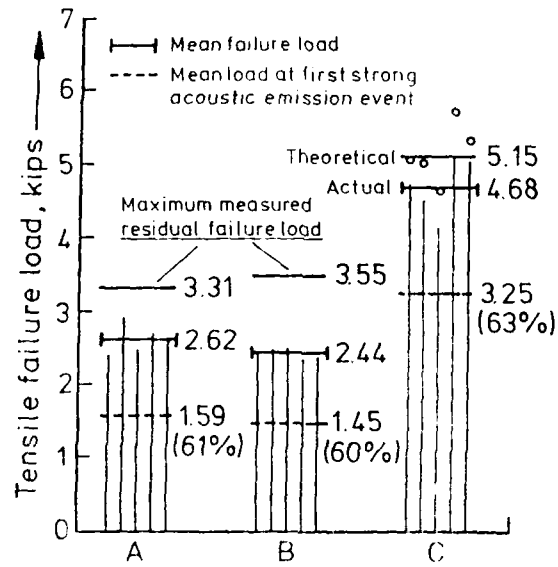


Fig. 9.3 Individual and average failure loads of A-, B- and C-type laminates.

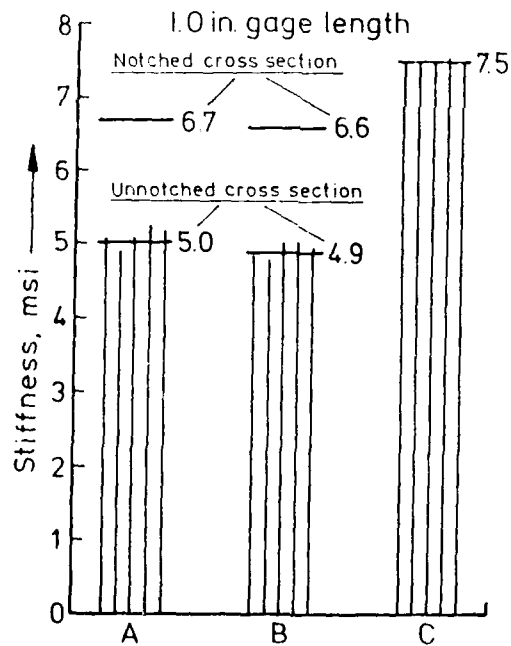


Fig. 9.4 Individual and average stiffness of notched and unnotched A-, B- and C-type laminates.

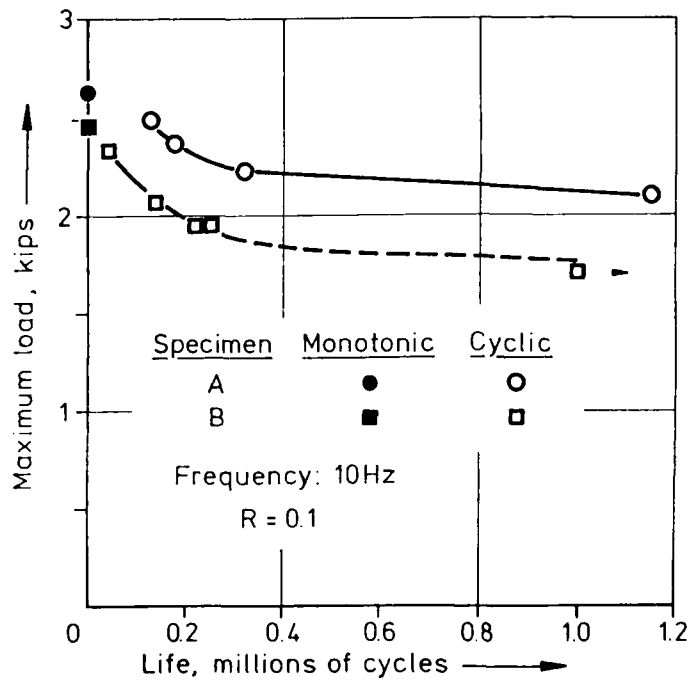


Fig. 9.5 S-N-curves for A- and B-type laminates. (R = -1).

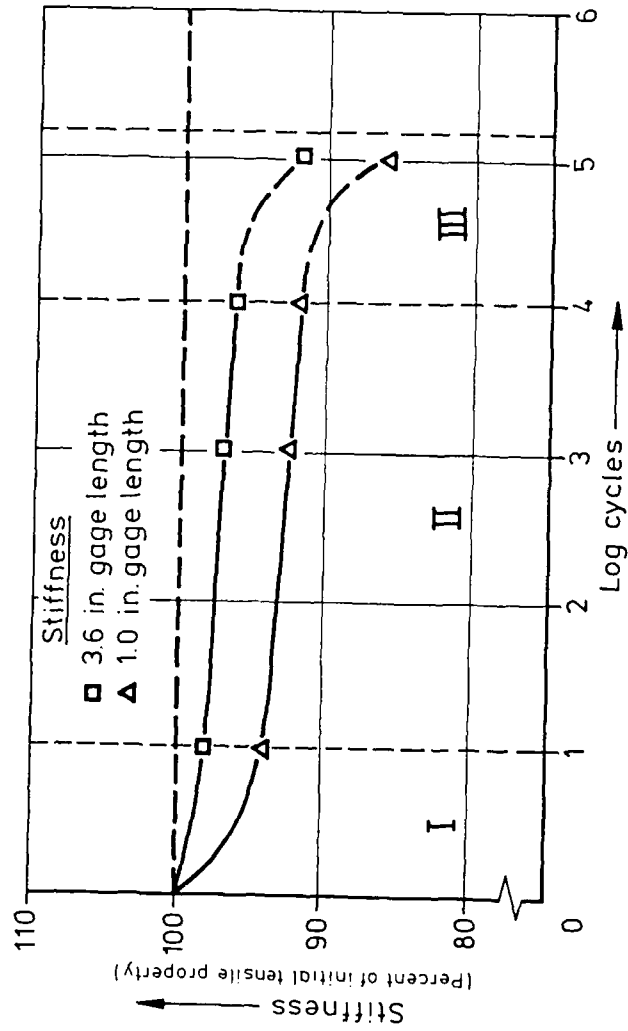


Fig. 9.6 Stiffness degradation for a B-type laminate during tension-tension fatigue loading.

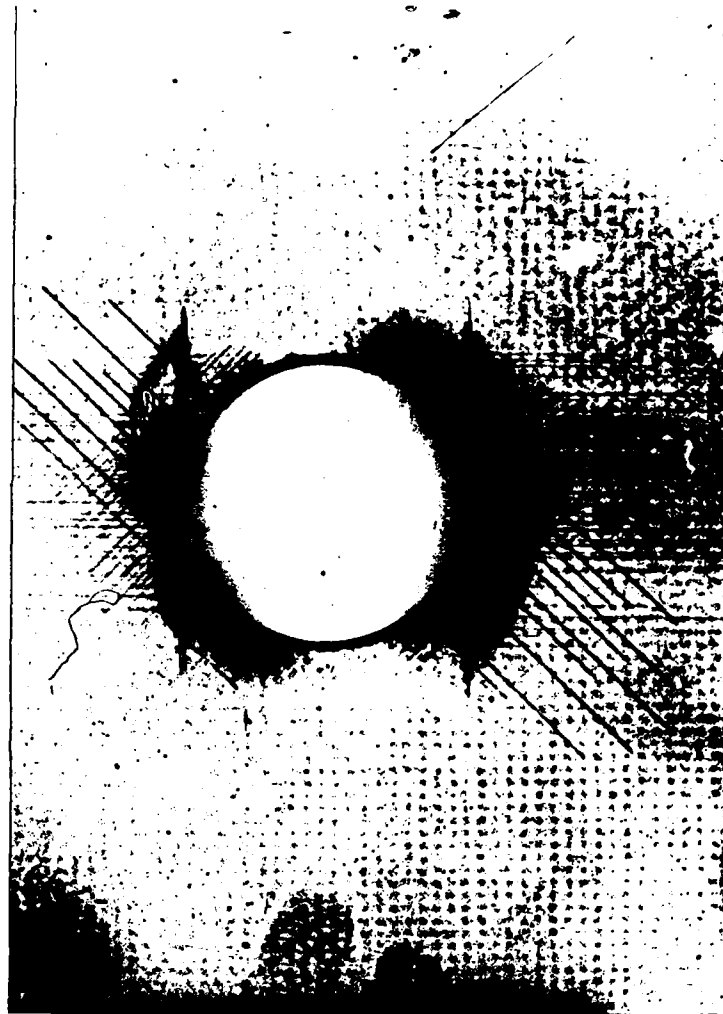


Fig. 9.7 X-ray radiograph of a damaged A-type specimen.

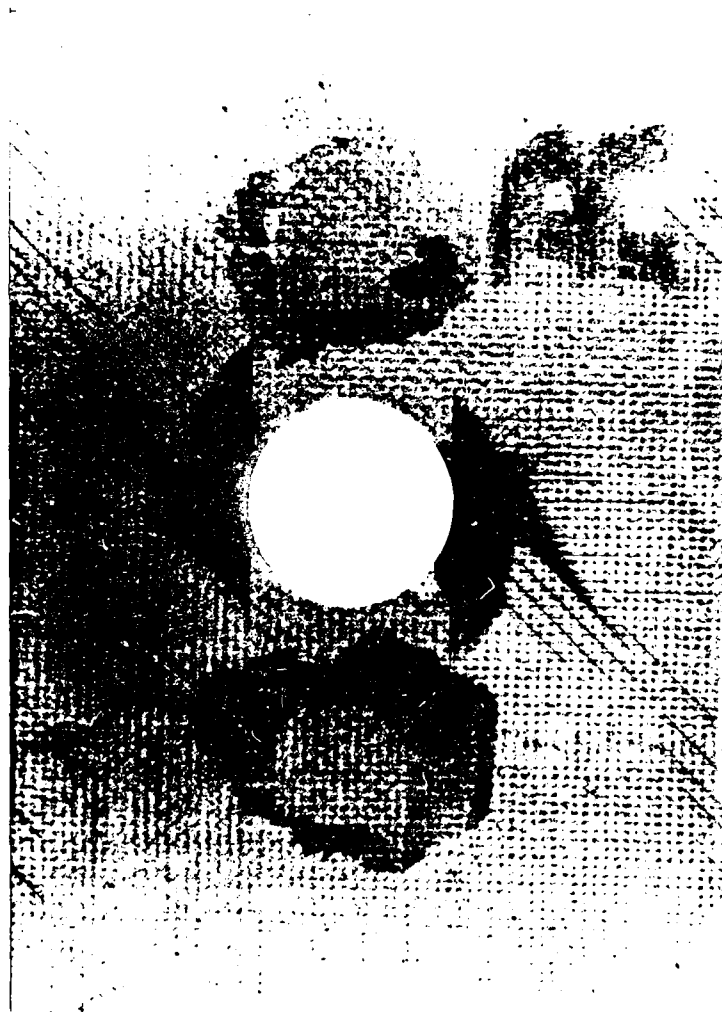


Fig. 9.8 X-ray radiograph of a damaged B-type specimen.

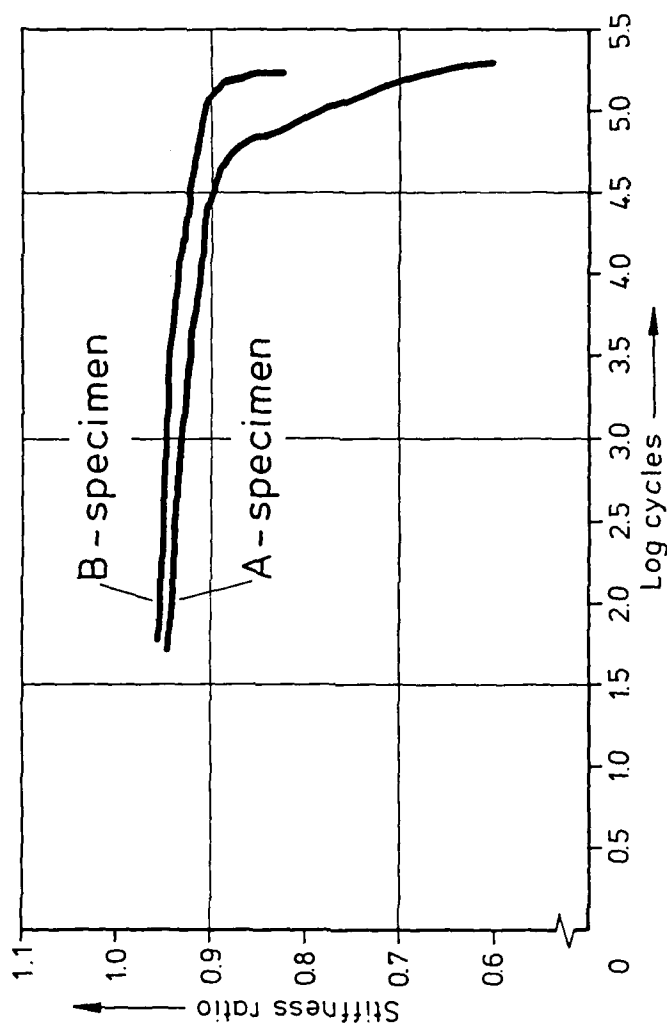


Fig. 9.9 Stiffness degradation of A- and B-type laminates during fatigue loading.

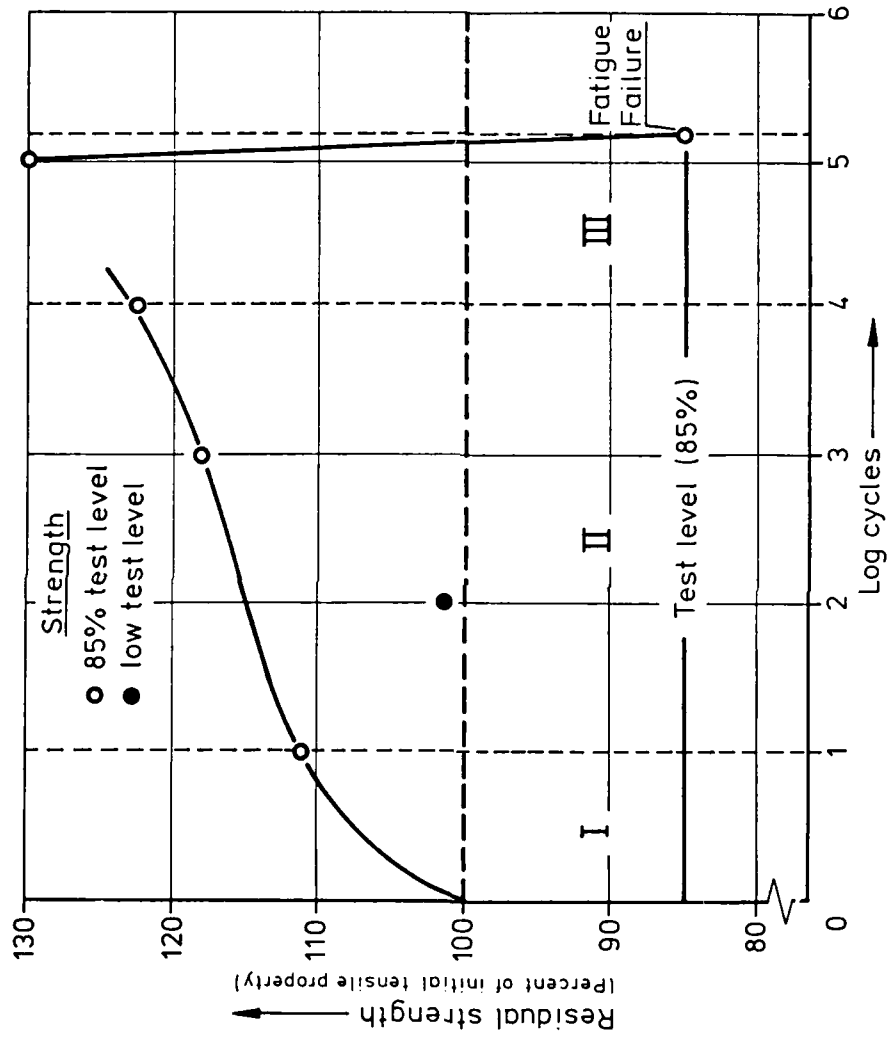


Fig. 9.10 Residual strength of B-type specimens.

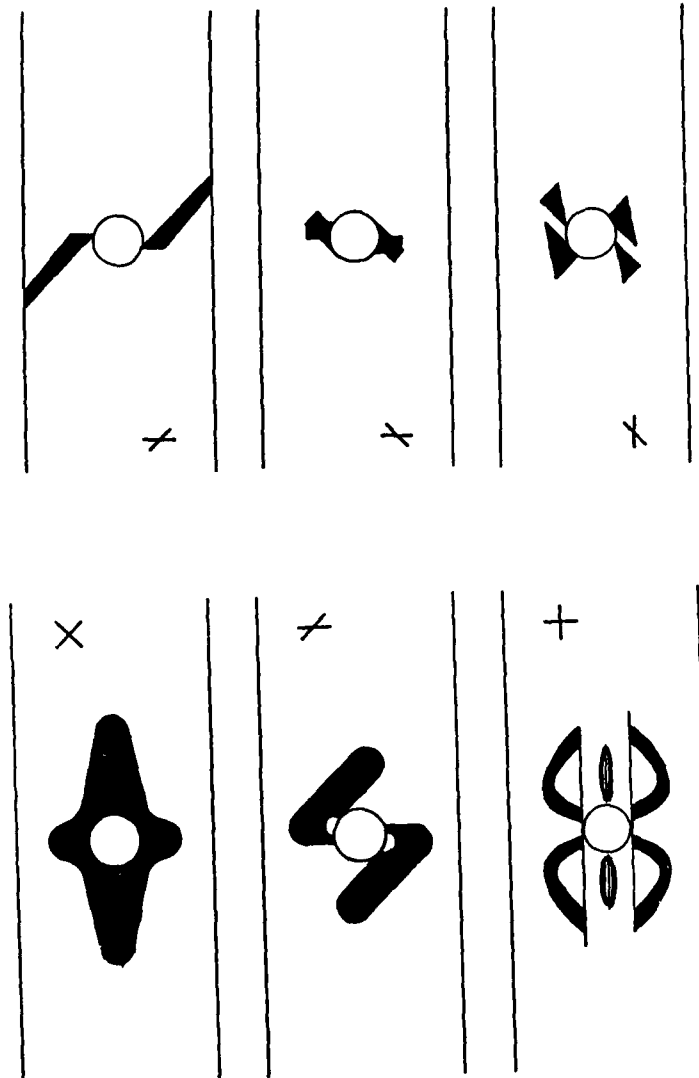


Fig. 9.11 Delamination areas in the interfaces between different layers of A- and B-type specimens.

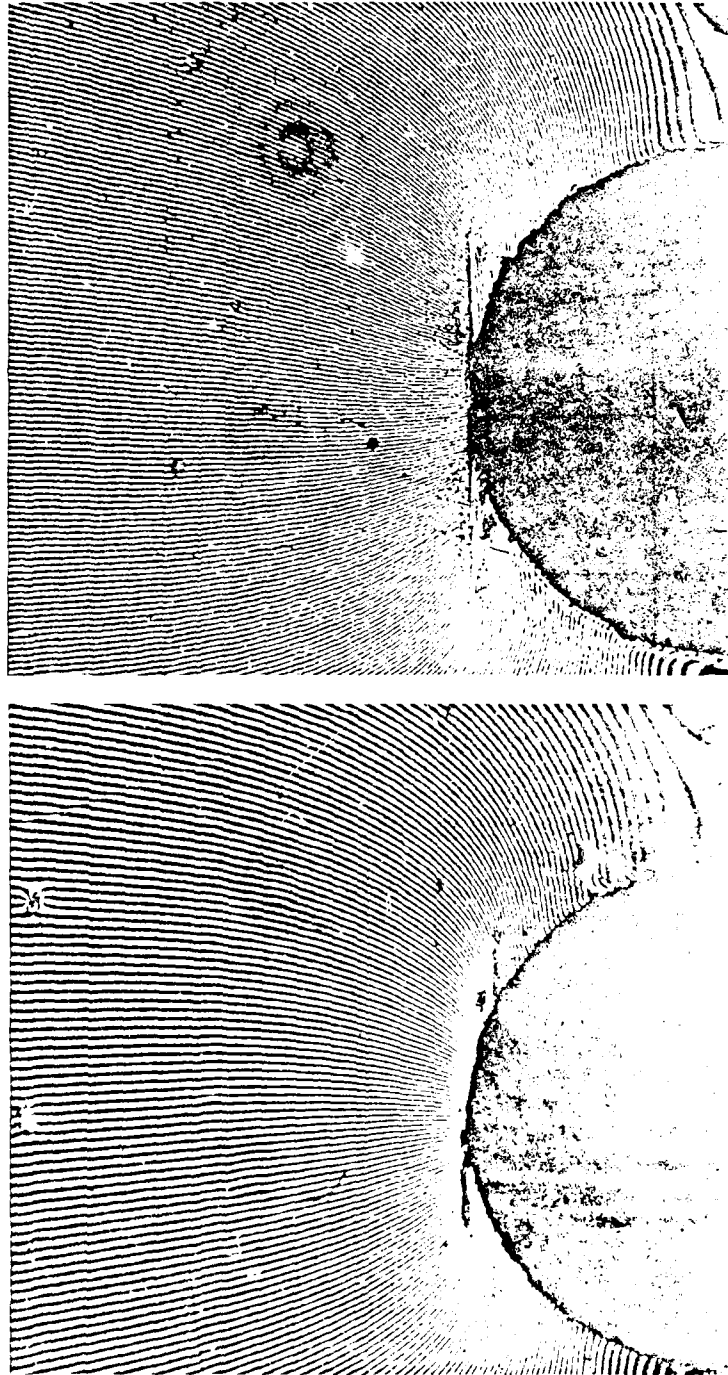


Fig. 9.12 Moiré gratings for two different crack lengths.

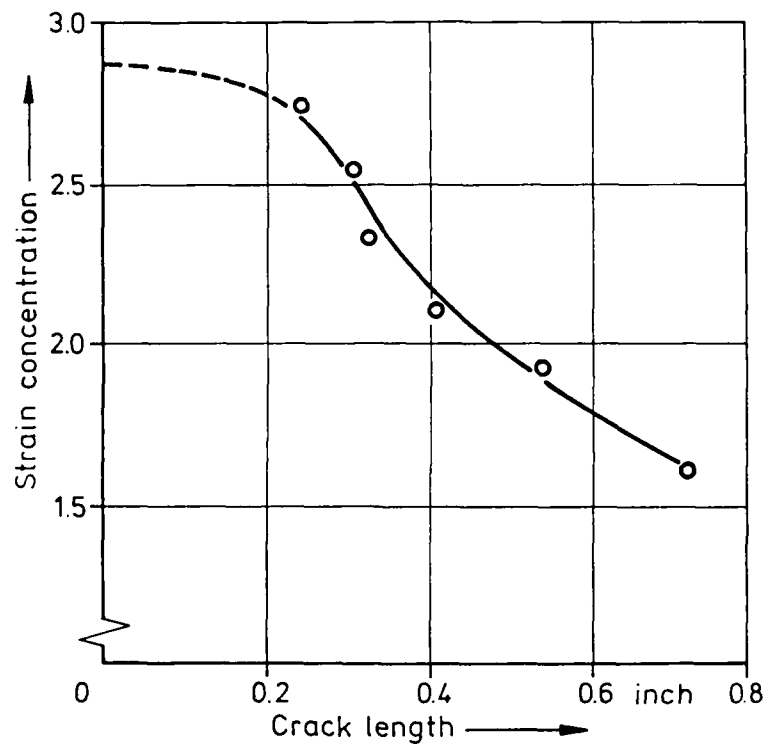


Fig. 9.13 Average strain concentration as a function of length of tangential-0-degree cracks.

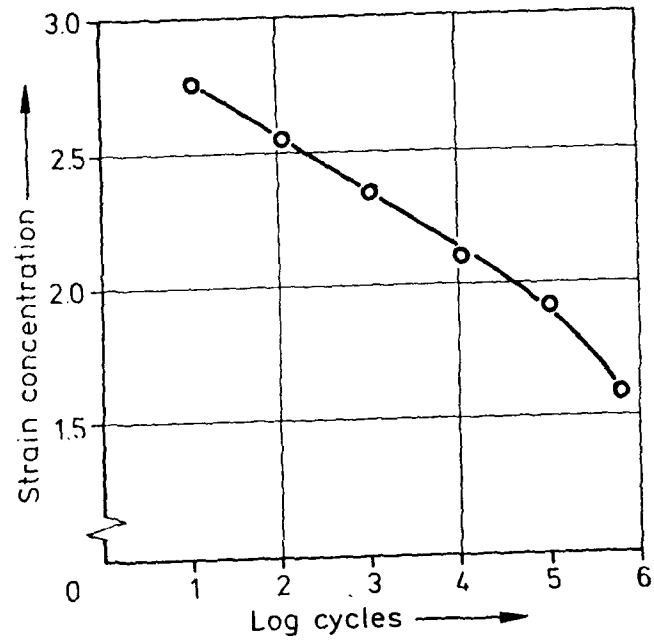


Fig. 9.14 Strain concentration versus number of cycles.

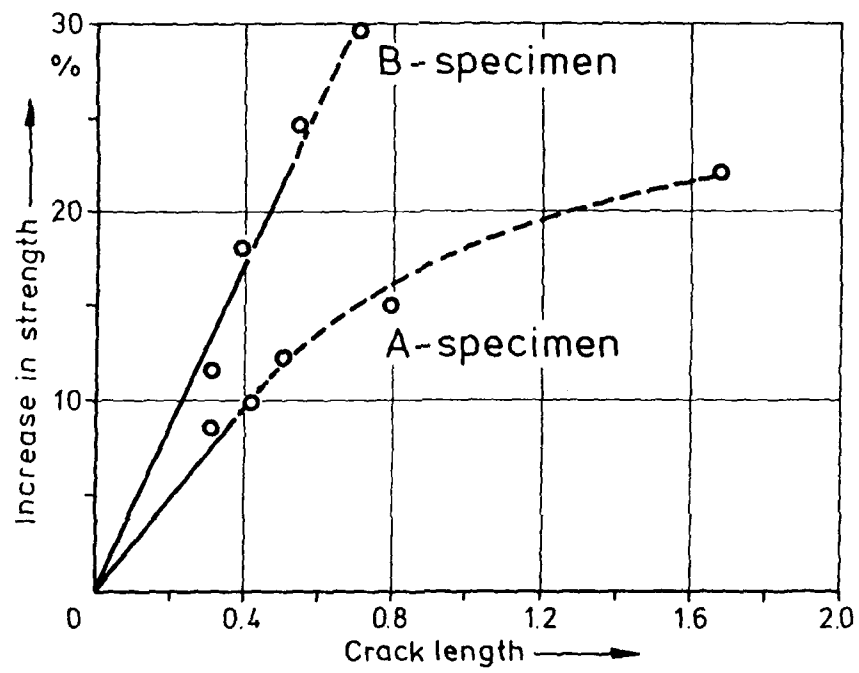


Fig. 9.15 Strength as a function of the length of tangential-0 degree cracks.

10. RESPONSE OF THERMALLY FATIGUED UN-NOTCHED SPECIMENS

10.1 Summary

Because of the different coefficients of thermal expansion of carbon fibers and polymeric resins, environmental temperature changes induce prestresses in the laminates. The magnitude of the resulting tensile stresses in the resins depends on the difference between the lock-on temperature of the resins and the lower service temperature of the composites. Repeated exposures to very low temperatures may lead to accumulating damages particularly in highly constrained laminates. In order to assess the effects of thermal cycling in a typical space environment on the mechanical properties of carbonfiber-reinforced composites, and to study the potential mechanisms of damage, a test program was performed with $[\pm 45^\circ]_{25}$ -laminates prepared from five different fiber-resin systems. Several sets of test specimens were evaluated prior to and after exposure to various numbers of thermal cycles, in vacuum, between $+100^\circ\text{C}$ and -160°C . The test results showed that strength degradations of up to 20% occurred in the epoxy-based laminates, and much more in the polyimide-based laminates, accompanied by corresponding stiffness degradations. Both types of degradation were traced to matrix cracking and to interface deterioration.

A more comprehensive treatment of the subject matter is presented in Appendix G "Influence of Simulated Space Environment on Carbonfiber-Reinforced Plastics".

10.2 Test Program

The five fiber/resin systems from which test specimens were prepared are identified in Fig. 10.1. They include high-strength as well as high-modulus fibers imbedded in four different epoxy resins with curing temperatures from 120°C to 190°C , and one polyimide resin with a curing temperature of 210°C [10.1].

The $\{\pm 45^\circ\}_{2S}$ -laminates were laid up from 0.125 mm thick prepregs and autoclave-cured with a volume fiber fraction of $60\% \pm 4\%$. The stacking order of $\pm 45^\circ$ was chosen to produce a maximum of curing prestress and, in view of the limited strength properties in the 0° -direction, to facilitate the tension and compression tests. The dimensions of the laminates used for the thermal cycling tests were 195x65 mm. Subsequent to cycling, each of the laminates was dissected into six 110x10 mm tension test specimens and six 80x10 mm compression test specimens.

The thermal cycling tests were performed in a closed test chamber at a vacuum of 10^{-4} Pa. The heating to 100°C was accomplished by infrared radiation, and the cooling to -160°C by radiation from LN_2 -filled radiators. The heating and cooling rates were applied realistically with a cycle duration of 50 min as shown in Fig. 10.2. One laminate of each material was subjected to 0, 1170, 2295 and 3480 thermal cycles. The laminates were prior to cycling completely dried and then kept dry by storage in a desiccator. Tension and compression tests before and after each cycling increment were conducted both at 23°C and at 100°C with three specimens per test point.

10.3 Strength and Stiffness Degradations

Figs. 10.3 and 10.4 display, relative to their normalized initial strengths, the residual tension and compression strengths of the test specimens cycled 1170, 2295 and 3480 times. It is apparent that the residual strengths of the epoxy-based laminates, tested at 23°C , is only moderately affected whereas the polyimide-based laminate is drastically degraded. According to Figs. 10.5 and 10.6, very similar relationships are found in the residual strength tests performed at 100°C . In general, the residual strengths were higher in resin systems with high curing temperatures. It may be assumed that a substantial amount of the strength reduction occurred already after the first few cycles. Figs. 10.7 and 10.8 contain the corresponding numerical data in terms of mean values and standard deviations.

In comparison to the modest strength decline of the test specimens, the associated reduction of their stiffness is more pronounced. Fig. 10.9 shows the magnitudes of this reduction for the four epoxy-based laminates. The data points were determined by the application of a reference stress which produced a strain of 0.2% in an uncycled test specimen when tested at 23°C.

10.4 Mechanisms of Damage

During thermal cycling the laminates were not mechanically loaded or constrained and subject only to internally induced thermal stresses. An analytical assessment indicated that in cross-ply laminates the thermal stresses transverse to the fibers exceed the tensile strength of the epoxy resin in every ply when cooled down to -160°C while the interlaminar shear strength between adjacent plies is approached but not exceeded [10.2,10.3]. Therefore, the following failure modes were expected:

- matrix cracks parallel to the fibers because of lateral constraints;
- local delaminations especially at the free edges of the laminates;
- loss of adhesion and debonding especially at the ends of the fibers.

The detection and identification of failure modes was attempted by ultrasonic and radiographic techniques, by microscopic investigations of polished surfaces and of fracture surfaces, and by analytical considerations. The suspected failure modes were indeed located although not all of them in every laminate and differing in severity from laminate to laminate.

10.4.1 Matrix Cracks

Thorough examinations of the laminates prior to cycling revealed no evidence of damage. After cycling, matrix cracks were found in different distributions and with different degrees of severity. In the epoxy-based laminates the cracks were rare and small, and

detectable only by scanning electron beam microscopy. A typical example of a matrix crack is given in Fig. 10.10. It was difficult to find a quantitative correlation between crack patterns and intensity of thermal strains because of the irregularity of crack formation. Much more distinct matrix cracks were found in the polyimide-based laminate on account of the lower ductility of the resin and the higher curing temperature. Contrast-enhanced radiographic records indicate a criss-crossing pattern of parallel lines (Fig. 10.11) which, under high magnification, could be identified as matrix cracks. The left photograph in Fig. 10.12 shows the regular spacing of the cracks and the right photograph, further magnified, the beginning of an edge delamination at the bottom of a crack between the first and second ply of a polyimide-laminate.

10.4.2 Local Delaminations

Refined ultrasonic techniques allow the detection of delaminations with diameters ≥ 0.5 mm. All such records for the epoxy-based laminates were uniform and free of defects as exemplified in Fig. 10.13 for the T300/914C material. Corresponding C-scans for the polyimide-based laminate have a drastically different appearance already after 1170 thermal cycles. It is evident from Fig. 10.14 that delaminations occurred both centrally and at the free edges of the laminate, which is consistent with the observations made in the preceding section.

10.4.3 Degradation of Fiber-Matrix Interface

Positive proof of loss of adhesion between fibers and matrix could not be established with the cited inspection techniques; however, an indication of degradation is apparent from a comparison of the texture of fiber surfaces in the microphotographs of Fig. 10.15. Before thermal cycling the fibers are covered with many specks of matrix material while after cycling the surfaces are relatively smooth, indicating a changed quality of adhesion.

Further evidence of degradation is given in Figs. 10.16 and 10.17 in the form of stress-strain diagrams established after various numbers of thermal cycles for the T300/914C-laminate. The continuous decline of stiffness with increasing cycle numbers is obvious, particularly at high test temperatures, although it is uncertain whether this effect is attributable to the matrix cracks, a deteriorating interface, or a combination of both.

10.5 Additional Observations

It should be expected that the presence of matrix cracks or fiber debonds will influence the coefficients of thermal expansion of the laminates. According to Fig. 10.18 a trend towards higher coefficients with increasing numbers of thermal cycles could be observed in the investigated temperature regime between 30°C and 100°C.

Also, the accumulation of damage ought to affect the natural frequencies and the damping characteristics of the laminates which is reflected in Fig. 10.19.

It may be concluded from the test program that in the tested temperature range from 100°C to -160°C the development of matrix cracks in cross-ply laminates cannot be avoided. The associated changes of the physical properties are relatively minor in epoxy-based laminates with high curing temperatures, whereas extreme caution should be exercised in the application of polyimide-based laminates.

10.6 References

- [10.1] Camahort, J.L.
Rennhack, E.H.
Coons, W.C.

Effects of Thermal Cycling
Environment on Graphite/Epoxy
Composites, Environmental Effects
on Advanced.
Composite Materials, 1976,
ASTM STP 602
- [10.2] Mazzio, V.F.
Mehan, R.L.

Effects of Thermal Cycling on the
Properties of Graphite/Epoxy Composites.
Composite Materials: Testing and
Design,
ASTM STP 617.
- [10.3] Woolstencroft, D.H.
Curtis, A.R.

Interface Stresses in Unidirec-
tional Carbon Fibre Composites.
PLASTICS AND RUBBER INST.,
Interfaces in Composite Materials,
Univ. of Liverpool, England,
Apr. 1,2 1981, 29 p.

Material Designation	Type of Fiber Type of Resin	Curing Temperature	Symbol
HY-E 1548 A 1 B	Celion GY - 70 Fiberite 948 A 1	120° C	x
LY 556 / HY 917 / XB 2692 / T 300	Toray T 300-6000 Unmodified Epoxy	140° C	□
HY-E 2034 D	Thorne1 Pitch Fiberite 934	180° C	Δ
914C-TS-5	Toray T 300 Ciba 914	190° C	○
T3T F 178	UC T 300-3000 Hexcel F 178	210° C	▽

Fig. 10.1 List of materials.

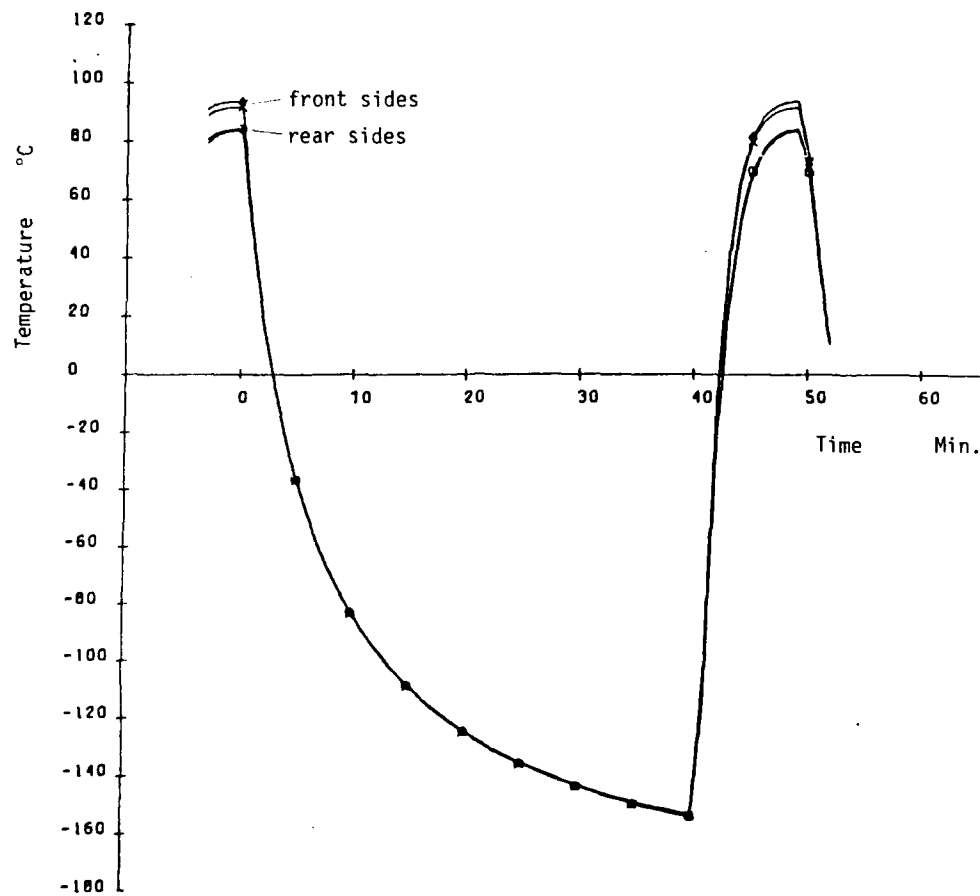


Fig. 10.2 Typical thermal cycle of surface temperatures versus time of two specimens.

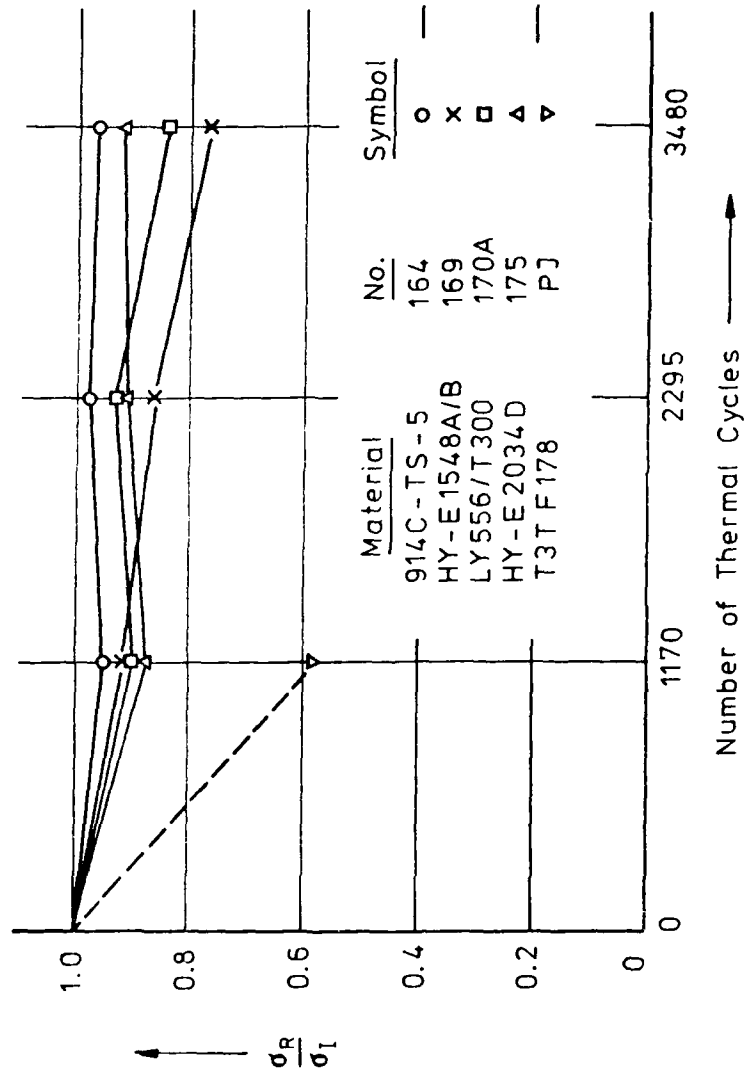


Fig. 10.3 Residual tensile strength at 23°C test temperature.

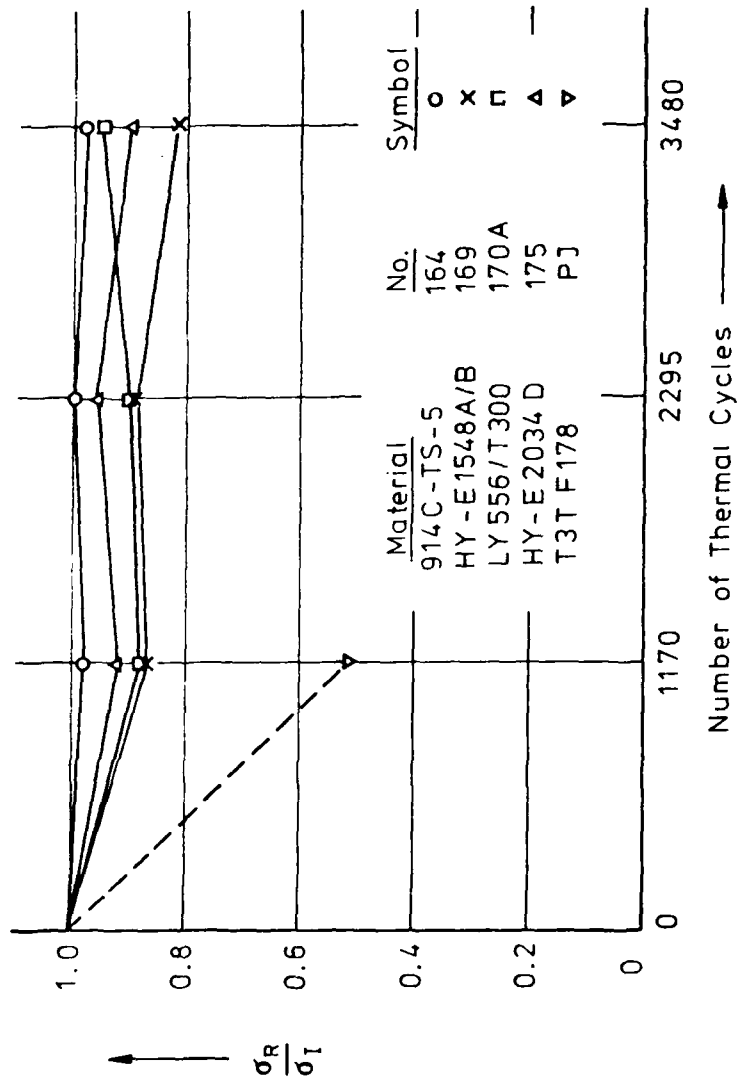


Fig. 10.4 Residual compressive strength at 23°C test temperature.

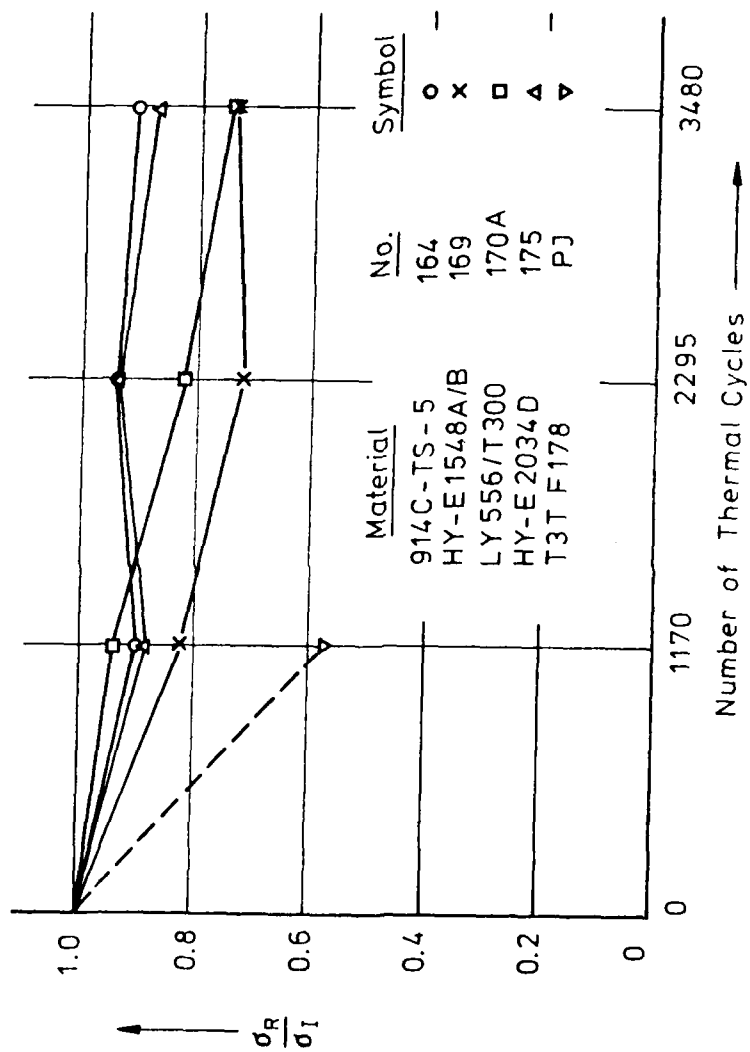


Fig. 10.5 Residual tensile strength at 100°C test temperature.

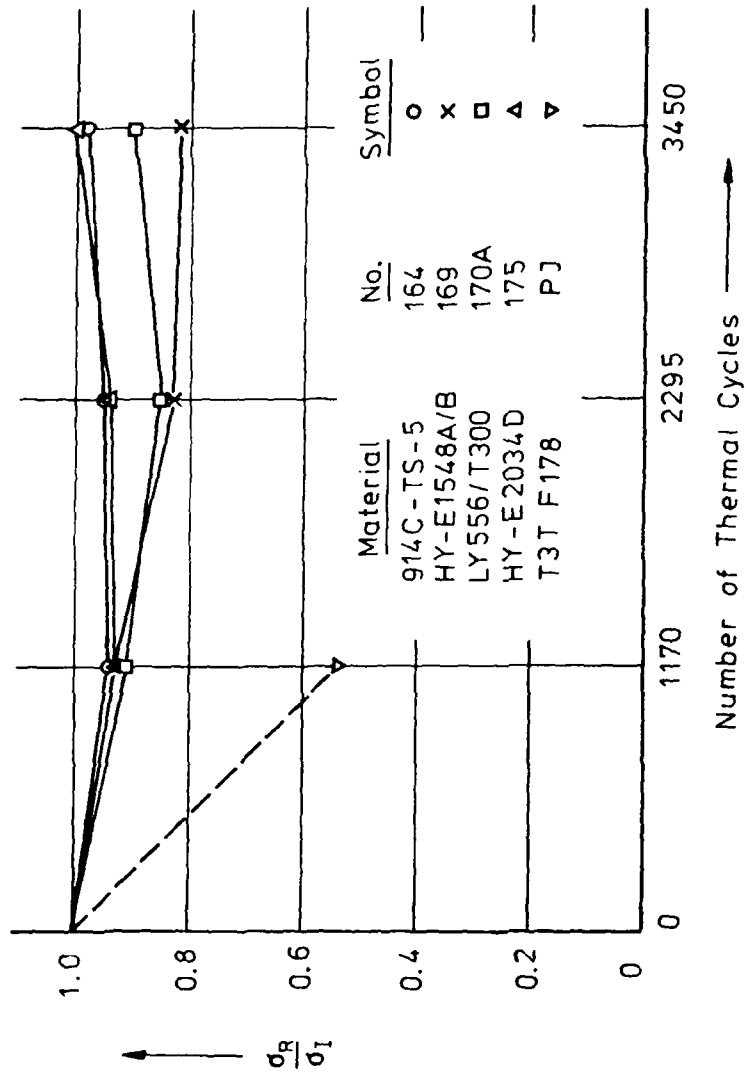


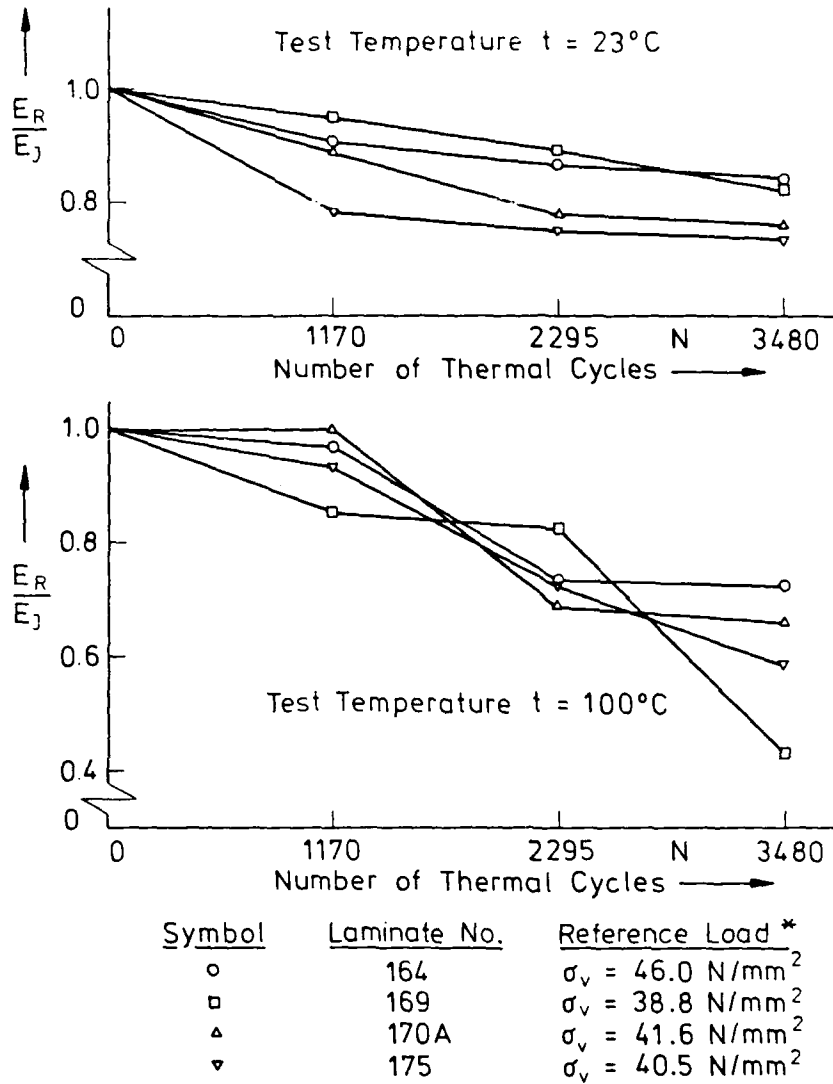
Fig. 10.6 Residual compressive strength at 100°C test temperature.

Laminate No. Material	Tensile Strength N/mm ²						Compressive Strength N/mm ²					
	Test Temperatur 23°C						Test Temperatur 23°C					
	0 Cycles	1170 Cycles	2295 Cycles	3480 Cycles	0 Cycles	1170 Cycles	0 Cycles	1170 Cycles	2295 Cycles	3480 Cycles	0 Cycles	1170 Cycles
164 914C-TS-5	156,6 6,6	148,8 4,7	153,5 3,7	151,9 2,5	163,0 9,6	159,1 1,5	163,0 9,6	159,1 1,5	163,5 6,9	159,7 4,6	163,0 9,6	159,1 1,5
169 HY-E 1548 A1B	122,9 8,1	112,7 2,2	106,1 0,4	94,4 3,3	122,2 7,5	106,2 3,5	122,2 7,5	106,2 3,5	108,4 4,0	100,5 0,9	122,2 7,5	106,2 3,5
170 A LY556/917/XB2692	204,2 11,8	183,1 6,5	190,3 8,7	172,8 16,6	188,9 11,8	167,1 4,7	188,9 11,8	167,1 4,7	169,2 11,4	178,7 1,8	188,9 11,8	167,1 4,7
175 HY-E 2034 D	69,9 3,9	61,3 1,9	63,9 0,7	64,3 0,8	68,5 6,8	58,3 0,9	68,5 6,8	58,3 0,9	66,1 2,0	61,6 9,3	68,5 6,8	58,3 0,9
PI T3T F 178	145,7 1,3	84,3 0,4			165,6 3,1	85,0 5,7	165,6 3,1	85,0 5,7			165,6 3,1	85,0 5,7

Fig. 10.7 Mean strength and standard deviation at 23°C.

Laminate No. Material	Tensile Strength N/mm^2						Compressive Strength N/mm^2					
	Test Temperature 100°C						Test Temperature 100°C					
	0 Cycles	1170 Cycles	2295 Cycles	3480 Cycles	0 Cycles	1170 Cycles	0 Cycles	1170 Cycles	2295 Cycles	3480 Cycles	0 Cycles	1170 Cycles
164 914C-TS-5	143,1 4,9	128,6 1,3	134,6 2,0	130,6 1,5	143,5 3,7	134,4 7,6	143,5 3,7	134,4 7,6	135,7 4,9	140,7 5,5	143,5 3,7	134,4 7,6
169 HY-E 1548 AlB	115,5 2,0	94,6 1,7	83,1 1,0	84,3 2,2	97,9 2,0	91,5 2,0	97,9 2,0	91,5 2,0	80,9 1,3	80,7 1,3	97,9 2,0	91,5 2,0
170 A LY556/917/AB2692 T300	119,5 5,2	112,5 12,0	97,8 3,5	87,8 7,9	115,3 5,7	105,4 6,1	115,3 5,7	105,4 6,1	97,8 0,7	111,1 2,3	115,3 5,7	105,4 6,1
175 HY-E 2034 L	58,5 1,9	51,9 4,1	54,5 2,6	51,2 1,1	57,0 4,6	53,2 2,0	57,0 4,6	53,2 2,0	53,3 3,5	57,1 7,3	57,0 4,6	53,2 2,0
PI T3T F 178	121,5 0,3	69,0 4,2			139,1 3,9	73,9 3,8	139,1 3,9	73,9 3,8			139,1 3,9	73,9 3,8

Fig. 10.8 Mean strength and standard deviation at 100°C.



* Reference Load was Defined to be the Load Resulting in an Elongation of 2mm/m of a Virginal Specimen at Room Temperature

Fig. 10.9 Stiffness degradation due to thermal cycling.

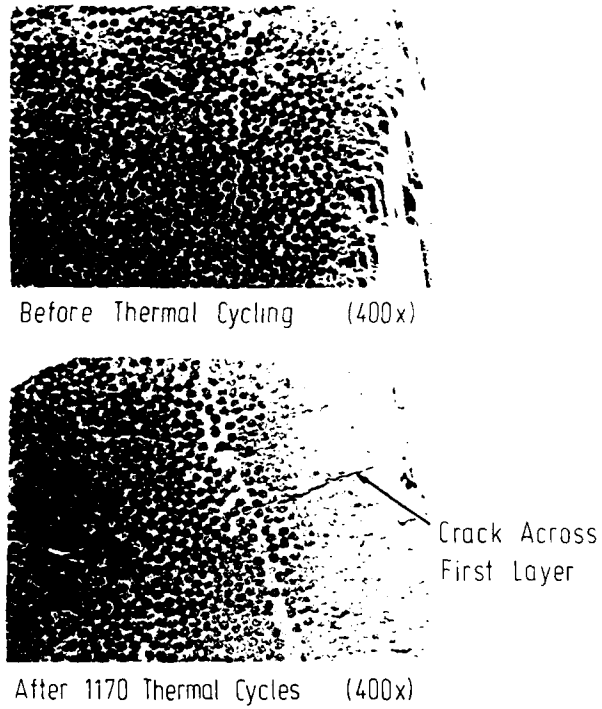


Fig. 10.10 Photomicrographs of the cross section of a 914C-TS-5 sample before and after thermal cycling .

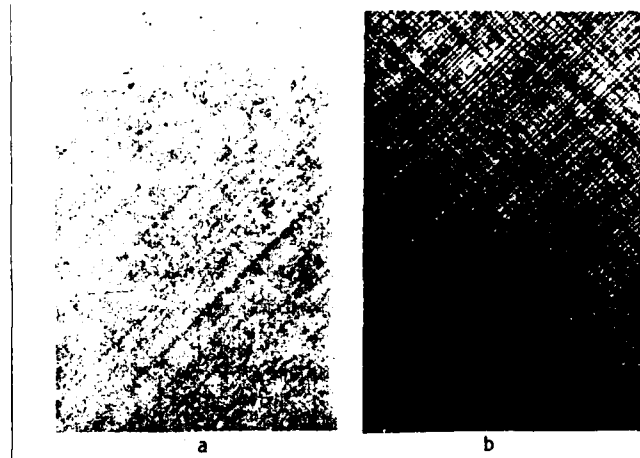


Fig. 10.11 X-Ray photographs of a T3T F178 laminate
 a) before thermal cycling
 b) after 2295 thermal cycles

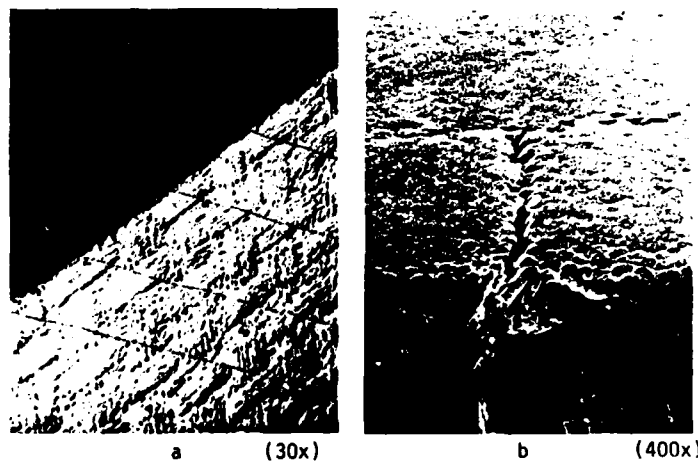


Fig. 10.12 Sample of T3T F178 after 1170 thermal cycles
 a) thin dark lines are surface cracks
 b) surface crack and subsequent delamination.

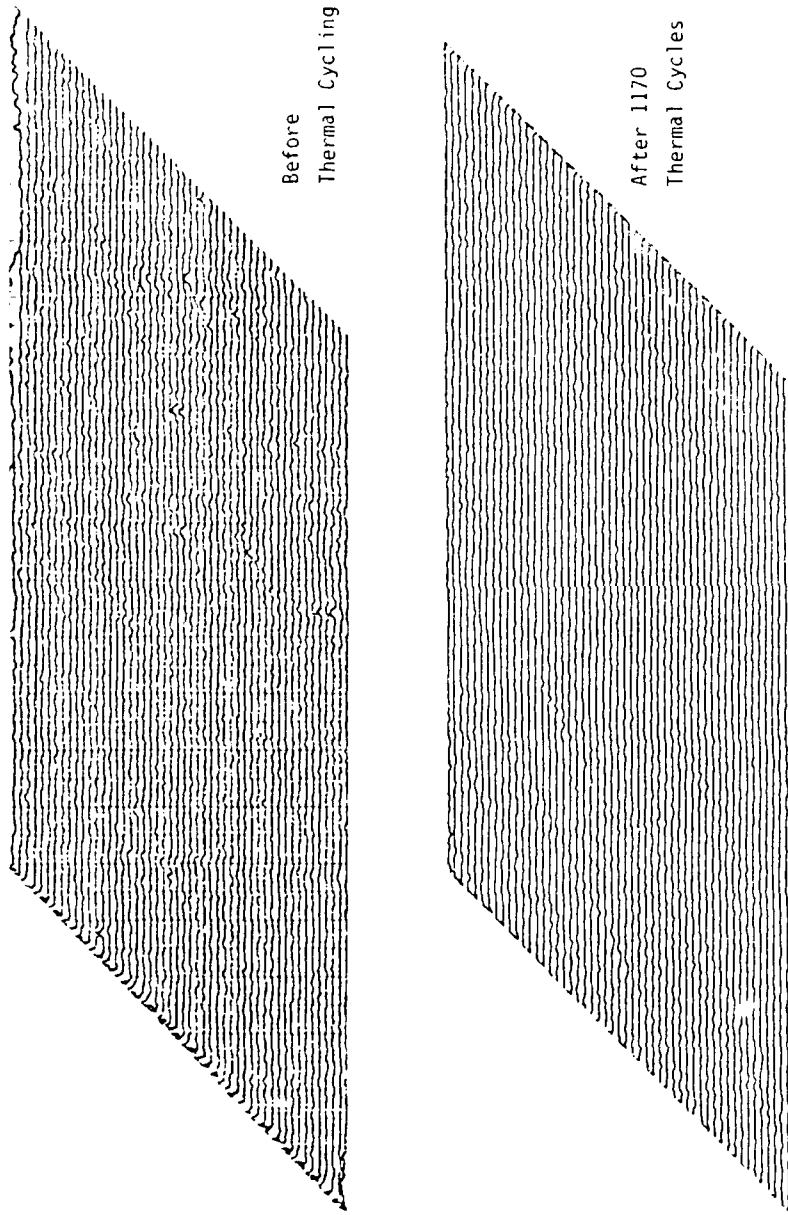


Fig. 10.13 Amplitude scans of a 914C/T300 laminate before and after thermal cycling.

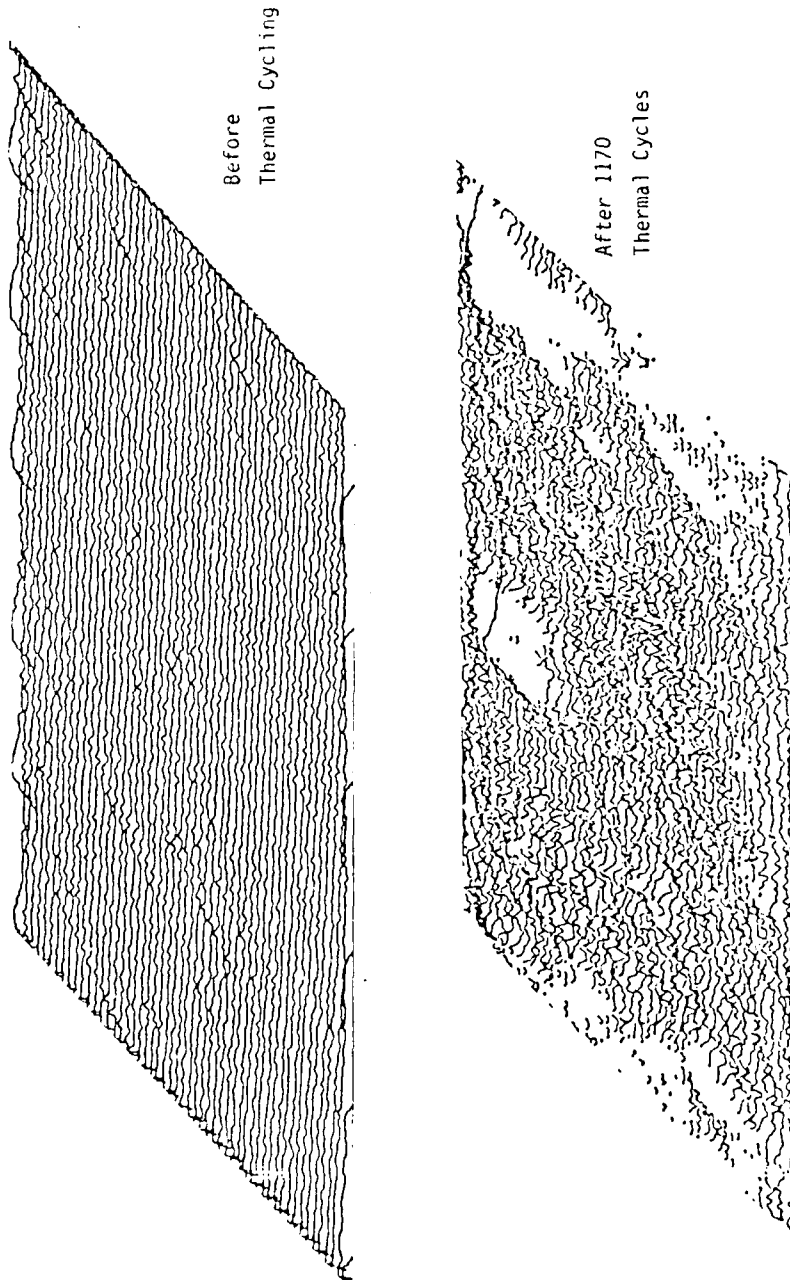


Fig. 10.14 Amplitude scans of a T3I F178 laminate before and after thermal cycling .

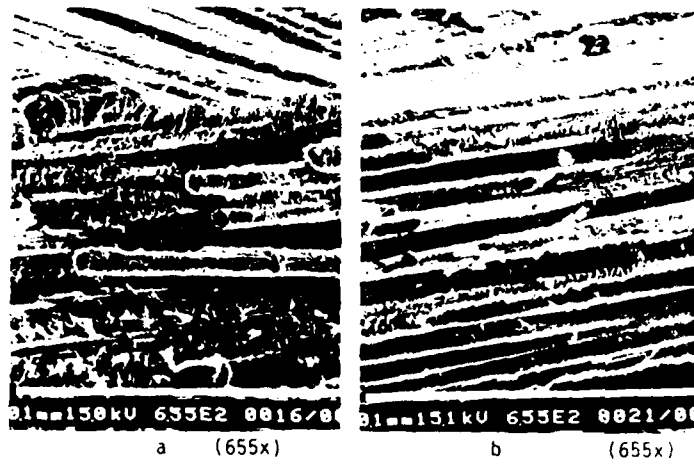


Fig. 10.15 Fracture surfaces of 914C-TS-5 specimens
a) before and b) after thermal cycling.

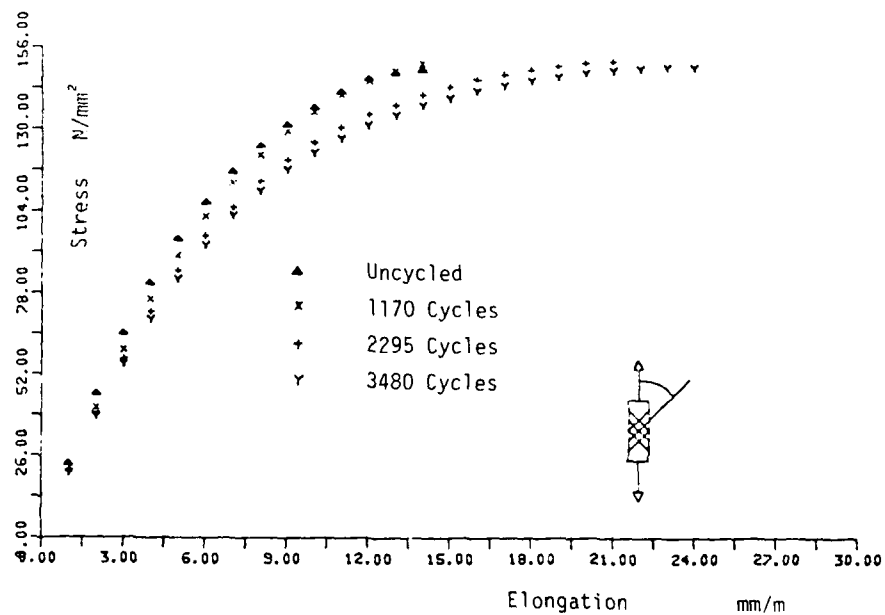


Fig. 10.16 Stress-strain curves for 914C/T300 laminate at 23°C
(Average values of 3 tests).

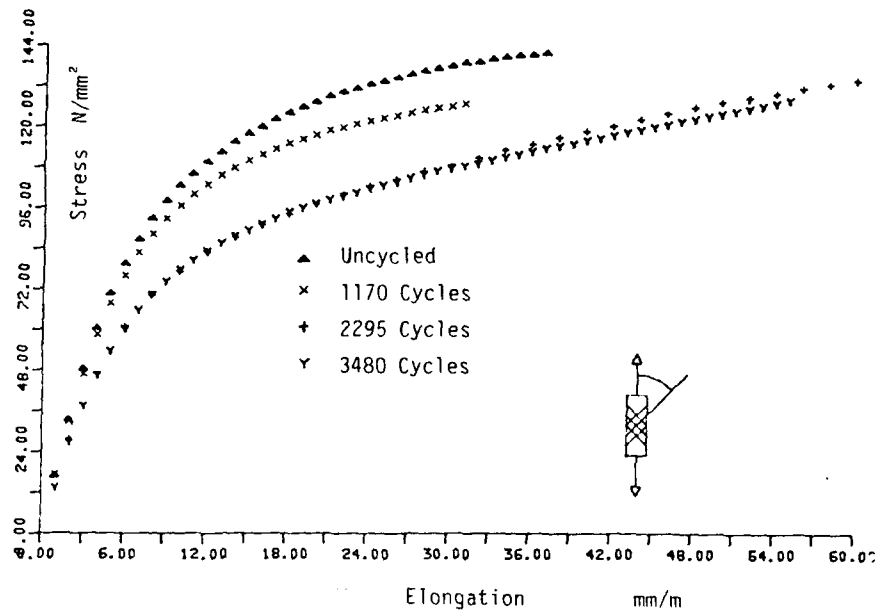


Fig. 10.17 Stress-strain curves for 914C/T300 laminate at 100°C (Average values of 3 tests).

Number of Cycles	Laminate Type (Ref. Fig.1)			
	○	×	□	▽
0	1.9	0.6	1.5	-0.9
1170	—	—	1.7	—
2295	1.9	0.6	2.0	-0.9
3480	2.0	0.6	2.4	-0.8
$\times 10^{-6} m/m \text{ } ^\circ C$				

Fig. 10.18 Coefficients of thermal expansion.

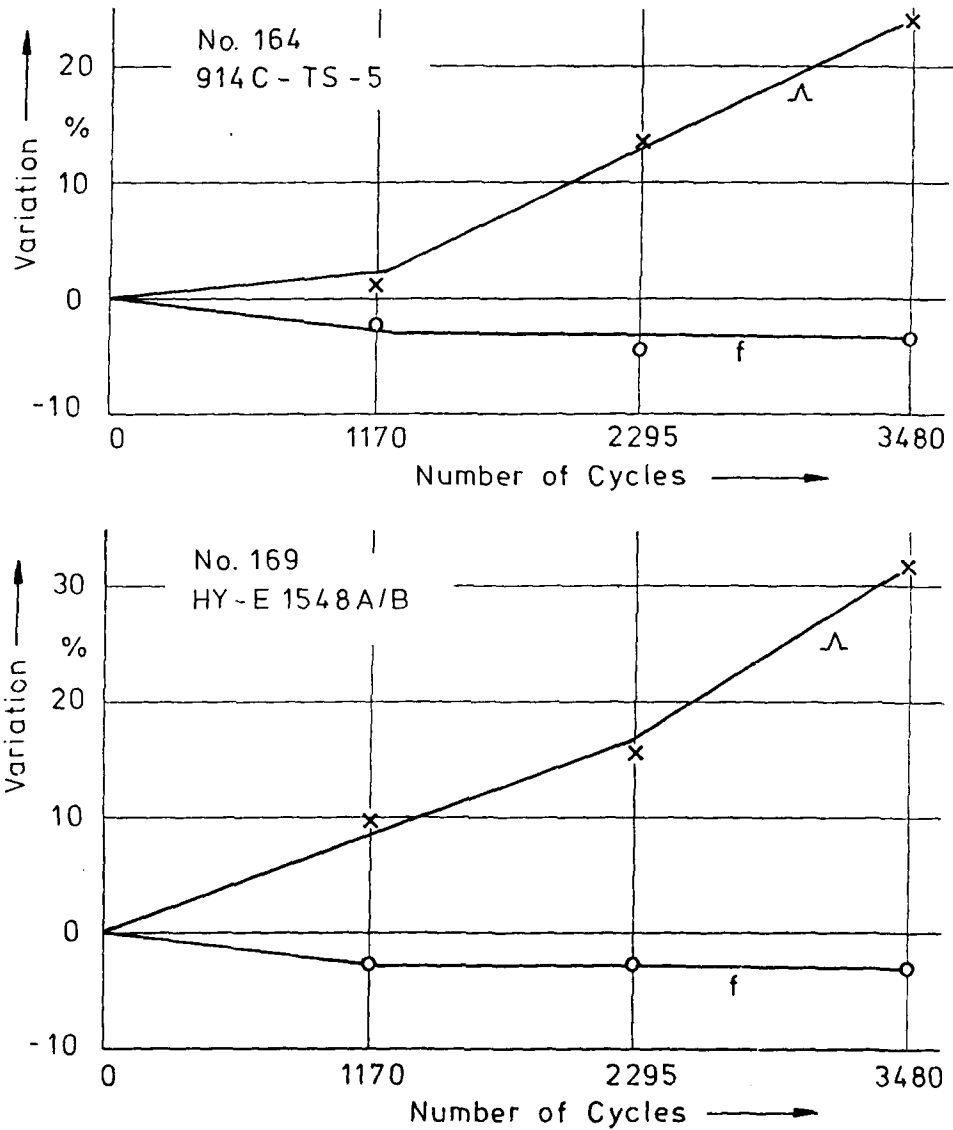


Fig. 10.19 Change of natural frequencies and damping characteristics in percentages of the original values as a result of thermal cycling.

11. STRAIN CAPABILITIES AND STRAIN RATE EFFECTS IN EPOXY RESINS AND LAMINATES

11.1 Summary

The currently available epoxy resins with curing temperatures of ca. 180°C have relatively low strain capabilities. The desirable increase of the strain values at failure under retention of reasonably high service temperatures is chemically incompatible and beyond the state of the art. It is uncertain therefore, whether the availability of advanced high strength-high strain carbonfibers in connection with the present generation of epoxy systems can offer significant advantages. Alternatively, the question can be raised what ranges of strain capability will be required in order to exploit the potential of the new carbonfibers. As a supplement to similar studies of other authors [11.1], [11.2], [11.3], investigations in this direction were made with a variety of matrix formulations and fiber types under ambient conditions, i.e., initially by-passing the issue of maximum service temperature. The majority of the tension tests were performed with unidirectional ring-type specimens [11.4] which led to quantitative and consistent results. By increasing the matrix failure strain from $\epsilon = 1.5\%$ to $\epsilon = 2.5\%$, strength improvements between 14 % and 54 % are possible. A second issue was the sensitivity of the strength and stiffness properties of the test specimens to different strain rates. With two specially constructed loading devices, loading rates differing by four orders of magnitude could be applied. The tests showed, somewhat surprisingly, that for strain rates greater than $d\epsilon/dt = 1.0\%$ per sec the strength values of the test specimens remain constant regardless of the ductility of the matrix. The majority of the tests were accompanied by acoustic emission analyses. Under the assumption that the acoustic energy release is an indicator for the fracture phenomenon as such, ideal or less ideal fracture sequences can be identified by comparison of the integrated energy release at prescribed deformation states.

11.2 Material Choice and Test Specimen Configurations

With respect to the matrix material two epoxy resins were selected which, dependent on their mixture and hardened with HT 976, produce different strain capabilities in the aggregate. One of the resins carries the designation MY 720 and has high thermal stability while the other, known as LY 556, is extremely ductile, as shown in Fig. 11.1. A total of nine different mixtures were prepared and tested, ranging from 0 % LY 556 and 100 % MY 720 to 0 % MY 720 and 100 % LY 556.

The resin mixtures were reinforced with three different kinds of carbonfibers, namely, HM45 (high stiffness), T300 (high strength) and ST3 (high strain). Their mechanical properties are listed in Fig. 11.2.

For the evaluation of the neat epoxy resins, 15×3×200 mm and 15×3×200 mm flat specimens and 3.8 mm thick rings with an inside diameter of 146 mm and a width of 6.4 mm were prepared. The carbonfiber-epoxy composites were tested in the form of so-called NOL-rings [11.5]. The filament-wound rings consisted of unidirectionally aligned rovings and had an inside diameter of 146 mm, a thickness of 1.6 - 1.8 mm and a width of 6.4 mm. The fiber volume fraction was approximately 60 %.

11.3 Test Procedure for Epoxy Resins

The thermal stability tests were conducted with 15×3×60 mm flat specimens according to DIN 53 458 (Martens method). The specimens were tested in a dry condition and after moisture-saturation at 100 % relative humidity.

The testing of the tensile stress and strain properties was accomplished with 15×3×200 mm flat specimens in a spindle-driven Zwick 1484 test machine with a feed of 2 mm/min. The test specimen displacements were measured inductively over a length of 50 mm. The test data were recorded and issued in the form of stress-strain diagrams by a process computer attached to the test machine. In order to assess the influence of the test specimen

configuration, additional tests were performed with the ring-type specimens described above. The hydraulic loading procedure and the data acquisition corresponded to those of the NOL-ring tests (Section 11.5.1).

11.4 Test Results for Epoxy Resins

Fig. 11.3 summarizes the results of the thermal stability tests conducted for the various resin mixtures. In the wet condition the thermal stability is surprisingly insensitive to proportions of the mixtures while in the dry condition the dependence is almost linear, as expected.

The results of the strength and ductility tests are given in Figs. 11.4 and 11.5 depicting the failure stresses and failure strains, respectively, for the nine resin mixtures. Each data point represents the mean value of at least five replicates of the flat specimens and of at least three of the ring-type specimens. Even though the scatter of the data is large and the distribution somewhat erratic, a clear tendency towards higher strength and higher ductility exists for increasing amounts of LY 556 up to 80 %. The subsequent drop at 100 % LY 556 defies rational explanation.

11.5 Test Procedure for NOL-Rings

The goal of the test program was the assessment of the effects of different loading rates on the mechanical properties of unidirectional laminates. For that purpose two test facilities were designed capable of low and high loading rates. In both cases the NOL-rings were loaded by radially directed hydraulic pressure producing uniform tension. The major advantage of this test procedure was the avoidance of the normally encountered gripping problem. Considering the ring dimensions both the curvature of the ring and the normal pressure component were assumed negligible.

11.5.1 Test Facility for Low Loading Rates

The major components of the test facility are depicted in Fig. 11.6. The NOL-ring is loosely fitted i. to a circular pressure chamber capable of 450 bar and sealed oif with a concentric rubber seal at its inside face [11.5]. The hydraulic pressure is produced by the downward motion of a plunger. The dimensions of the test facility are such that the velocity of the plunger corresponds to 1.26 times the velocity of the circumferential length increase of the NOL-ring. The entire assembly is placed into a Zwick 1300 test machine and the plunger compression-loaded at velocities dictated by the limitations of the test machine. The actually executed plunger velocities were 20 mm/min and 360 mm/min, implying circumferential length increases of 15.9 mm/min ($d\epsilon/dt = 0.057\%$ per second) and 286 mm/min ($d\epsilon/dt = 1.04\%$ per second), respectively.

During a typical test the hydraulic pressure and the radial extension of the NOL-ring were measured by a pressure gauge and displacement transducers, and recorded directly on a x-y-t-recorder, as shown in Fig. 11.7. Additionally, the acoustic energy release was monitored to assist in the identification of failure modes.

11.5.2 Test Facility for High Loading Rates

In order to substantially exceed the loading rates achievable in semi-static test machines, a new test facility was developed allowing circumferential length changes of the NOL-rings of 660000 mm/min ($d\epsilon/dt = 1600\%$ per second). The major feature of the new facility is a different propulsion device for the plunger. Both the original positioning and sealing provisions were retained. As shown in Fig. 11.8, the upper part contains a double-faced sealed plunger whose downward motion can be arrested in the cylinder by a shear pin. Above the cylinder a hydraulic storage unit contains an elastic bladder filled with gaseous nitrogen. Gradual pressurization compresses the bladder to maximally 330 bar and ultimately shears the pin holding the plunger. Under the subsequent expansion of the bladder the plunger moves

downward and loads the NOL-ring in an explosive fashion. Fig. 11.9 is a photograph of the high loading rates facility ready for operation.

The hydraulic pressure exerted on the NOL-ring and its radial displacement were monitored according to Fig. 11.10. In view of the short test duration of ca. 1 msec the test data had to be initially stored in a transient recorder. The simultaneous storage of pressure and strain data allowed the evaluation of the pressure as a function of strain and the strain as a function of time.

11.6 Test Results on Mechanical Properties for NOL-Rings

In the course of the test program the influence of the following parameters on the stress-strain relationships of NOL-rings was investigated:

- a) different carbonfibers (ST3, T300, HM45)
- b) different matrix strain capabilities
($\epsilon_{ult} = 1.45\%$ to $\epsilon_{ult} = 2.8\%$)
- c) different strain rates
($d\epsilon/dt = 0.057\%$ per sec. to $d\epsilon/dt = 1600\%$ per sec.)

The results of the low strain rates tests are displayed in Figs. 11.11 through 11.14 in terms of failure stresses and failure strains of the NOL-rings versus the elongations of the nine different matrix systems. It is apparent that under more or less semi-static loading ($d\epsilon/dt = 0.057\%$ per sec.) the failure stresses of the NOL-rings with all fiber-types improves significantly with increasing matrix elongations (Fig. 11.11). The same trend prevails, although somewhat less pronounced, with respect to the failure strains (Fig. 11.12).

In contrast, no or only insignificant improvements of failure stresses or failure strains are evident at a strain rate of $d\epsilon/dt = 1.04\%$ per second even at very high matrix elongations (Figs. 11.13 and 11.14). From the fact that at a matrix elongation

of 1.45 % both strain rates produce comparable values for failure stresses and failure strains it may be surmised that at high strain rates the more ductile matrices have insufficient time to develop their potential. Figs. 11.15 through 11.17 show a comparison of the elastic moduli of the different fiber-type composites in dependence on the matrix elongation. For all fiber-matrix systems the values of the moduli obtained at a strain rate of $d\epsilon/dt = 1.04$ % per second lag those obtained at the very low strain rate of $d\epsilon/dt = 0.057$ % per second for perhaps the same reason as advanced above.

First results of the high strain rate tests ($d\epsilon/dt = 1600$ % per sec) concerning the failure stresses are displayed in the Figs. 11.18 through 11.21. The tests indicated no dependence of the strength on matrix elongation, as already noticed at a strain rate of 1.04 % per second. This again points to the fact that the potential of a more ductile matrix cannot be utilized at very high strain rates.

In comparison to the test results obtained at a strain rate of 1.04 % per second, the increase of the failure stress in HM45 composites amounted to 37 %, Fig. 11.19, and to an average of 10 % in ST3 composites, Fig. 11.20. For T300 composites the failure stress is only insignificantly higher, Fig. 11.21.

11.7 Test Procedure for Acoustic Emission Analysis

The monitoring of acoustic emission data during the loading of test specimens allows an assessment of the damage progression process and can thus contribute to the characterization of the type of laminate under evaluation. It is essential that this evaluation is based upon an AE parameter which not only indicates the occurrence of damage propagation qualitatively, but can be correlated in quantitative terms with its extent. Furthermore, the rate of data acquisition must not influence the interpretation of this parameter. Preliminary investigations have shown that the *energy content* of the AE events satisfies these requirements.

On this premise the cumulative AE energy $S(\epsilon)$ was plotted versus strain. Both the abscissa and the ordinate of the obtained diagrams were normalized:

$$\begin{aligned}\epsilon_{ult} &\rightarrow \epsilon_{ult,norm} = 1 \\ S(\epsilon_{ult}) &\rightarrow S(\epsilon_{ult,norm}) = 1\end{aligned}$$

The amount of energy released by the final fracture process itself was excluded because its absolute value would dominate the whole distribution and the measurement conditions would be distorted by the failing specimen.

11.8 Acoustic Emission Results

The normalized $S(\epsilon)$ -curves allow a direct comparison between the performance of different test specimens. From an engineering aspect, the optimal case is a small $S(\epsilon)$ -value up to imminent failure. This type of curve is approximately realized in Fig. 11.22(e). On the other hand, Fig. 11.22(a) demonstrates that considerable amounts of energy can be released by damage mechanisms already at very low strain values. The question was whether or not the different types of curves correspond to certain fiber/resin-combinations.

The AE energy release was pursued in detail for each test. The obtained results indicate that the initiation of the final failure process is indeed influenced by the matrix ductility. However, there is large scatter in the individual damage progression processes.

On a high strain level ($\epsilon_{ult} = 0.8$) NOL-rings made from ST3 and T300 fibers show a tendency of declining $S(\epsilon)$, i.e., less accumulated damage, when the ductility of the epoxy resin increases (see Figs. 11.23, 11.24). This tendency was not observed for HM45 specimens (Fig. 11.25).

In a number of tests, a spontaneous or step-like increase in the cumulative energy indicated the initiation of the final failure process at certain strain levels, which are depicted in

Figs. 11.26 and 11.27 for T300 and ST3 test specimens. NOL-rings made from HM45 fibers show a more continuous acoustic energy output under increasing load.

11.9 References

- [11.1] Dimmock, J., Prediction of composite properties
 Abrahams, M. from fibre and matrix properties.
 Composites (December 1969), pp.87-93

- [11.2] McMahon, F.E. The relationship between high modulus
 fiber and unidirectional composite
 tensile strength.
 19th SAMPE National Symposium and
 Exhibition Calif., 23-25 April 1974

- [11.3] Fitzer, E., Anorganische Fasern.
 Schlichting, J. Werkstofftechnik 11(1980), pp.330-341

- [11.4] Heinrich, W., Eigenschaften von feinstdrahtver-
 Nixdorf, J. verstärkten Kunststoffen.
 Wehr, W. Carl Hanser Verlag, München 1970

- [11.5] Kleiner, W., Ermittlung charakteristischer Werk-
 Lüßmann, W. stoffkenngrößen zum Berechnen von
 GFK-Wickelstrukturen unter betriebs-
 gerechten Bedingungen.
 Kunststoffe, Bd.59(1969) Heft 12,
 pp.941-947

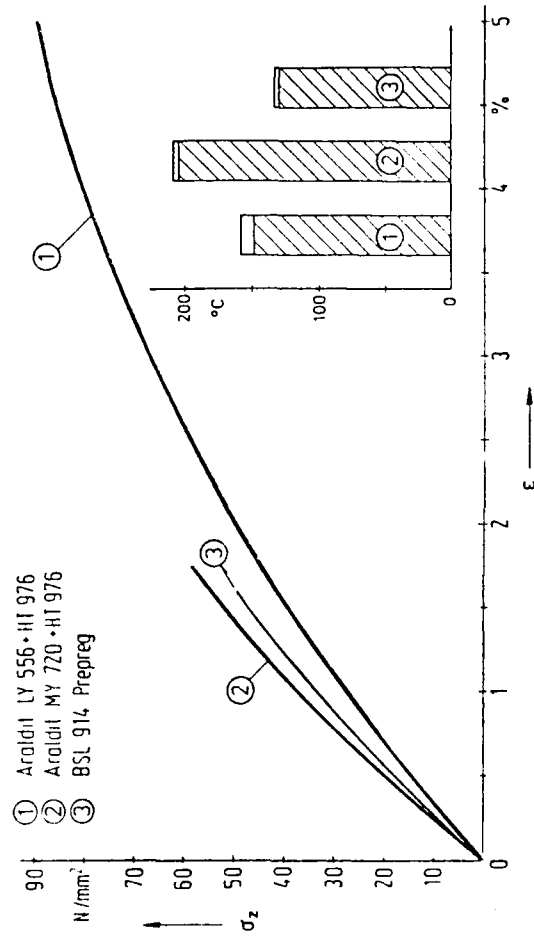


Fig. 11.1 Stress/strain plots and thermal stability of three epoxy resin types.

Property	T300-3000	ST-III-7-3000	HM-45-6000
Tensile strength N/mm ² , MPa	3100	4560	1860
Young's modulus kN/mm ² , GPa	248	247	454
Failure strain %	1,25	1,84	0,41
Density g/cm ²	1,74	1,77	1,90

Fig. 11.2 The typical properties of three types of carbon fibers.
(Specification of the manufactures)

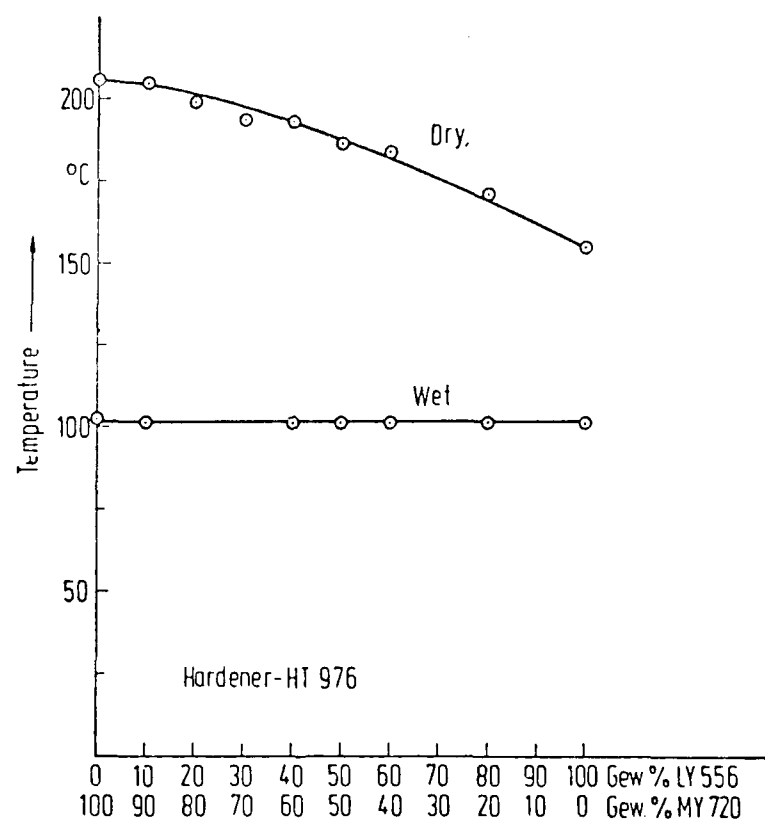


Fig. 11.3 Temperature of thermal stability of mixtures with MY 720 and LY 556 resins (DIN 53 458).

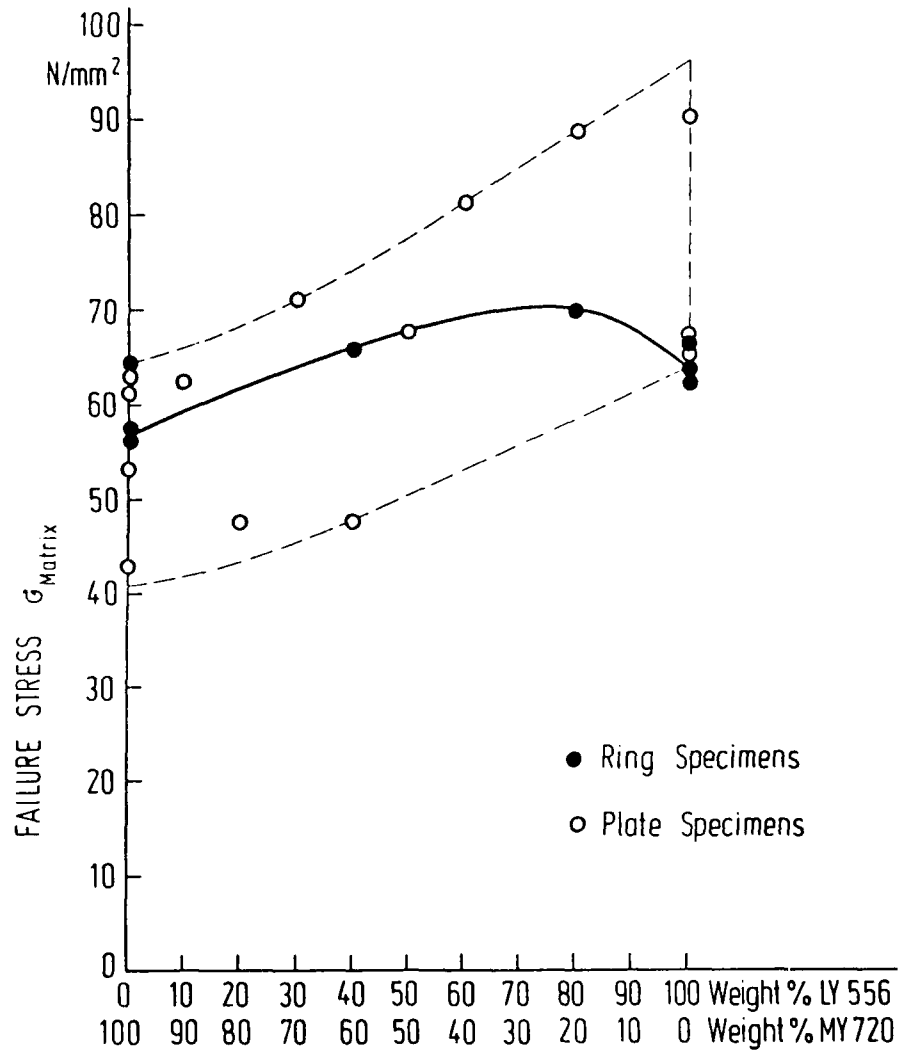


Fig. 11.4 Matrix failure stress depending on mixture ratio of the two resin components LY 556 and MY 720.

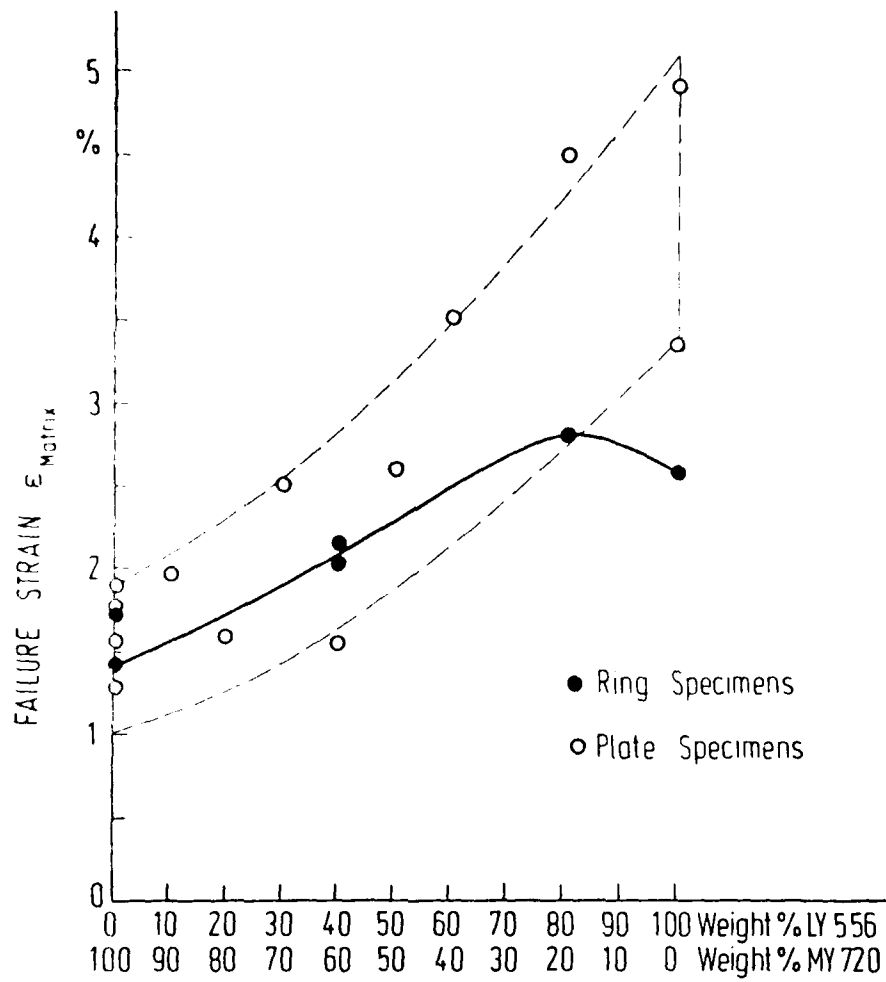


Fig. 11.5 Matrix failure strain depending on mixture ratio of the two resin components LY 556 and MY 720.

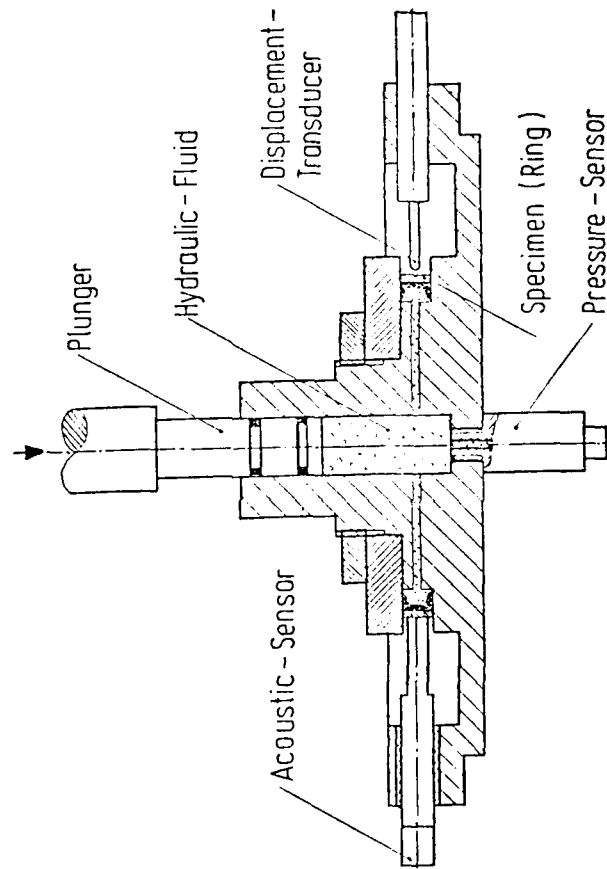


Fig. 11.6 Testing installation for NOL-ring loading

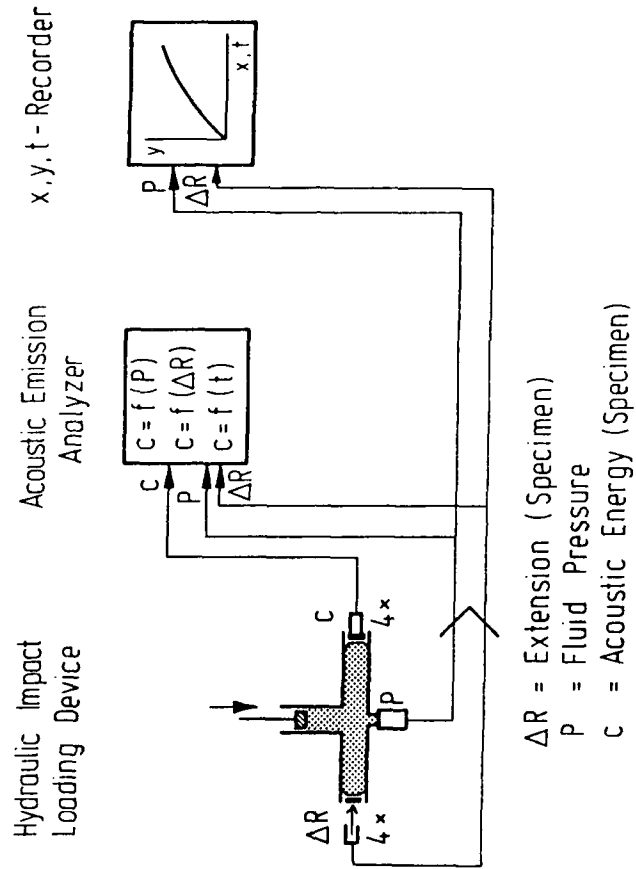


Fig. 11.7 Measuring equipment for hydraulic impact loading tests at low speed.

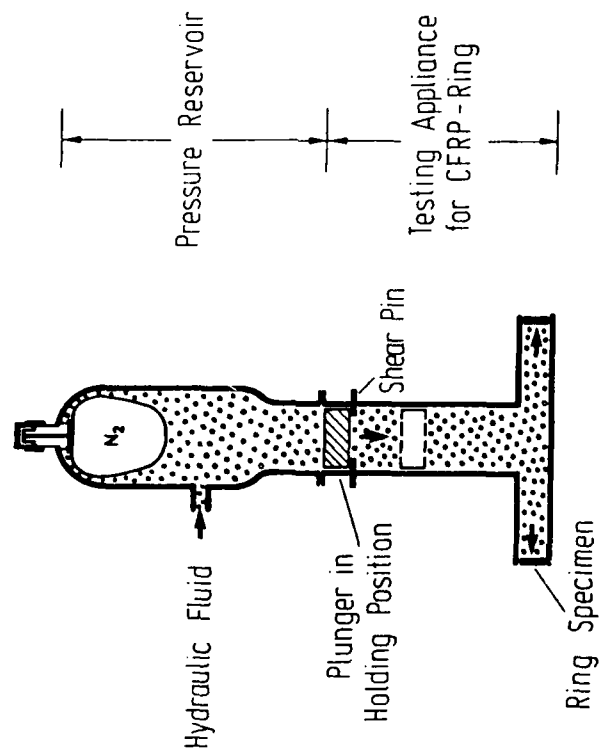


Fig. 11.8 Schematic of the test assembly for high speed loading of ring-specimens.

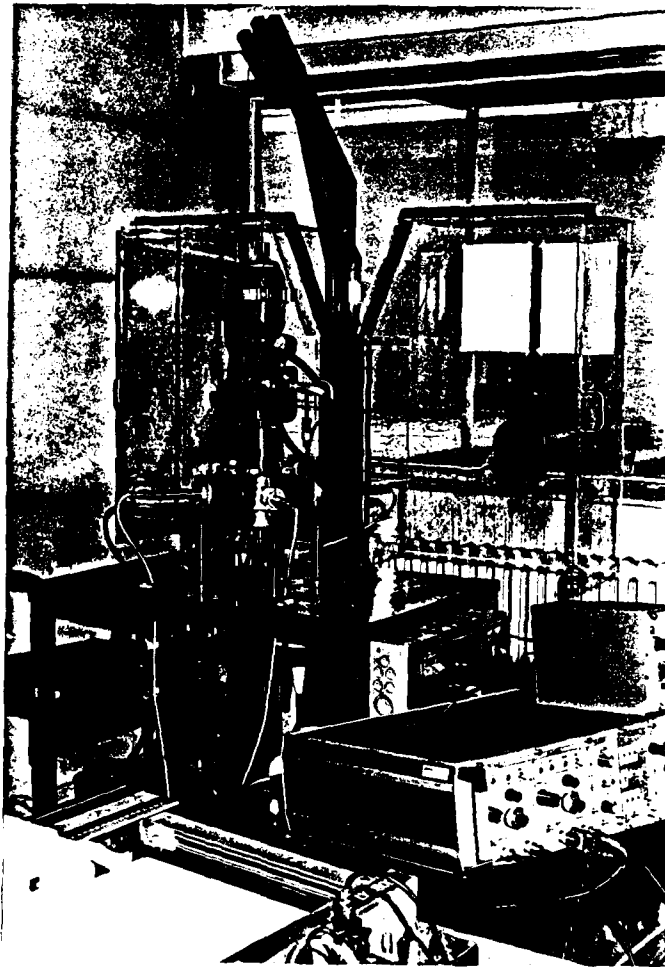


Fig. 11.9 Test set-up for high speed loading of ring specimens.

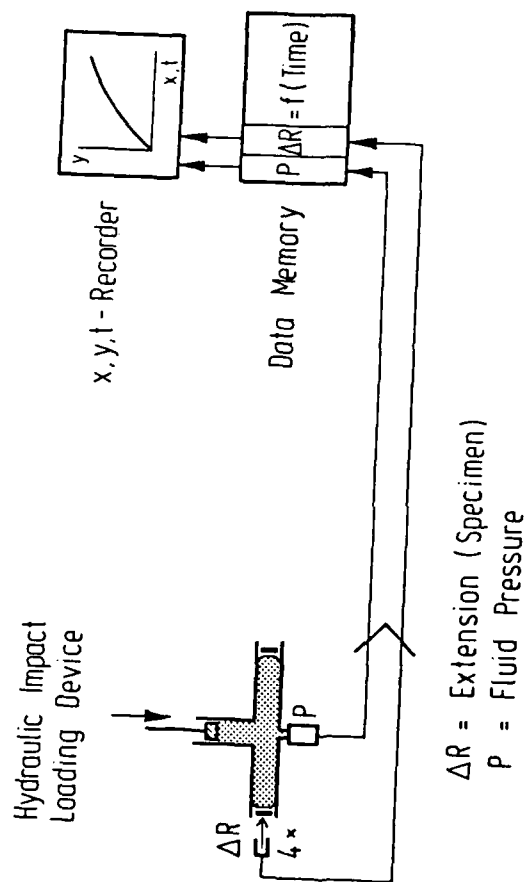


Fig. 11.10 Measuring equipment for high speed hydraulic impact loading tests.

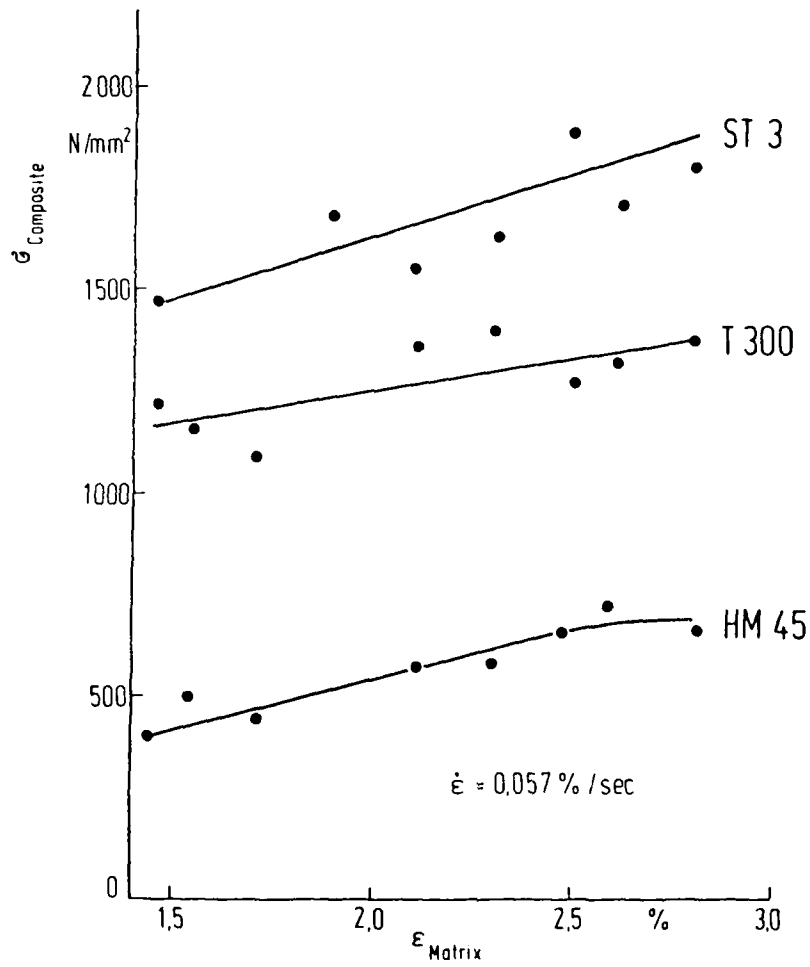


Fig. 11.11 Failure stress of CFRP-rings at a strain rate of 0.057 %/sec vs. failure strain of different matrices.

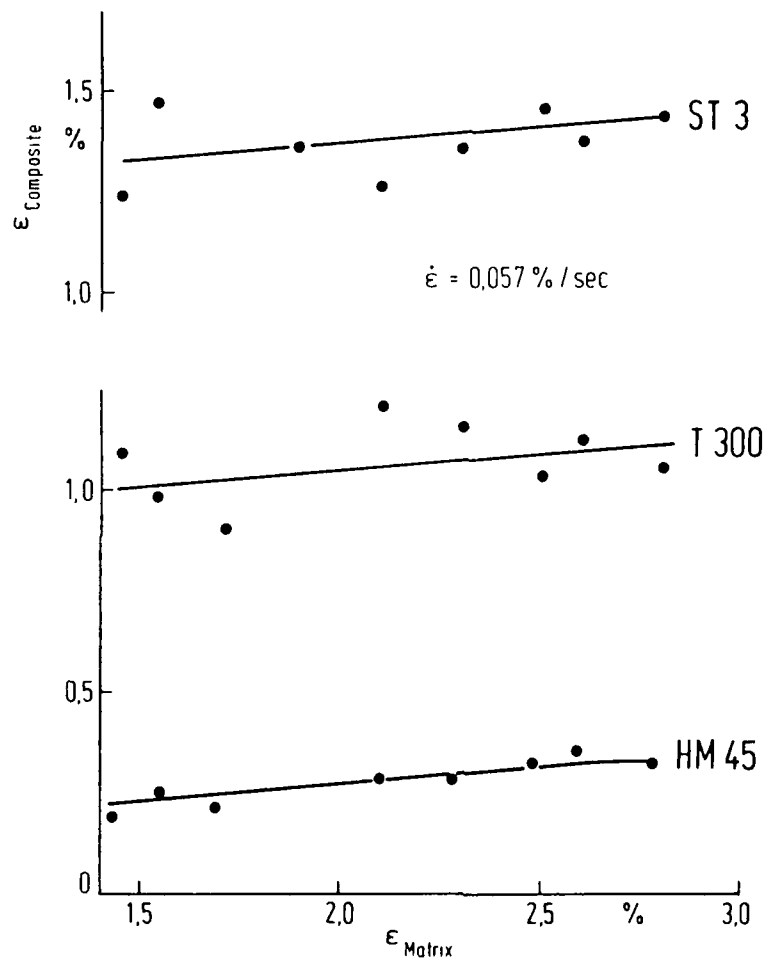


Fig. 11.12 Failure strain of CFRP-rings at a strain rate of 0.057 %/sec vs. failure strain of different matrices.

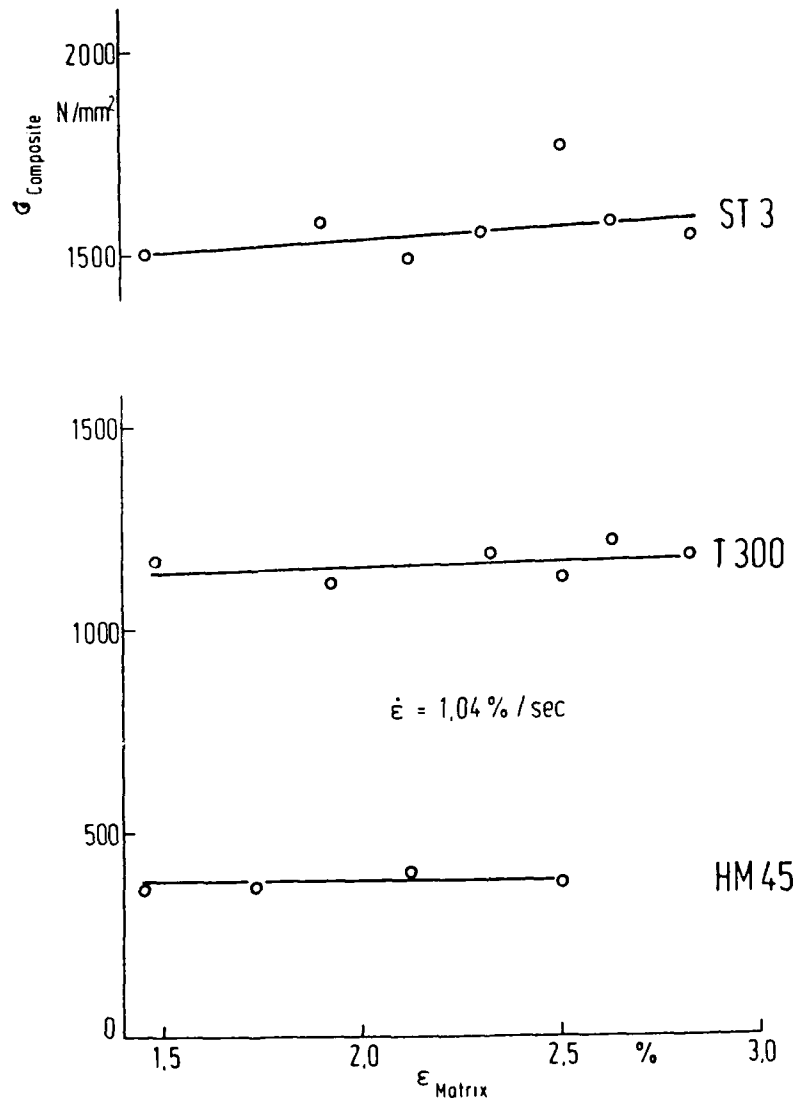


Fig. 11.13 Failure stress of CFRP-rings with a strain rate of 1,04 %/sec vs. failure strain of different matrices.

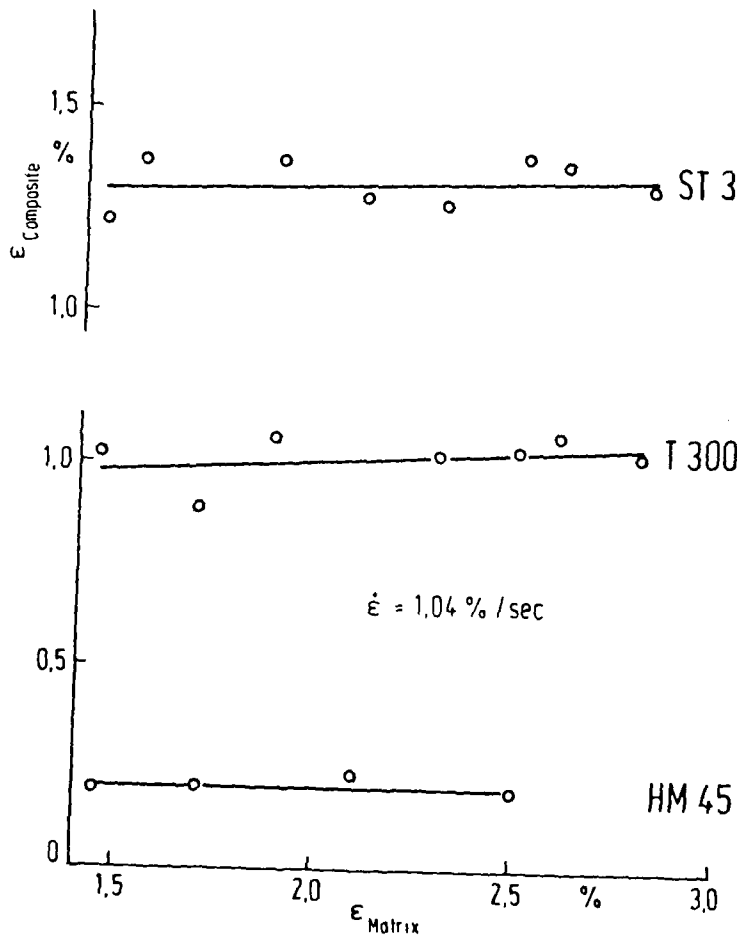


Fig. 11.14 Failure strain of CFRP-rings with a strain rate of 1,04 %/sec vs. failure strain of different matrices.

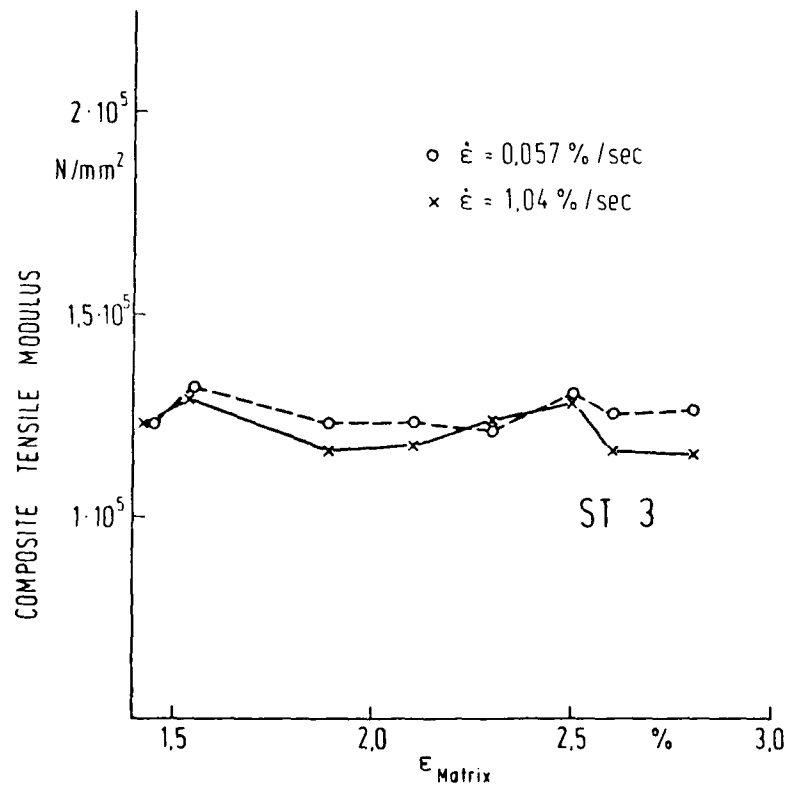


Fig. 11.15 Tensile modulus of CFRP-rings vs. failure strain of different matrices.

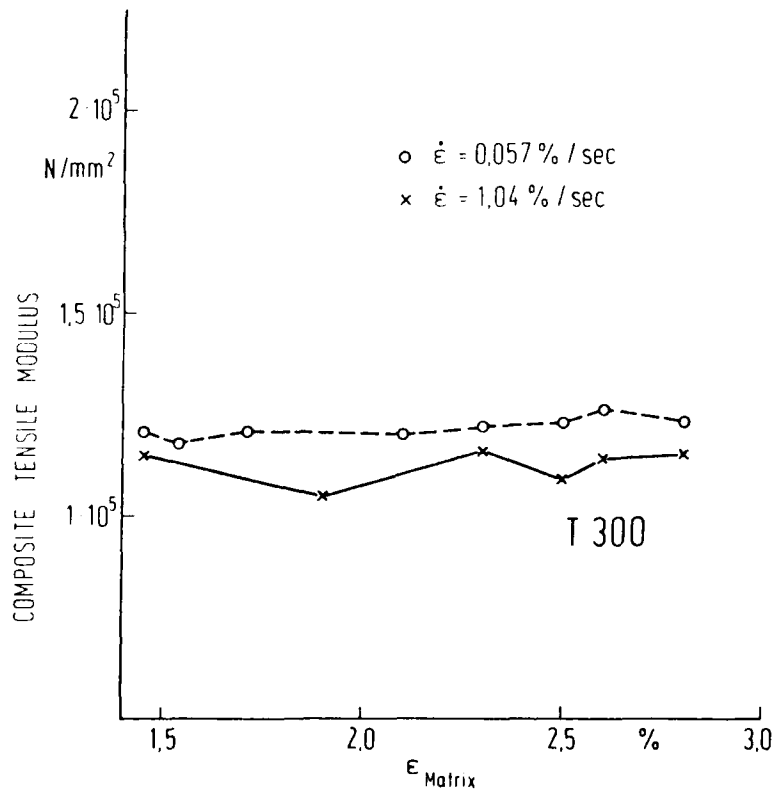


Fig. 11.16 Tensile modulus of CFRP-rings vs. failure strain of different matrices.

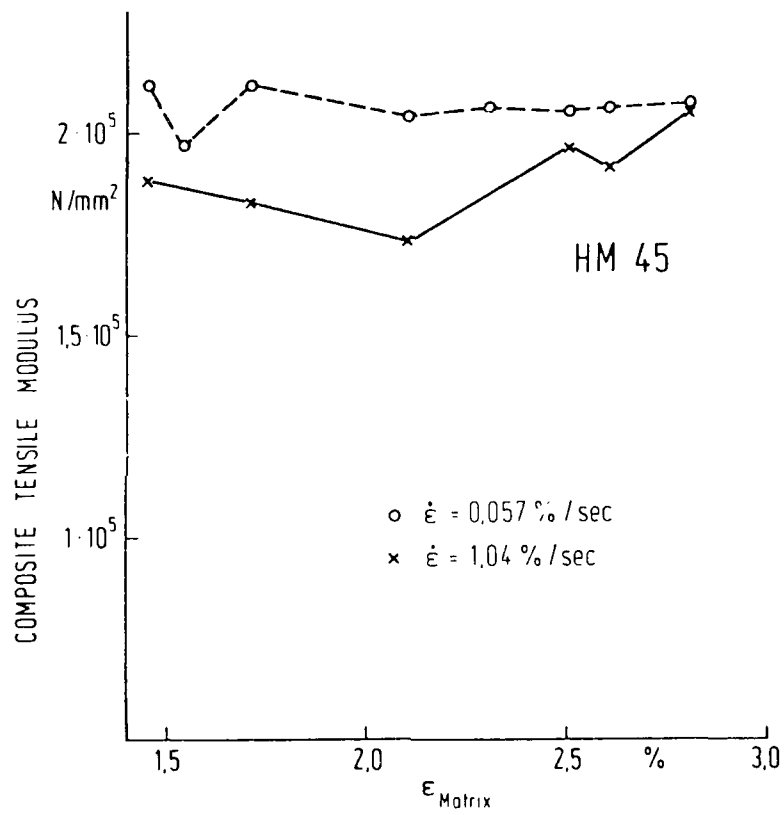


Fig. 11.17 Tensile modulus of CFRP-rings vs. failure strain of different matrices.

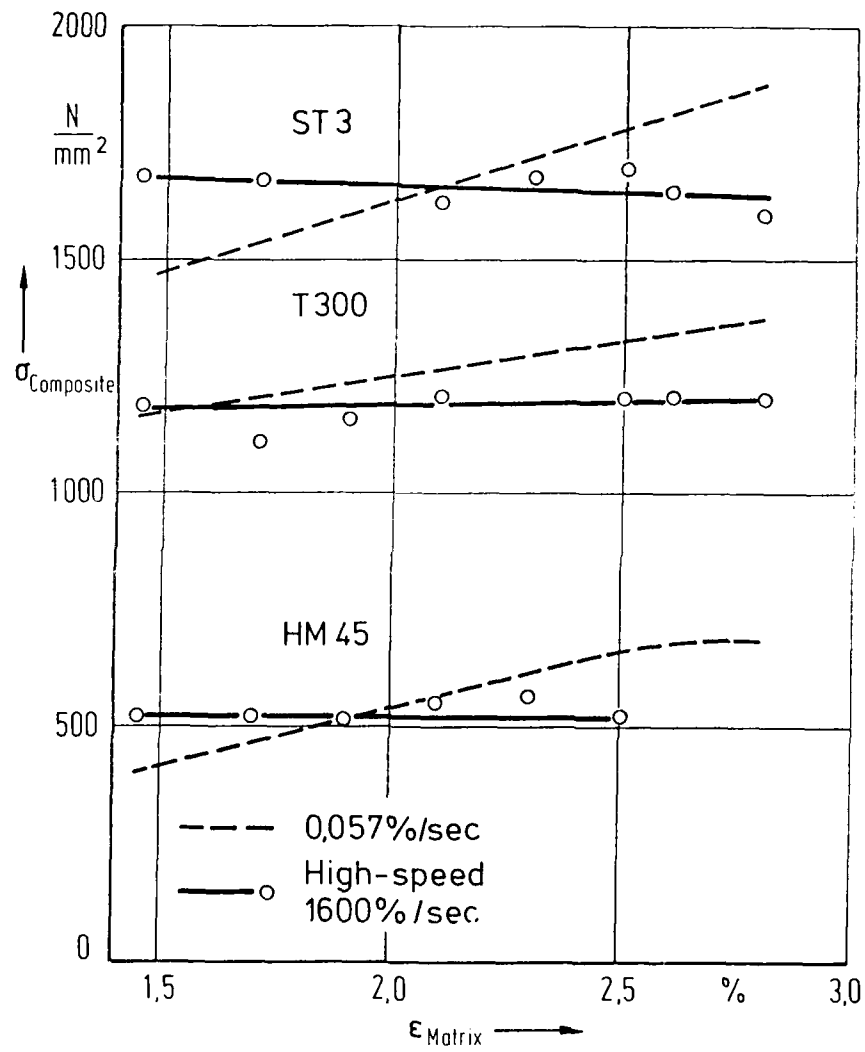


Fig.11.18 Failure stress at high and low speed loading of the variety of ring specimens.

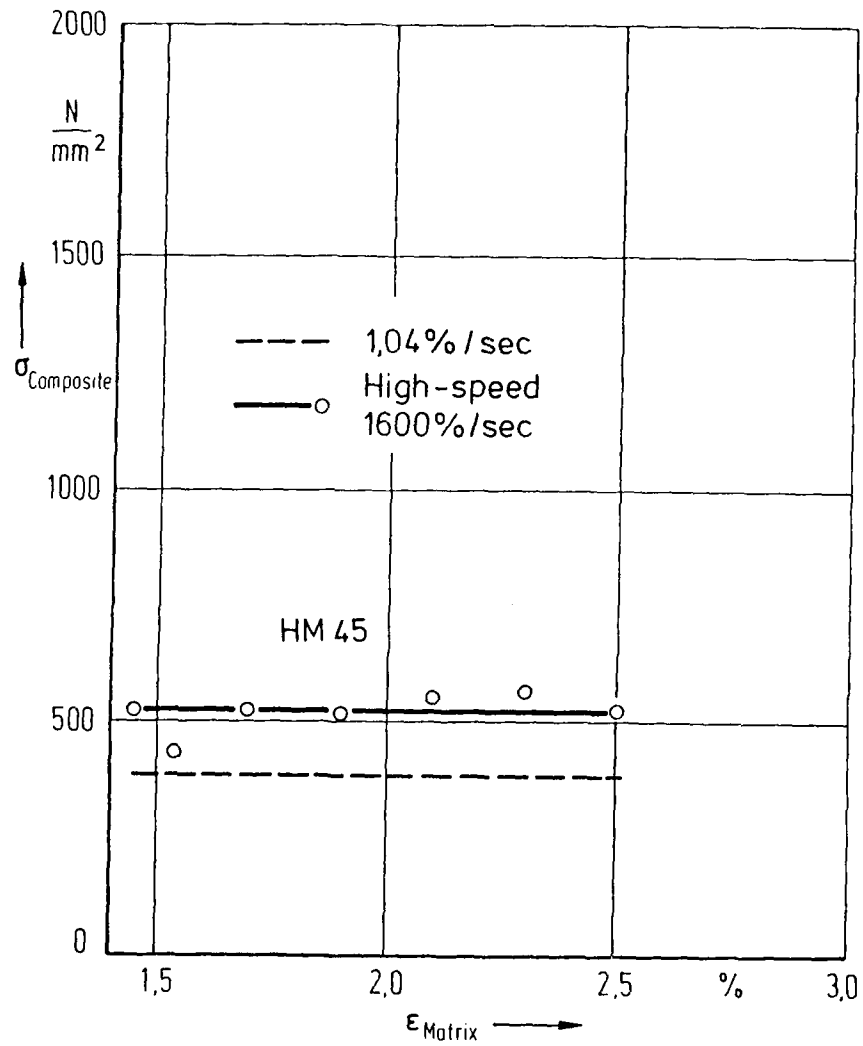


Fig.11.19 Failure stress of HM 45 ring specimens at strain rates of 1600 %/sec and 1,04 %/sec.
(average of two tests at high strain rate)

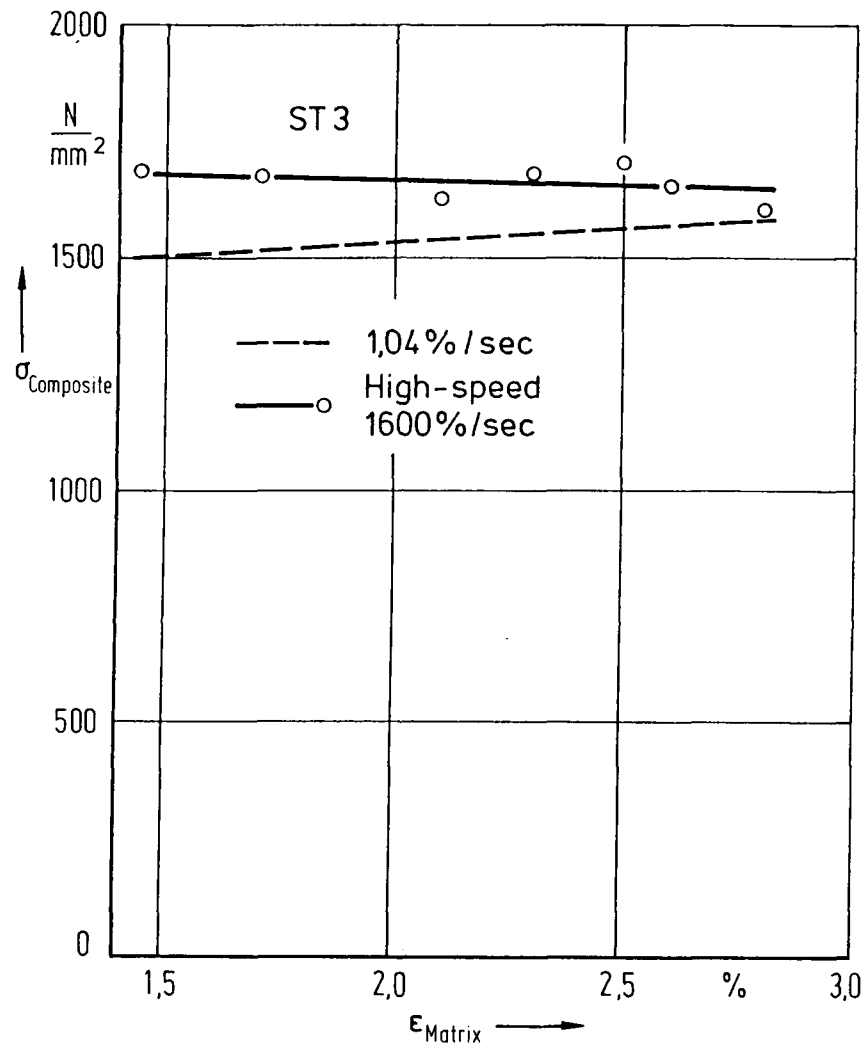


Fig.11.20 Failure stress of ST 3 ring specimens at strain rates of 1600 %/sec and 1,04 %/sec.
(average of two tests at high strain rate)

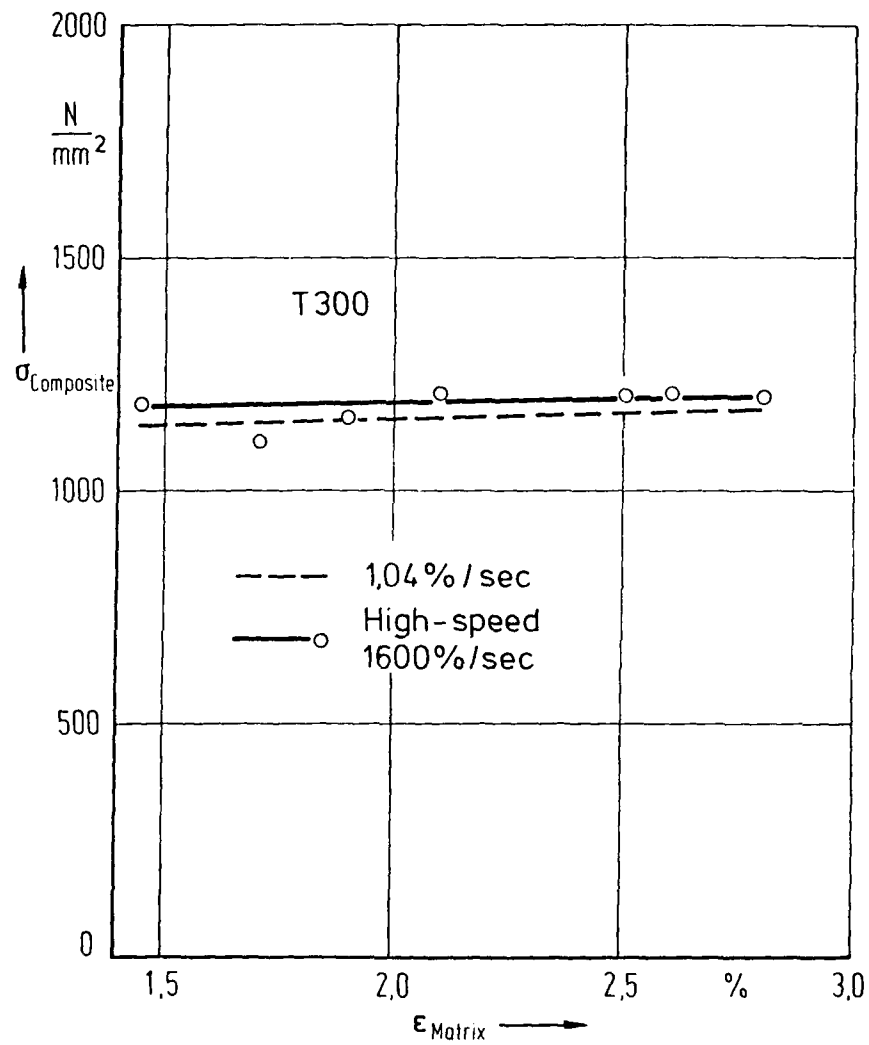


Fig.11.21 Failure stress of T 300 ring specimens at strain rates of 1600 %/sec and 1,04 %/sec.
(average of two tests at high strain rate)

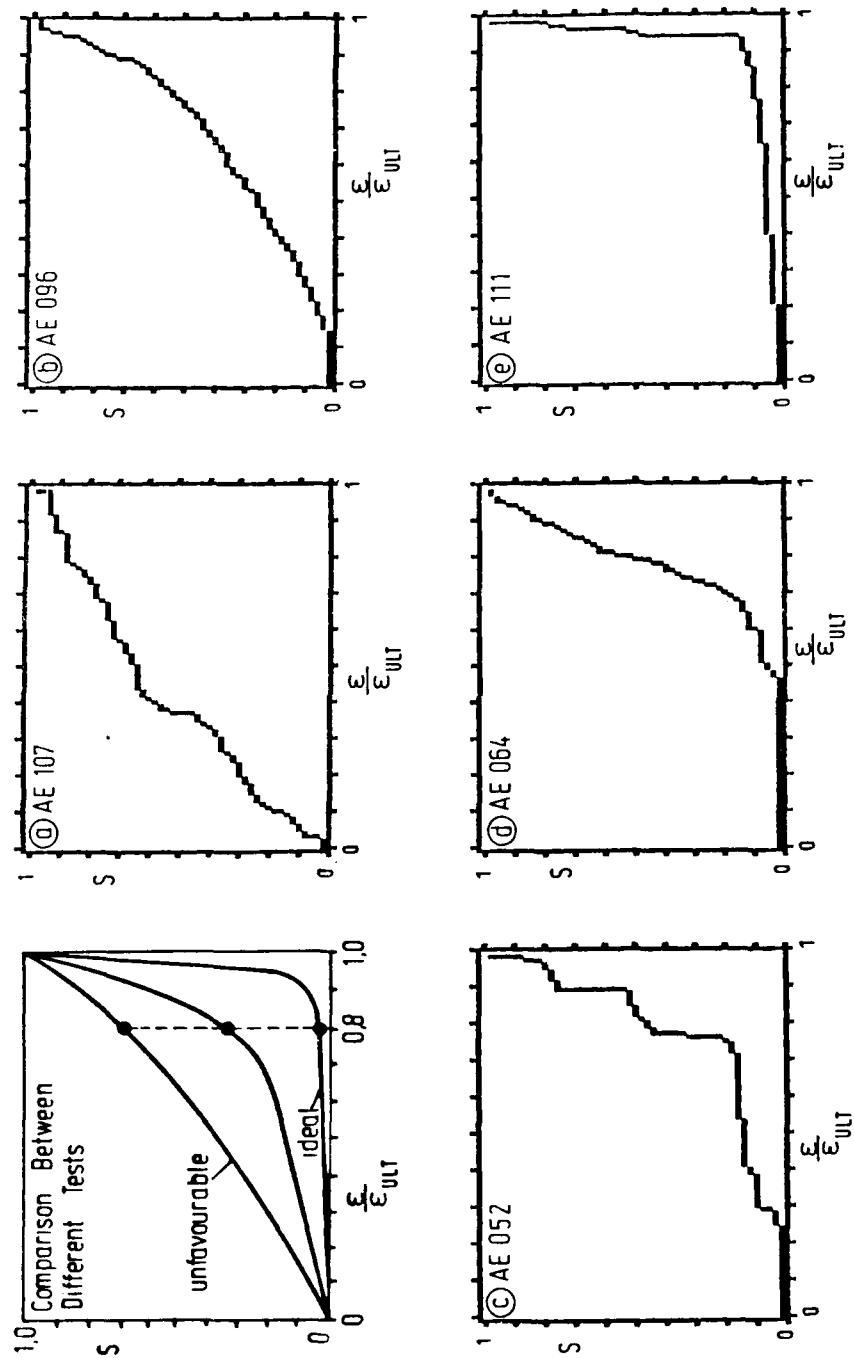


Fig. 11.22 Cumulative acoustic energy output S during loading of CFRP-rings by internal pressure.

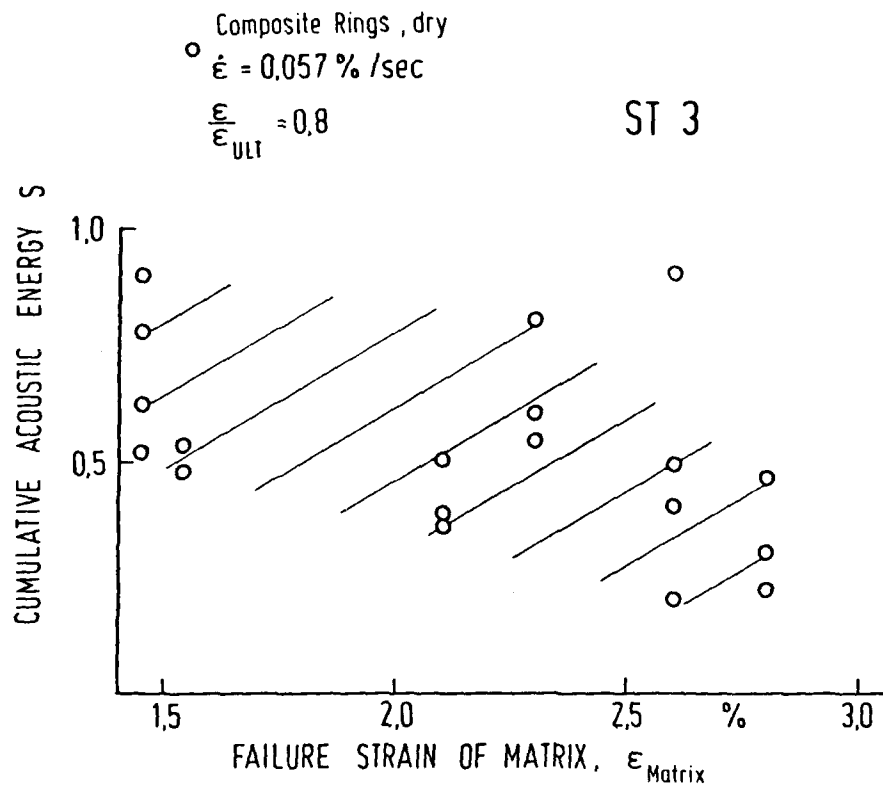


Fig. 11.23 Cumulative acoustic energy output of CFRP rings with different matrices at 80% of failure stress. (The shaded area represents a general tendency found in the entire set of tests with ST 3)

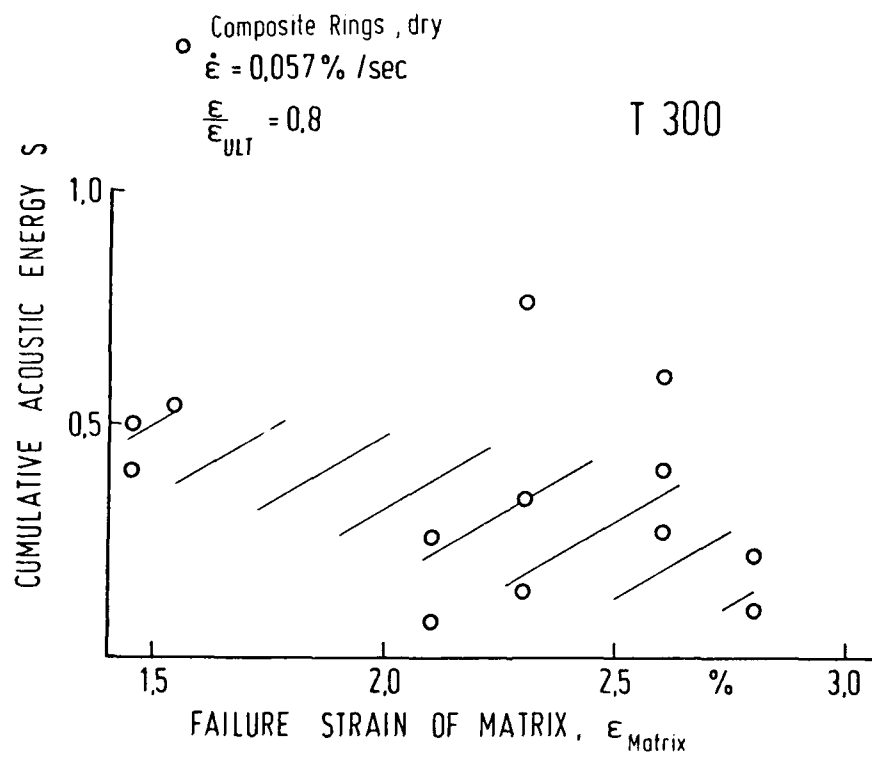


Fig. 11.24 Cumulative acoustic energy output of CFRP rings with different matrices at 80% of failure stress. (The shaded area represents a general tendency found in the entire set of tests with T 300)

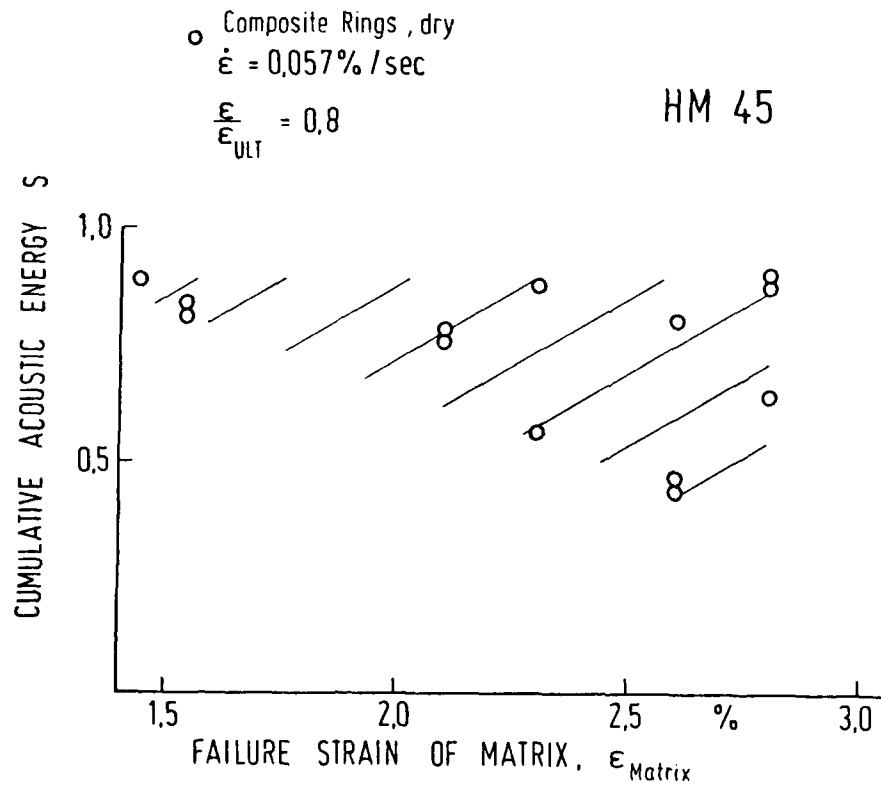


Fig. 11.25 Cumulative acoustic energy output of CFRP rings with different matrices at 80% of failure stress. (The shaded area represents a general tendency found in the entire set of tests with HM 45)

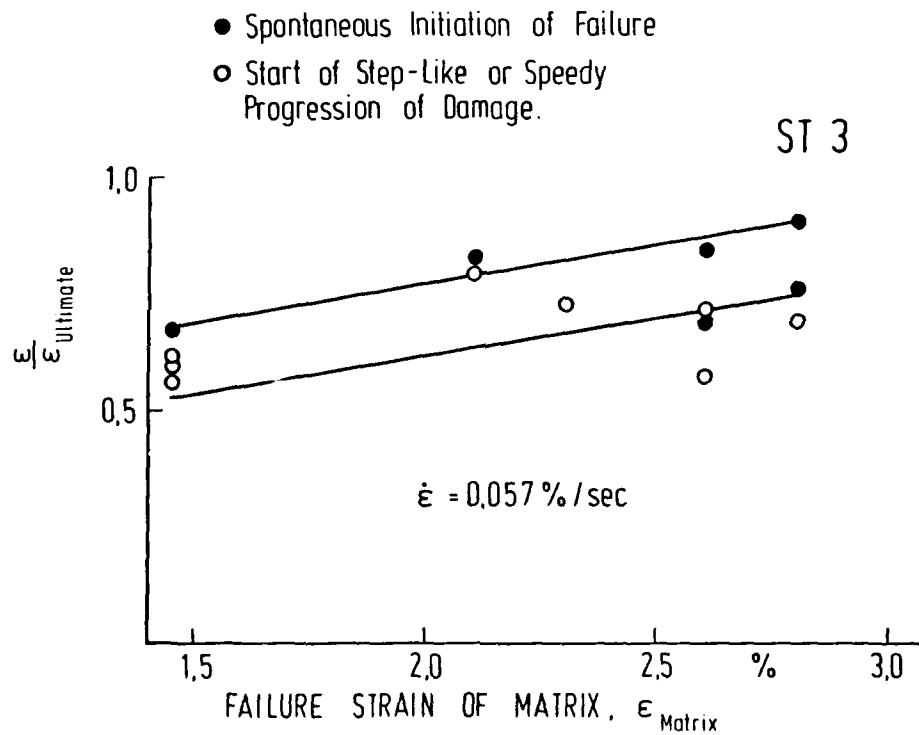


Fig. 11.26 Range of spontaneous initiation of failure in CFRP rings determined by acoustic energy output.

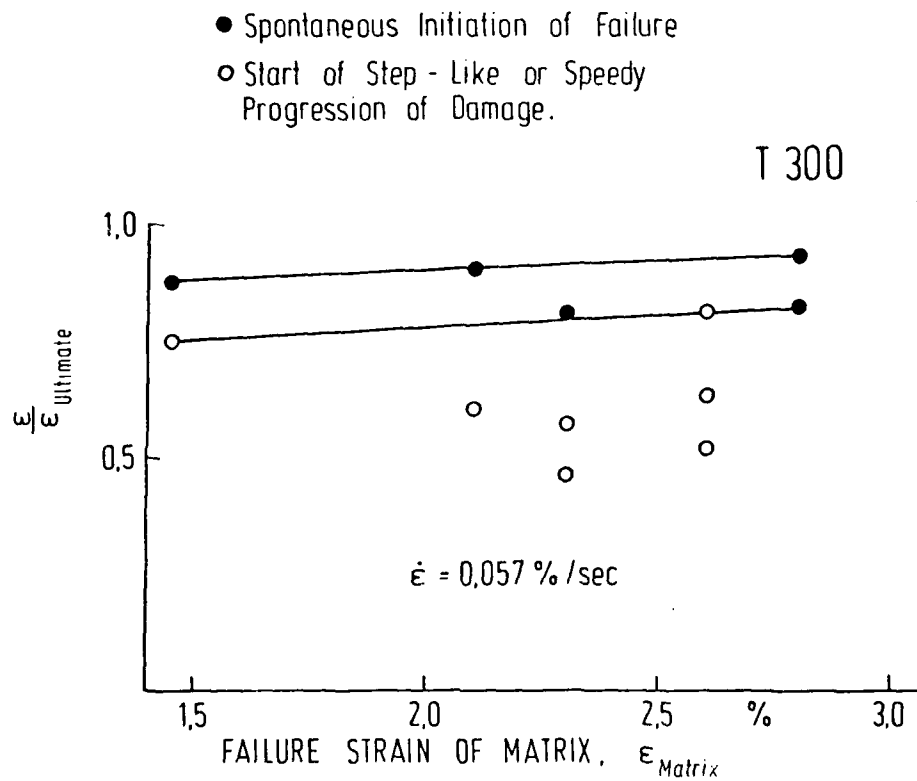


Fig. 11.27 Range of spontaneous initiation of failure in CFRP rings determined by acoustic energy output.

12. RADIATIVE AND OXIDATIVE EFFECTS

12.1 Summary

Carbonfiber-reinforced epoxy resins are susceptible to impairment of their mechanical properties in radiative and oxidative environments. A limited attempt has been made to assess the magnitude of degradation in three specific cases. A realistic simulation of electron beam irradiation as experienced during the service life of a spacecraft structure in a typical geostationary orbit showed that neither the tensile strength nor the elongation to failure of 1 mm thick laminates were impaired after 3×10^8 rads. A slight reddish tint on the laminate surfaces may be indicative of optical property changes. The long-time exposure of test specimens to open atmospheric conditions in 75 m and 1600 m elevation led to the observation of matrix cracks and obvious deteriorations of the laminate surfaces. The direct cause was surmised to be UV-B type irradiation, aided by the presence of both moisture and oxygen. Following an initial increase of the tensile strength it subsequently diminished continuously to 90% of the initial strength after an irradiation dose of 2000 J/cm² which is roughly equivalent to three calendar years. A clearly oxidative effect was observed on test specimens which were subjected to a sustained temperature of 120°C in the presence of air. The measured weight loss of 914C/T300-laminates was 3.3% after 28900 hours and continuing. At a sustained temperature of 100°C the rate of weight loss was considerably less but had an equally continuing trend. Optical investigations revealed no changes in the surface texture of the test specimens. It is recognized that in rarefied regions of the atmosphere the presence of atomic oxygen presents a more serious threat. However, this condition is difficult to simulate in ground-based facilities and may have to be evaluated in appropriate altitudes.

12.2 Effect of Electron Irradiation

In the course of their service lives, space structures may be subjected to various kinds of irradiation. The potential degradation of the mechanical properties of carbonfiber-reinforced laminates

will depend on the nature and duration of the irradiation exposure. The effect of electron beam irradiation on the tensile strength and stiffness of $[\pm 45]_{2s}$ -laminates made from the three different material systems shown in Fig. 12.1 was investigated in some detail.

Rectangular test specimens of 65 mm width and 195 mm length were first irradiated in a Van der Graaf accelerator at the University of Illinois at 100° C in a 10^{-4} Pa vacuum. With a beam current of 165 μ A held for approximately 27 hours a total of 3×10^8 rads was applied which corresponds to at least twice the dose a space structure in a geostationary orbit will experience during a ten years service life. After the electron beam irradiation a visual inspection of the test specimens indicated no degradation of the surface texture; however, a slight reddish discoloration was noted on the specimen surfaces facing the irradiation source.

The laminates were subsequently dissected into 10x110 mm parallel-sided tensile test specimens and statically loaded to failure. A comparison of their tensile strengths and elongations at failure with corresponding values obtained from non-irradiated specimens showed only minor differences which may be attributable to data scatter. The test results are summarized in Fig. 12.1. From a structural point of view the effects of electron beam irradiation may be considered negligible.

12.3 Effect of UV-Irradiation

Moderate exposure of epoxy resins to UV-irradiation seems to cause additional cross-linking of the polymers and is in that sense beneficial. Higher doses of irradiation, however, tend to break down the polymer chains which leads to a degradation of the epoxy resins and a reduction of their molecular weight. The study of these effects was limited to UV-B type irradiation which, in contrast to UV-C irradiations, is capable of reaching the earth's surface. The test specimens were 1 mm thick epoxy laminates reinforced with different kinds of fibers in fabric form with approximately equal fiber volume contents. The specimens were exposed at 75 m and 1600 m elevation to the open atmosphere in

order to include the potentially negative influences of atmospheric oxygen and moisture. In view of the unstable climate it seemed to be prudent to interpret the results in terms of the amount of UV-B irradiation rather than in calendar months. The corresponding calculations were based on measurements of the global irradiation with a solarimeter [12.1].

In certain intervals, specimens were removed from the test sites and subjected to static tension tests in order to determine their residual strength. The test results are summarized in Fig. 12.2 in the form of residual tensile strength versus amount of UV-B irradiation [12.2]. In all laminates an initial slight strength increase is followed by a more or less substantial strength degradation. Microscopic investigations disclosed matrix cracks within the surface of the laminates which increased in number and branched out in several directions. In this process resin particles on the specimen surfaces were isolated and afterwards flaked off, as shown in the bottom part of the figure. Photograph 1 was made before outdoor weathering, photographs 2 and 3 after one and two years of exposure, respectively.

12.4 Effect of Oxidation

The influence of the environment on the performance characteristics of carbonfiber-reinforced resins is a well known phenomenon. Sustained exposure to elevated temperatures, for example, can lead to irreversible changes in the composition of epoxy resins. A convincing indication of such changes is the weight loss observed in 914 C/T300 and Code 69/T300 laminates subjected, in two test series, to long-time exposure at constant temperatures of 100°C and 120°C for up to 28900 hours. The heating of the test specimens took place under normal atmospheric conditions in separate 100°C- and 120°C- ovens, where the gas exchange in the two ovens was accomplished by a daily pumping action, and by continuous ventilation, respectively. The number of test specimens was five for each material for the 100°C- tests, and two for the 120°C- tests, collected from different material batches. The dimensions and dry weights of the specimens are given below. The

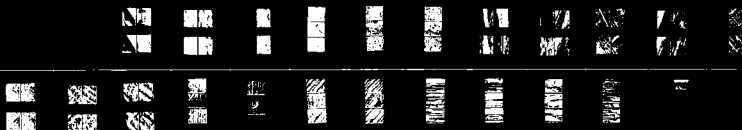
AD-A168 003

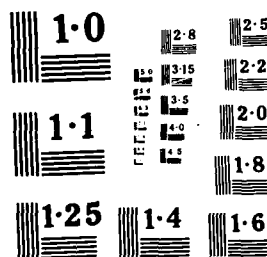
DEVELOPMENT OF FRACTURE MECHANICS MAPS FOR COMPOSITE
MATERIALS VOLUME 2 (U) DEUTSCHE FORSCHUNGS- UND
VERSUCHSANSTALT FUER LUFT- UND RAUMF. H W BERGMANN
DEC 85 AFMML-1A-85-4158-VOL-2 P/G 11/4

2/3

UNCLASSIFIED

NL





dry weights were established after exposure of the specimens to 70°C for 55 hours.

	Dimensions [mm]	Dry Weights [g]
100°C		
914 C	114×10×1	1.65 - 1.68
Code 69	114×10×1	1.54 - 1.57
120°C		
914 C	100×50×1	7.33 - 7.38
Code 69	100×50×1	6.88 - 7.18

Fig. 12.3 shows the functional relationship between exposure time and weight reduction which, evidently, does not reach terminal values. According to the figure the reduction in temperature from 120°C to 100°C leads to a significantly lower rate of weight loss especially in the 914 C/T300 material.

Independent tests at the NASA-Ames research center confirmed the suspicion that the weight reduction is caused by an oxidative process. Neat epoxy resins were exposed to high temperatures in vacuum and out of vacuum. A weight loss, accompanied by a drastic reduction of stiffness, was observed only in specimens tested under atmospheric conditions. Apparently, the products of the oxidation process leave the resins in a gaseous state by diffusion, so that the weight loss becomes noticeable only after extended periods of time.

12.5 References

- [12.1] Seifert, H.-J. Ein Beitrag zu Alterungsunter-
suchungen an Textilien.
IB 152-75/15 DFVLR.
- [12.2] Niederstadt, G. Einfluß von Umweltbedingungen
auf Verbundwerkstoffe des Flugzeugbaues.
Kunststoffberater 12, S. 25-29
Dezember 1982.

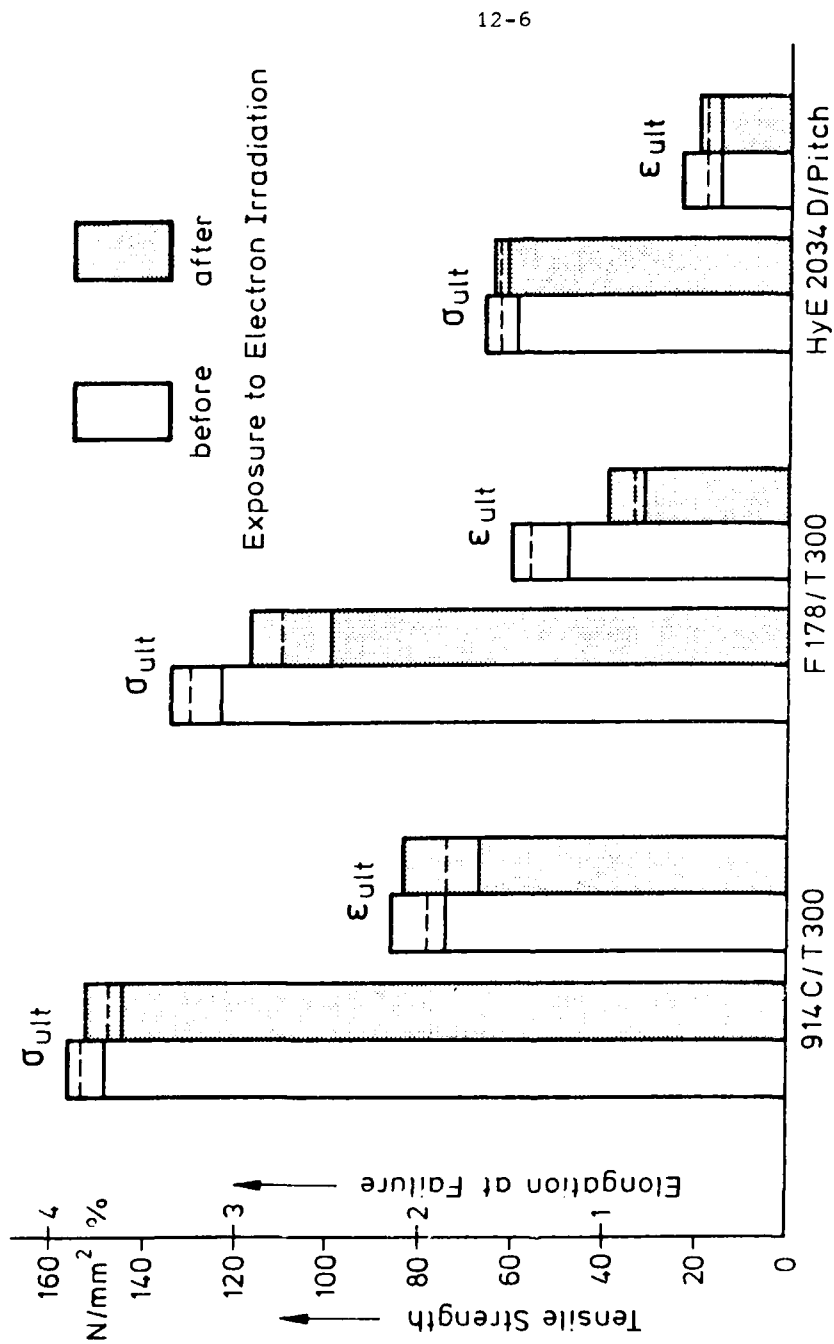
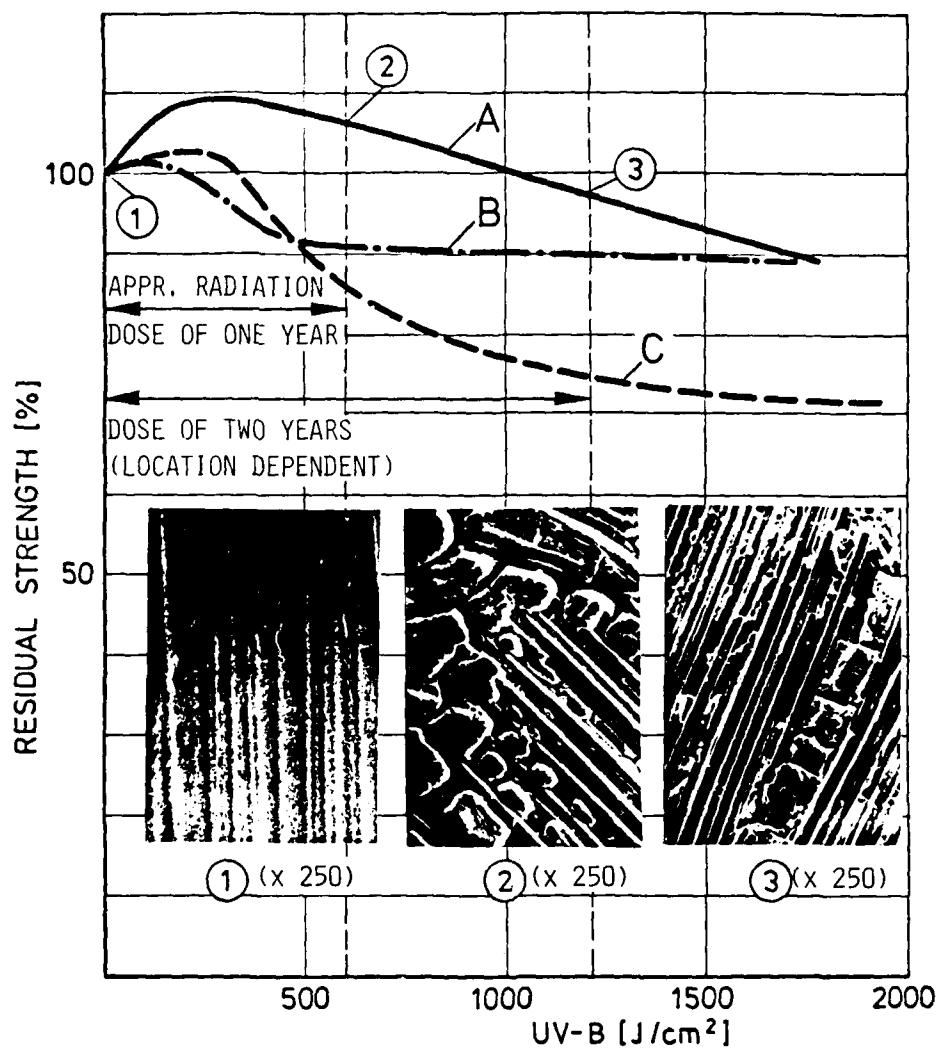


Fig. 12.1 Degradation of the mechanical properties due to electron irradiation.



MATERIAL

REINFORCEMENT
(0/90)

A: CARBONFIBER FABRIC
B: GLASSFIBER FABRIC
C: ARAMIDFIBER FABRIC

MATRIX

(A,B,C): ALIPH. EPOXY-RESIN CURED WITH
CYCLOALIPH. AMIN

CURING PROCESS

: 1,5 h 90°C/6 h 100°C

THICKNESS

: AVERAGE 1mm

Fig. 12.2 Degradation due to UV-B Irradiation,

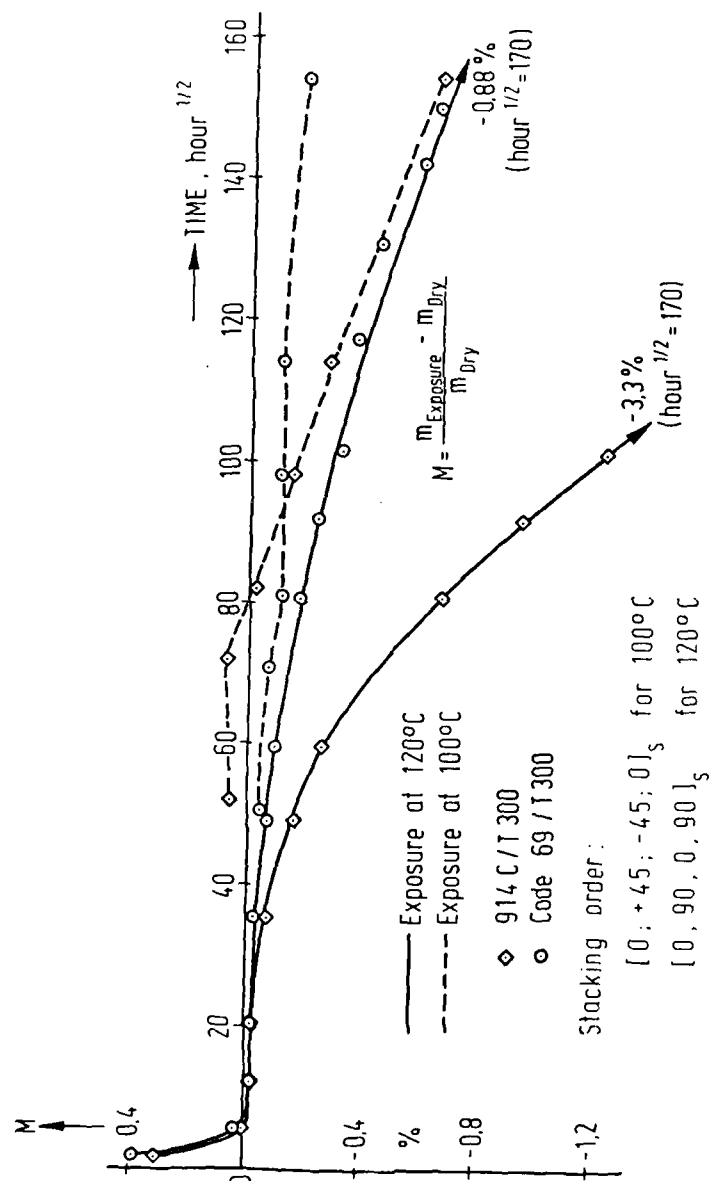


Fig. 12.3 Weight loss of carbonfiber-reinforced epoxy resins during long time exposure in air at 100°C and 120°C.

13. FRACTOGRAPHICAL INVESTIGATIONS

13.1 Summary

Laminates made of carbonfiber-reinforced epoxy resins exhibit, under increasing tensile loads, three different kinds of failure modes: rupture of individual fibers, microcracks in the matrix, and loss of adhesion at the fiber-matrix interface. These initially microscopic failure modes, occurring singly or in combination, degrade the mechanical properties of the laminate and may lead to total fracture. By means of a fractographical evaluation of the fracture surfaces it was attempted to gain insight into the mechanisms which initiate and perhaps control the three fracture modes. It became soon apparant, however, that the topography of the fracture surfaces is not only affected by the nature or sequence of the dominant failure modes but also by such parameters as moisture content, variations of curing process, and different stacking orders or strain rates. For that reason it has not yet been possible to develop the same comprehensive understanding of failure mechanisms for composite materials as it already exists for metals. In view of the complexity of the issue the efforts commenced with the failure modes analysis of BSL 914 epoxy resins and proceeded to the investigation of environmental effects in uni- and multidirectional laminates made of Fiberdux 914C/T300 and Code 69,T300 materials. The topography of the fracture surfaces of the tension-loaded neat resin was seen to depend on the curing process as well as on the moisture content. In curing cycles with low heating rates the formation of microcracks was observed. Both the curing cycle and the moisture content affect the strain capability of the resin, as can be qualitatively recognized in the fracture surfaces. A clear distinction between the two phenomena could not yet be made. With a known curing cycle, however, it is possible to deduce the moisture content of a specimen or, with a known moisture content, the nature of the curing cycle. In regard to fiber-reinforced laminates it became evident that the influence of different curing cycles, of test temperature and of moisture content on the matrix microstructure and on the fiber-matrix interface are identifiable. A

first attempt to quantify the fiber-matrix adhesion in terms of the mean length of the pulled-out fibers is promising.

13.2 Description of Test Equipment

The microfractographical investigations were performed with a scanning electron beam microscope of the type Philips SEM 505 capable of a resolution down to 6 nm. The beam voltage is variable between 1 and 30 kV and the magnification is adjustable up to 160×10^3 . The diameter of the electron beam on the object can be varied between 4 and 1000 nm. The image of the fracture surface is produced simultaneously on a viewing monitor and on a photographic monitor by a secondary electron detector and a video unit. The depth of field is 0.34 mm at a magnification of 100, and 1.2 μm at a magnification of 10 000. The test specimens are positioned on a goniometric table allowing translation and rotation.

For the quantitative evaluation of the photographic images a semiautomatic photo interpreter permitted, under manual scanning, the count and measurement of individual picture elements, their statistical treatment and the representation of characteristic quantities in terms of cumulative distribution diagrams.

13.3 Investigation of Epoxy Resins

The appearance of the fracture surfaces of laminates is influenced by a multitude of parameters. Their proper interpretation can be simplified by an initial evaluation of the characteristics of the unreinforced resin system. Consequently, the investigations began with a study of the effects of different moisture contents and different curing cycles on the fracture surfaces.

13.3.1 Influence of Moisture Content

Figs. 13.1 through 13.10 display fracture surfaces of Ciba BSL 914 test specimens subjected to tensile loads. The data line at the bottom of the figures contains, as the third entry, the magni-

fication in exponential form, i.e., the designation 1.06 E1 in Fig. 13.1 signifies a magnification of 10.6. The odd-numbered figures display the fracture surfaces of dry test specimens under increasing magnification and the even-numbered the fracture surfaces of test specimens saturated at 93% relative humidity. Figs. 13.1 and 13.2 show the fracture surfaces of dry and moist specimens magnified ca.10. Already here different patterns of elevations and suppressions are noticeable which become more pronounced at magnification 50 in Figs. 13.3 and 13.4, indicating different degrees of ductility. In the upper half of Fig. 13.4 fracture parabolas can be recognized similar in appearance to those occurring at high static loads in metals. The fracture surfaces of the dry specimen with their flat and uniform topography, in comparison, signify lack of ductility in the resin. At a magnification of 500 (Figs. 13.5 and 13.6) the fracture surfaces have a flake-shaped appearance, more pronounced in the moist specimen and thereby supporting the contention of higher ductility of the resin in the presence of moisture. This reasoning is in accord with macroscopic measurements of the strain to failure, ϵ_{ult} , which is twice as high in the moist specimen (2.7%) than in the dry specimen (1.35%).

At magnifications of 2000 (Figs.13.7 and 13.8) and 4000 (Figs. the microstructure of the matrix becomes more apparent. It is composed of spherically shaped and interconnected elements whose diameters increase with increasing moisture content. This configuration may be influenced by the presence of polysulfon in the BSL 914 epoxy resin.

13.3.2 Influence of Curing Cycle

Figs. 13.11 through 13.19 show the topography of the fracture surfaces of BSL 914 tensile specimens cured under the substantially different curing cycles identified on the right-hand side of the figures. The specimens were statically loaded to failure in a completely dry condition. According to Figs. 13.11 and 13.12 the texture of the fracture surface of specimens cured at a high heating rate (4°C/min to 170°C, 4 hrs constant at 170°C) is more coarsely grained than that cured at a low heating rate (0.8°C/min,

4 hrs constant at 170°C). The topography of specimens cured at low heating rates also exhibits flakes and cracks suggesting a higher strain capability. Macroscopic measurements, however, yielded similar values of elongation at failure and did not support that suggestion.

Fig. 13.13 shows the fracture surface of a specimen cured with a heating rate of 2°C/min and subsequent hold times of 3 hrs at 120°C and 4 hrs at 170°C. The topography displays medium grain sizes and uniform elevations and depressions.

More distinct differences of the fracture surfaces become apparent at a magnifications of 2 000 and 5 000 (Figs. The sphere-shaped elements of the microstructure, typical for the BSL 914 resin system, differ in size and are larger in the latter curing cycle. The macroscopically measured elongation at failure is also the highest for this case.

13.4 Investigation of Statically Loaded Laminates

The failure mechanisms of multidirectional laminates are affected by a variety of parameters. Their proper interpretation mandates the microscopic evaluation of the topography of their fracture surfaces. For that purpose, representative regions of the microscopically nonuniform surfaces were identified and photographically documented. The aim of the investigation centered on the determination of characteristics in the fracture surfaces of carbonfiber-reinforced laminates caused by a) preceding thermal cycling of test specimens, b) variations of the curing process, c) different moisture contents and d) different test temperatures. The test specimens were uni- and multidirectional laminates which were loaded statically to failure. In each of the last three test series, two of the parameters mentioned above were held constant while the third was systematically varied.

13.4.1 Influence of Thermal Cycling

In the course of the thermal cycling tests described in Section 10, $[\pm 45]_{28}$ -specimens made from different materials were exposed to ca. 3500 thermal cycles between +90°C and -155°C. The evaluation of their properties prior to and after cycling included a comparison of relevant features of their fracture surfaces after static loading to failure. Pertinent microphotographs of Fiberdux 914C/T300 specimens are assembled in Fig. 13.20 through 13.31. The even-numbered figures always relate to non-cycled specimens and the odd-numbered figures, to cycled specimens.

Figs. 13.20 and 13.21 show the rupture planes of a 45°-ply and part of the adjacent ply beneath it. In the non-cycled specimen many specks of the resin are still attached to the fibers over the entire extent of the microphotograph, whereas the rupture plane of the cycled specimen is much smoother. At higher magnification (Figs. 13.22 and 13.24) the resin particles are seen to still firmly adhere to the fibers. In Figs. 13.23 and 13.25 the surfaces of the fibers and their impressions in the matrix material appear quite smooth. The matrix has a rather flat topography and is more finely grained, which is indicative of embrittlement. This observation is supported by Figs. 13.26 and 13.27 which show a higher number of fiber breaks and a stronger inclination of the fiber failure plane at the cycled specimen. Corresponding macro-mechanical tests described in Section 10 support the soundness of this contention.

It is also of significance that the fracture surfaces of the cycled specimens have a rather flat topography and display crack patterns with smaller crack distances than those of the non-cycled specimens (Figs. 13.28 through 13.31) which may be interpreted as embrittlement of the resin due to the postcuring effect of the thermal cycling. A tendency toward embrittlement of the matrix and a weakening of the fiber-matrix interface was noted also in the other epoxy-systems referred to in Section 10. In the case of the polyimide-system, however, no degradation of the interface is evident from a comparison of the fracture surfaces of non-cycled and cycled specimens shown in Figs. 13.32 and 13.34, and in Figs. 13.33 and 13.35, respectively. An evaluation

of Figs. 13.36 and 13.37, on the other hand, points to a state of embrittlement in the polyimide-matrix on account of the high number of matrix cracks in the thermally cycled specimen.

13.4.2 Influence of Curing Cycle Variation

The study was motivated by the suspicion that modest changes of the curing cycle might influence the fracture surfaces of test specimens and camouflage the effect of those parameters whose identification is being attempted. In order to assess the significance of the issue, the tests commenced with $[\pm 45]_S$ -laminates laid up from Fiberdux 914C/T300 prepregs and cured with the following substantially different cycles:

- $H_1 = 1.5^\circ\text{C}/\text{min}$ to $170^\circ\text{C} + 4$ hrs at 170°C
- $H_2 = H_1 + 4$ hrs at 190°C
- $H_3 = H_2 + 4$ hrs at 240°C
- $H_4 = H_3 + 2$ hrs at 280°C

It should be noted that H_2 is the curing cycle recommended by the prepreg producer, and that the results of preliminary interlaminar shear tests conducted with specimens from all curing cycles were, in accordance with Fig. 13.38, indeed the highest for the H_2 -cycle.

The fracture surfaces of specimens tensile-loaded to failure indicated subtle distinctions. Figs. 13.39 through 13.42 show microphotographs typical of the four curing cycles at a magnification of 775. It is apparent that the H_2 -cycle produced the most uniform fracture pattern. At a magnification of 3 100 (Fig. 13.43 through 13.46) certain differences in the microstructure of the epoxy resin are recognizable which become more obvious at still higher magnification (Figs. 13.47 through 13.50). In comparison to the H_2 -cycle, the sphere-shaped elements of the microstructure in the H_1 -cycle are less pronounced, of larger diameter and of a nonuniform distribution, while in the H_3 - and H_4 -cycles the microstructure appears molten and indistinct. Apparently the optimal formation of a spherical microstructure correlates with an optimal strength of the epoxy matrix.

As a consequence of this investigation, the test specimens of the entire fracture mechanics program were cured under close observation of the prepreg supplier's recommendation (H_2 -cycle). Minor deviations from the prescribed temperature or pressure levels were not expected to cause noticeable effects on the microstructure of fracture surfaces.

13.4.3 Influence of Temperature and Moisture

The mechanical properties of carbonfiber-reinforced epoxy resins tend to degrade in wet, in wet and, especially, in hot-wet environments. In order to comprehend the nature of the degradation the fracture surfaces of uni- and multidirectional laminates were microscopically examined and evaluated.

The microphotographs in Figs. 13.51 through 13.58 display representative portions of the fracture surfaces of Fiberglass 914C T300 test specimens with a stacking order of $[0, \pm 45, 90]_g$. Two sets of test specimens were pre-conditioned to a completely dry state and to a moisture saturation state at 93% relative humidity, respectively, and then tension-loaded to failure at different temperatures. Figs. 13.51 through 13.53 depict the fracture characterization of the 90° -ply at the center of a dry specimen. It is quite evident that at -55°C the matrix material has a finely grained topography indicating low ductility whereas, beginning already at 25°C and clearly so at 120°C , the matrix fails with a coarser pattern and adheres less well to the fibers. This effect is more pronounced in the moisture-saturated specimen (Figs. 13.54 and 13.55) where, at 120°C , hardly any of the matrix material adheres to the fibers, signifying a predominantly adhesive failure. Rather similar observations can be made in Figs. 13.56 through 13.61 depicting corresponding appearances in a $\pm 45^\circ$ -ply.

Figs. 13.62 through 13.66 show microphotographs of a dry 914C T300 unidirectional $[90]_g$ -laminate loaded transverse to the fiber direction. Relatively good adhesion seems to prevail at all temperatures for which both the coarse surfaces of the fibers and the presence of sheared fibers are indicative. In contrast, the moist specimens at 120°C display no fiber breaks at all on account of the markedly reduced fiber-to-matrix adhesion (Fig. 13.67). Test specimens of identical configuration but prepared from Code

69/T300 material exhibited phenomenologically similar trends. However, from the texture of the fracture surfaces as well as from the number and the inclination of the fiber breaks it may be deduced that the adhesive properties of this fiber-matrix system are somewhat superior to the Fiberdux 914C/T300 system (Figs. 13.68 through 13.73).

13.5 Investigation of Dynamically Loaded Laminates

The fracture surfaces of a large number of Fiberdux 914C/T300 laminates with stacking orders of $[\pm 15]_8$, $[\pm 30]_8$, $[\pm 45]_8$ and $[0, \pm 45, 90]_8$ were microscopically investigated after cyclic loading at different stress levels and different numbers of cycles. All test specimens were dry and were tested at two different temperatures.

Macroscopically the fracture surfaces were always of a very rough appearance. The microscopic interpretation depended much on the location of the investigated segment within the normally splintered fracture surface but led to no consistent diagnosis. Equally unsuccessful was the attempt to discover the anticipated growth bands in the matrix material.

Despite the rather comprehensive test program a systematic classification of the effects of temperature, number of cycles and stress level could not yet be accomplished. The major problem is the unknown interplay of chronological and geometric occurrences at the point of damage growth which cannot be separated by post mortem analyses.

A certain trend was observed in the case of the angle-ply laminates where at the free edges a weakening of the fiber-matrix adhesion, and at the center of the specimen a grinding of the matrix material seems to take place, but this point is made with considerable reservation.

13.6 Characteristic Values in Micromechanics

It would, of course, be desirable to identify the micromechanical failure phenomena in terms of characteristic values and to correlate those with macromechanical data. In view of the complexity

and the stochastic nature of the problem this will only be possible in selected cases. For the characterization of the fiber-matrix adhesion, for example, the mean length of the pulled-out fibers may serve that purpose. First attempts in this direction were made with Fiberdux 914C/T300 laminates with a stacking order of $[0,90]_S$. 1.25 mm wide segments of the fracture surface of a 0° -ply were magnified and photographed for a subsequent measure of the fiberends protruding from the matrix. The mean value of a large number of measurements of pulled-out fibers was then displayed graphically as a function of test temperature and moisture content of the test specimens. Fig. 13.74 indicates a distinct dependence of the mean length of the pulled-out fibers on both parameters. A comparison with the macroscopic strength properties given in Fig. 13.75 shows a remarkably good correlation considering that diminishing strength implies increasing fiber pull-out lengths.

13.7 References

- [13.1] Engel, L. Rasterelektronenmikroskopische
 Klingele, H. Untersuchung von Kunststoffschäden.
 Ehrenstein, G. Carl Hanser Verlag, München, 1978.
 Schaper, H.

- [13.2] Franz, H.E. Ermüdungsbruchstrukturen an
 faserverstärkten Kunststoffen.
 MBB-Bericht BB-300-78.



Fig. 13.1

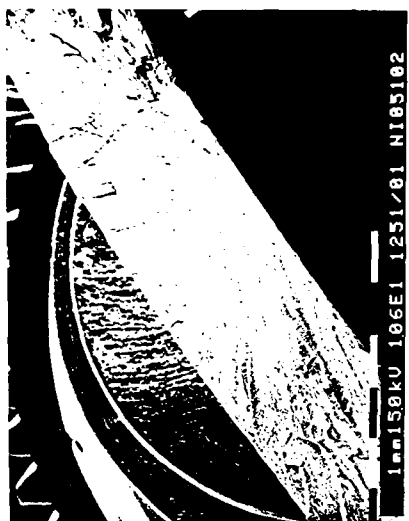


Fig. 13.2

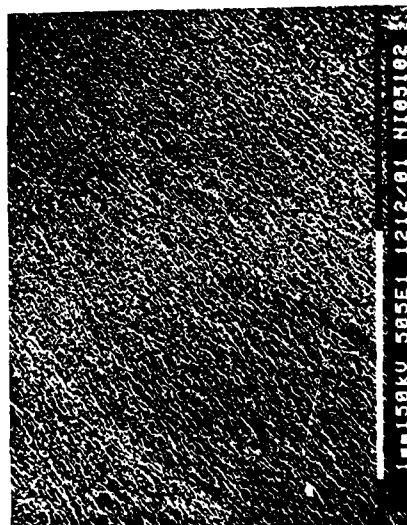


Fig. 13.3

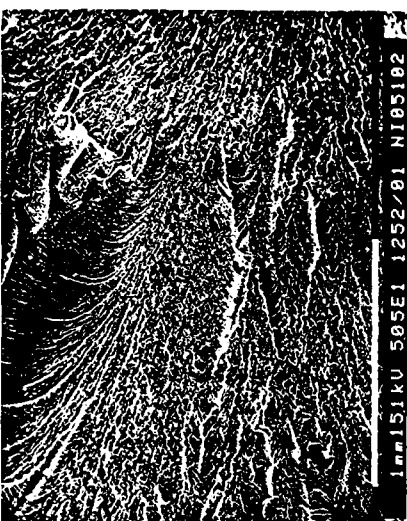


Fig. 13.4

Epoxy resin BSL 914; fracture surfaces of tensile test specimens.

Left: Dry

Tensile strength: 37,6 N/mm²

Fracture strain : 1,35%

Right: Moisture content: 9% (saturated at 93% r.H.)

Tensile strength: 55,7 N/mm²

Fracture strain : 2,7%



Fig. 13.5

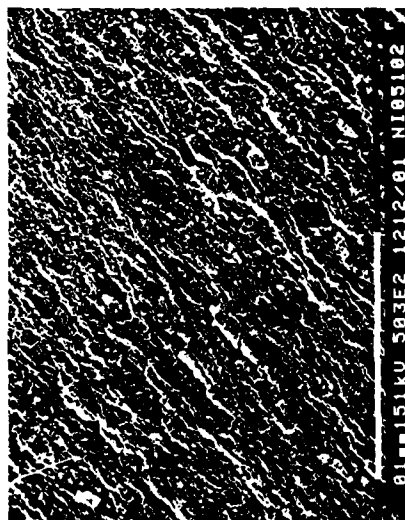


Fig. 13.6

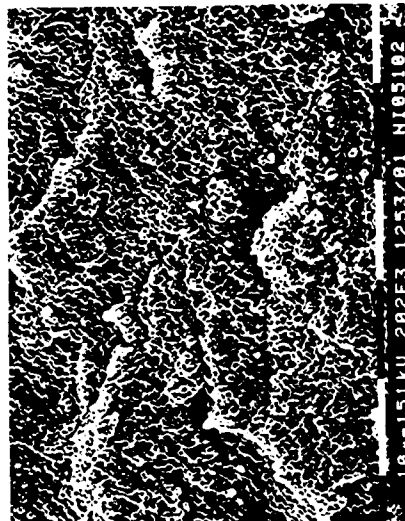


Fig. 13.7

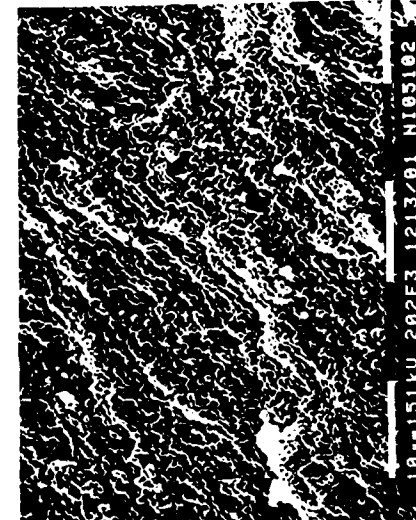


Fig. 13.8

Left: Dry
 Tensile strength: 37,6 N/mm²
 Fracture strain : 1,35%

Right: Moisture content: 9% (saturated at 93% r.H.)
 Tensile strength: 55,7 N/mm²
 Fracture strain : 2,7%

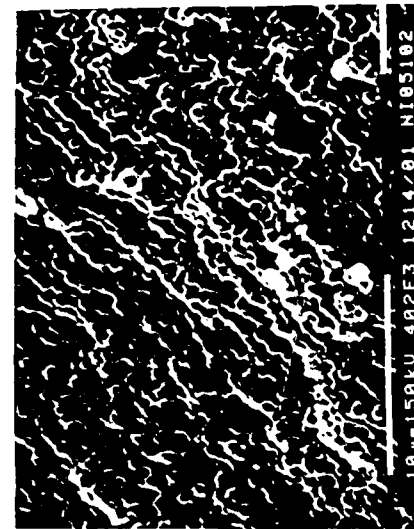


Fig. 13.9

Epoxy resin BSL 914; fracture surfaces of

Left: Dry

Tensile strength: 37,6 N/mm²

Fracture strain : 1,35%

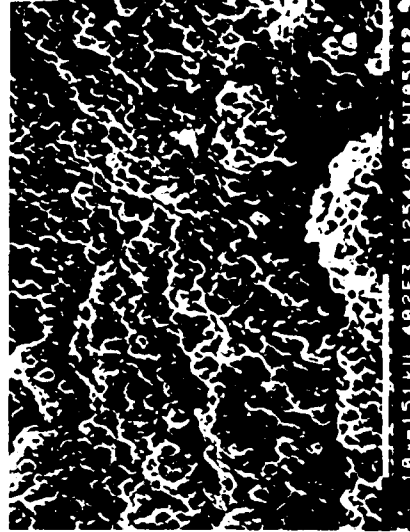


Fig. 13.10

Right: Moisture content: 9% (saturated at 93% r.H.)

Tensile strength: 55,7 N/mm²

Fracture strain : 2,7%



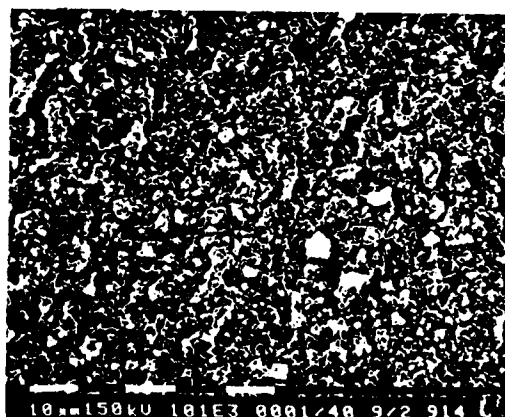
Heating rate 4°C/min
up to 170°C
4h constant 170°C

Fig. 13.11



Heating rate 0,8°C/min
up to 170°C
4h constant 170°C

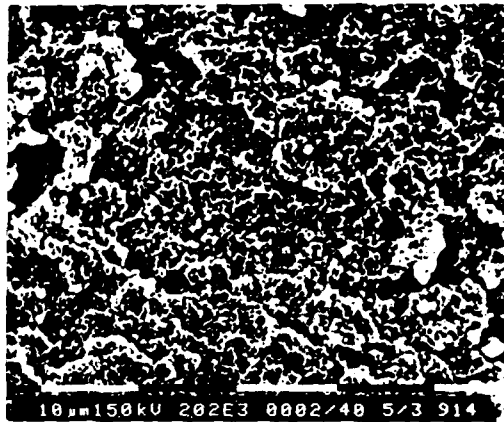
Fig. 13.12



Heating rate 2°C/min
up to 120°C
3h constant 120°C,
2°C/min up to 170°C
4h constant 170°C

Fig. 13.13

Epoxy resin BSL 914. Fracture surfaces of tensile test specimens with different curing cycles.



Heating rate 4°C/min
up to 170°C
4h constant 170°C

Fig. 13.14



Heating rate 0,8°C/min
up to 170°C
4h constant 170°C

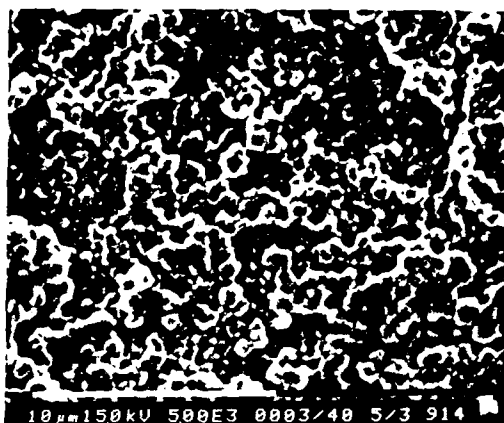
Fig. 13.15



Heating rate 2°C/min
up to 120°C
3h constant 120°C,
2°C/min up to 170°C
4h constant 170°C

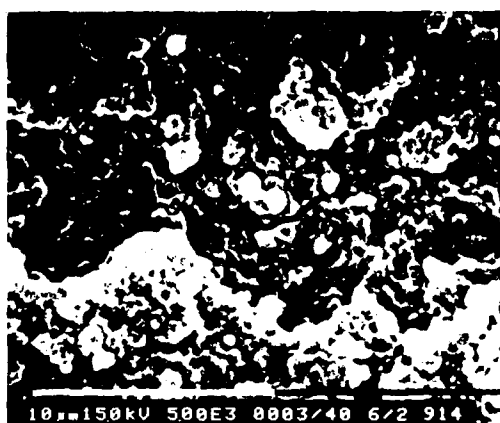
Fig. 13.16

Epoxy resin BSL 914. Fracture surfaces of tensile test specimens with different curing cycles.



Heating rate 4°C/min
up to 170°C
4h constant 170°C

Fig. 13.17



Heating rate 0,8°C/min
up to 170°C
4h constant 170°C

Fig. 13.18



Heating rate 2°C/min
up to 120°C
3h constant 120°C,
2°C/min up to 170°C
4h constant 170°C

Fig. 13.19

Epoxy resin BSL 914. Fracture surfaces of tensile test specimens with different curing cycles.



Fig. 13.20



Fig. 13.22

914C-TS-5 laminates, $[\pm 45^\circ]_{2s}$
 Left: Without thermal cycling;

$$\dot{G}_{ult.} = 143,1 \text{ N/mm}^2$$

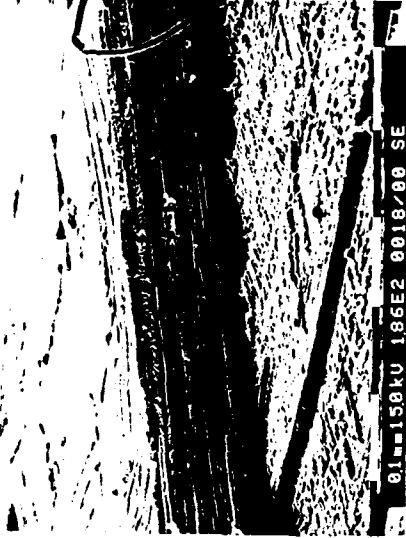


Fig. 13.21



Fig. 13.23

Right: 3480 thermal cycles;

$$\dot{G}_{ult.} = 151,9 \text{ N/mm}^2.$$

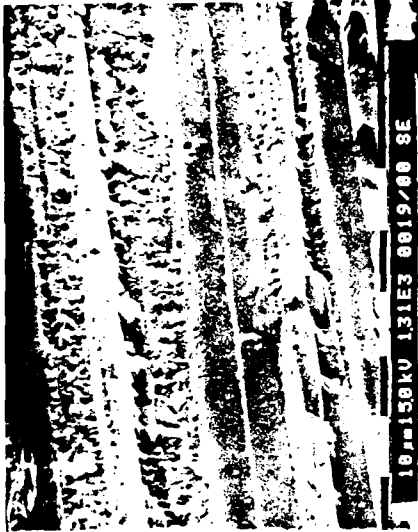


Fig. 13.25



Fig. 13.27



Fig. 13.24



Fig. 13.26

914C-TS-5 laminates, $[\pm 45^\circ]_{2s}$. Fracture surfaces of tensile test specimens.

Left: Without thermal cycling;

Right: 3480 thermal cycles;

$$G_{ult.} = 143,1 \text{ N/mm}^2$$

$$G_{ult.} = 151,9 \text{ N/mm}^2.$$



Fig. 13.28



Fig. 13.29



Fig. 13.30



Fig. 13.31

914C-TS-5 laminates, $[\pm 45^\circ]_{2s}$. Fracture surfaces of tensile test specimens.
 Left: Without thermal cycling;
 $G_{ult.} = 143,1 \text{ N/mm}^2$
 Right: 3480 thermal cycles;
 $G_{ult.} = 151,9 \text{ N/mm}^2$.



Fig. 13.32



Fig. 13.34

Polyimide laminates T3T-F178, $[\pm 45^\circ]_{2s}$

Left: Without thermal cycling,

$$G_{ult.} = 121,5 \text{ N/mm}^2.$$



Fig. 13.33



Fig. 13.35

Right: 1170 thermal cycles,

$$G_{ult.} = 69 \text{ N/mm}^2.$$



Fig. 13.36

Polyimide laminates T3T-F178, $[\pm 45^\circ]$ _{2s}.
Left: Without thermal cycling,

$$\sigma_{ult.} = 121,5 \text{ N/mm}^2.$$



Fig. 13.37

Right: 1170 thermal cycles,

$$\sigma_{ult.} = 69 \text{ N/mm}^2.$$

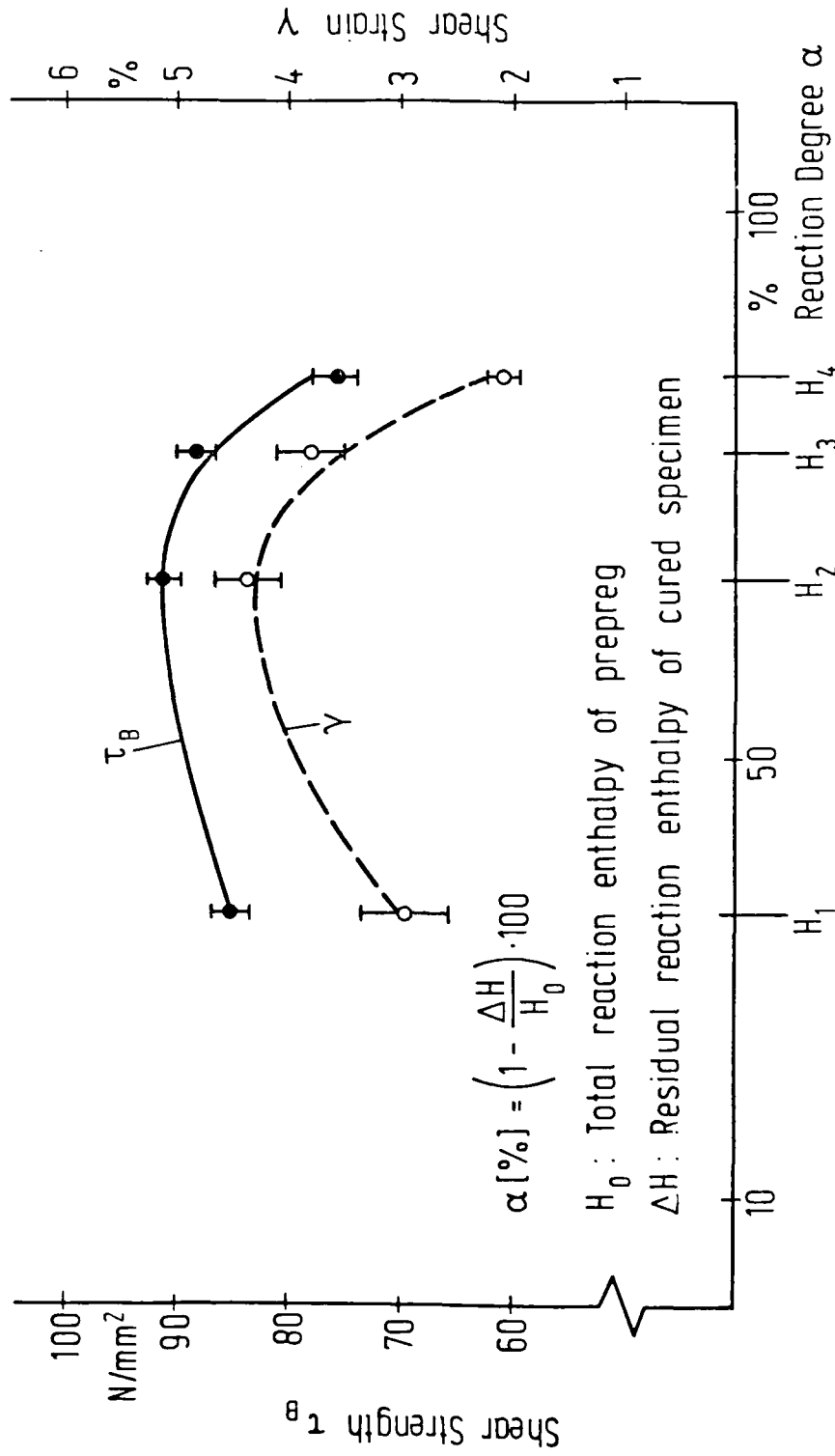


Fig. 13.38 Strength and shear strain of 914C/T300 laminates $[\pm 45^\circ]_S$ as a function of reaction degree α for different curing cycles.



H₁ =
1,5°C/min to
170°C;
170°C/4h

Fig. 13.39



H₃ =
H₂+240°C/4h

Fig. 13.41



H₂ =
H₁+190°C/4h

Fig. 13.40



H₄ =
H₃+280°C/2h

Fig. 13.42

13-23

914C/T300 laminates [$\pm 45^\circ$]_s, with different curing cycles H₁ to H₄ (tensile test)



$H_1 =$
 $1,5^\circ\text{C}/\text{min}$ to
 $170^\circ\text{C};$
 $170^\circ\text{C}/4\text{h}$

Fig. 13.43



$H_2 =$
 $H_2 + 240^\circ\text{C}/4\text{h}$

Fig. 13.45



$H_2 =$
 $H_1 + 190^\circ\text{C}/4\text{h}$

Fig. 13.44



13-24

$H_4 =$
 $H_3 + 280^\circ\text{C}/2\text{h}$

Fig. 13.46

914C/T300 laminates $[\pm 45^\circ]_s$, with different curing cycles H_1 to H_4 (tensile test)



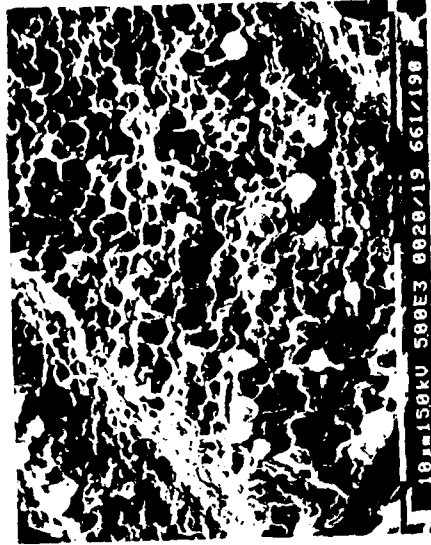
$H_1 =$
 1,5°C/min to
 170°C;
 170°C/4h

Fig. 13.47



$H_3 =$
 $H_2 + 240^\circ\text{C}/4\text{h}$

Fig. 13.49



$H_2 =$
 $H_1 + 190^\circ\text{C}/4\text{h}$

Fig. 13.48



$H_4 =$
 $H_3 + 280^\circ\text{C}/2\text{h}$

Fig. 13.50

13-25

914C/T300 laminates $[\pm 45^\circ]_s$, with different curing cycles H_1 to H_4 (tensile test)



$T = -55^{\circ}\text{C}$

Fig. 13.51



$T = 23^{\circ}\text{C}$

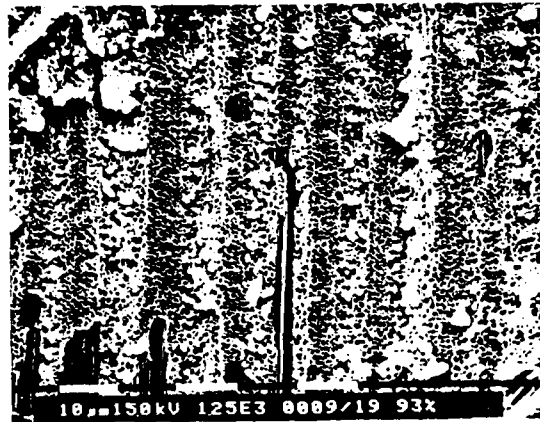
Fig. 13.52



$T = 120^{\circ}\text{C}$

Fig. 13.53

Fracture surfaces of 914C/T300 laminates $[0^{\circ}, \pm 45^{\circ}, \overline{90^{\circ}}]_s$.
Tensile loading parallel to 0° -layer. View onto the
 90° -layer. Completely dry specimens, tested at different
temperatures.



$T = -55^{\circ}\text{C}$

Fig. 13.54



$T = 120^{\circ}\text{C}$

Fig. 13.55

Fracture surfaces of 914C/T300 laminates $[0^{\circ}, \pm 45^{\circ}, \overline{90^{\circ}}]_s$.
Tensile loading parallel to 0° -layer. View onto the
 90° -layer. Moisture saturated specimens (at 93% r.H.),
tested at different temperatures.



$T = -55^{\circ}\text{C}$

Fig. 13.56



$T = 23^{\circ}\text{C}$

Fig. 13.57



$T = 120^{\circ}\text{C}$

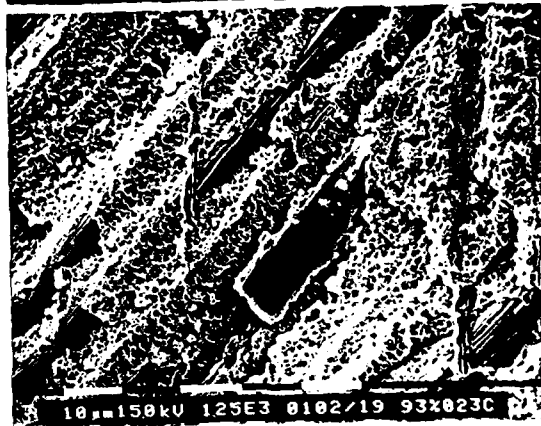
Fig. 13.58

Fracture surfaces of 914C/T300 laminates $[0^{\circ}, \pm 45^{\circ}, \overline{90^{\circ}}]_s$. Tensile loading parallel to 0° -layer. View onto the $+45^{\circ}$ -layer. Completely dry specimens tested at different temperatures.



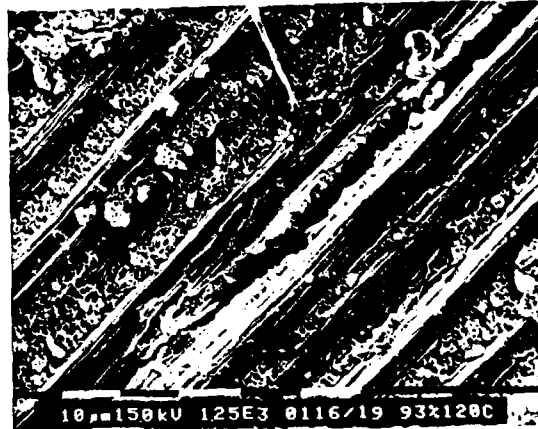
$T = -55^{\circ}\text{C}$

Fig. 13.59



$T = 23^{\circ}\text{C}$

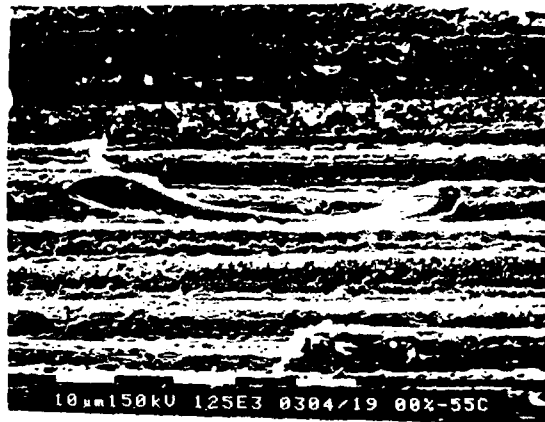
Fig. 13.60



$T = 120^{\circ}\text{C}$

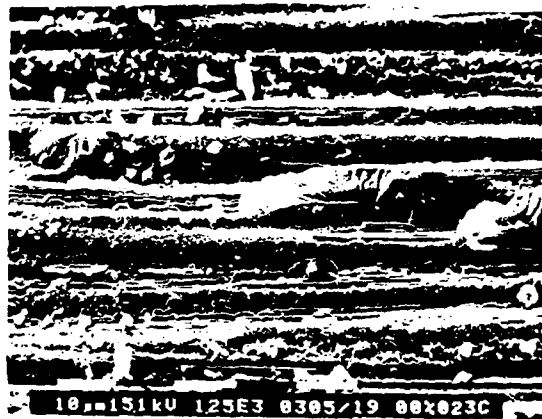
Fig. 13.61

Fracture surfaces of 914C/T300 laminates $[0^{\circ}, \pm 45^{\circ}, \overline{90^{\circ}}]_s$.
Tensile loading parallel to 0° -layer. View onto the $+45^{\circ}$ -layer.
Moisture saturated specimens (at 93% r.H.) tested at different
temperatures.



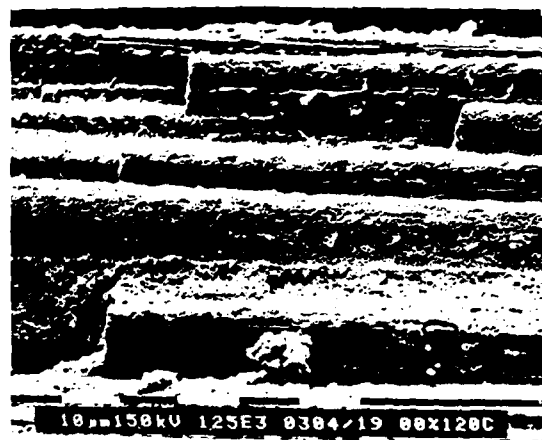
$T = -55^{\circ}\text{C}$

Fig. 13.62



$T = 23^{\circ}\text{C}$

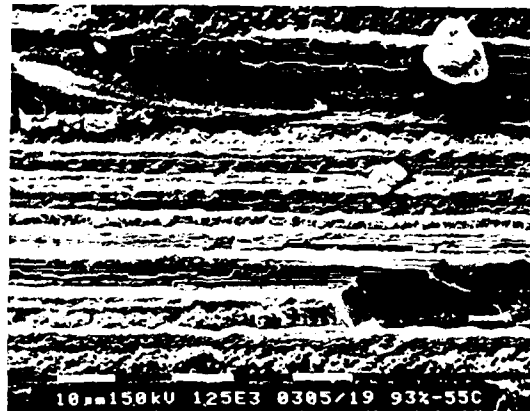
Fig. 13.63



$T = 120^{\circ}\text{C}$

Fig. 13.64

Fracture surfaces of unidirectional 914C/T300 laminates. Tensile loading transverse to fiber direction. Completely dry specimens tested at different temperatures.



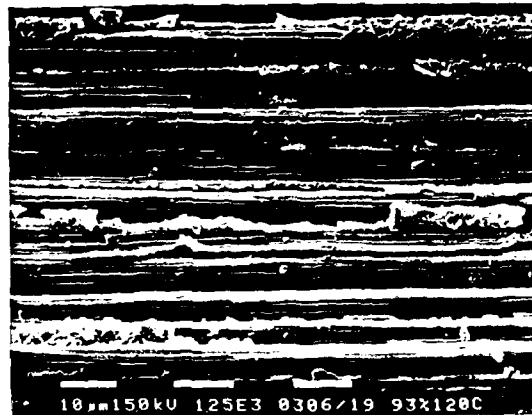
$T = -55^{\circ}\text{C}$

Fig. 13.65



$T = 23^{\circ}\text{C}$

Fig. 13.66



$T = 120^{\circ}\text{C}$

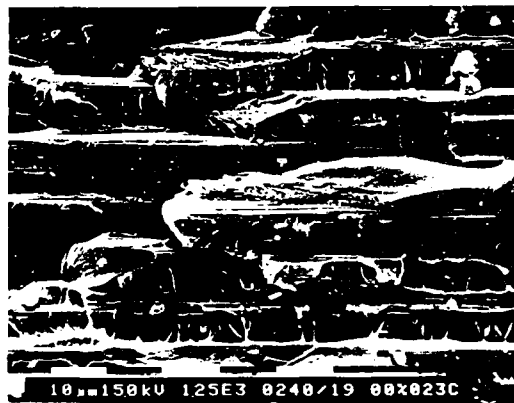
Fig. 13.67

Fracture surfaces of unidirectional 914C/T300 laminates
Tensile loading transverse to fiber direction. Moisture
saturated specimens (at 93% r.H.), tested at different
temperatures.



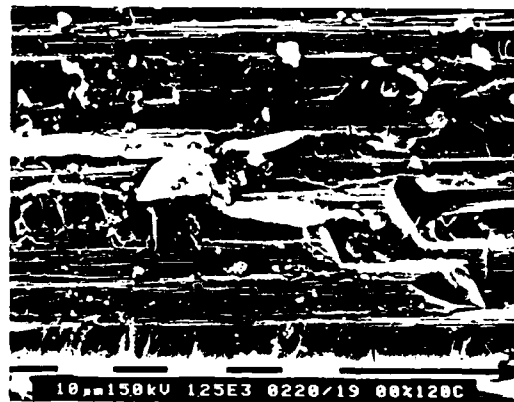
$T = -55^{\circ}\text{C}$

Fig. 13.68



$T = 23^{\circ}\text{C}$

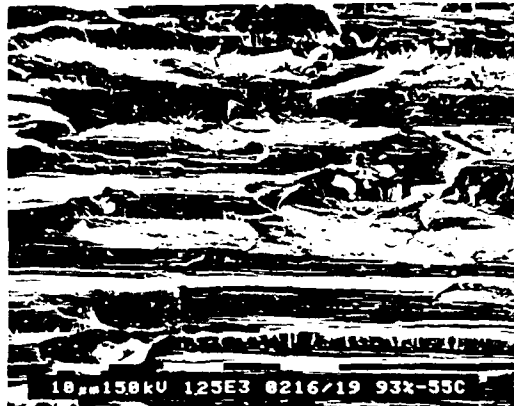
Fig. 13.69



$T = 120^{\circ}\text{C}$

Fig. 13.70

Fracture surfaces of unidirectional Code 6/T300 laminates. Tensile loading transverse to fiber direction. Completely dry specimens tested at different temperatures.



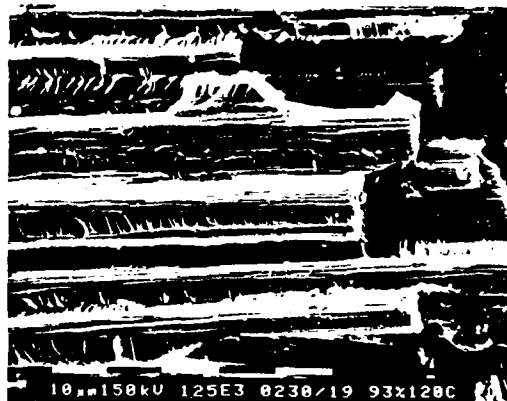
$T = -55^{\circ}\text{C}$

Fig. 13.71



$T = 23^{\circ}\text{C}$

Fig. 13.72



$T = 120^{\circ}\text{C}$

Fig. 13.73

Fracture surface of unidirectional Code 9/T300 laminates. Tensile loading transverse to fiber direction. Moisture saturated specimens (at 93% r.H.), tested at different temperatures.

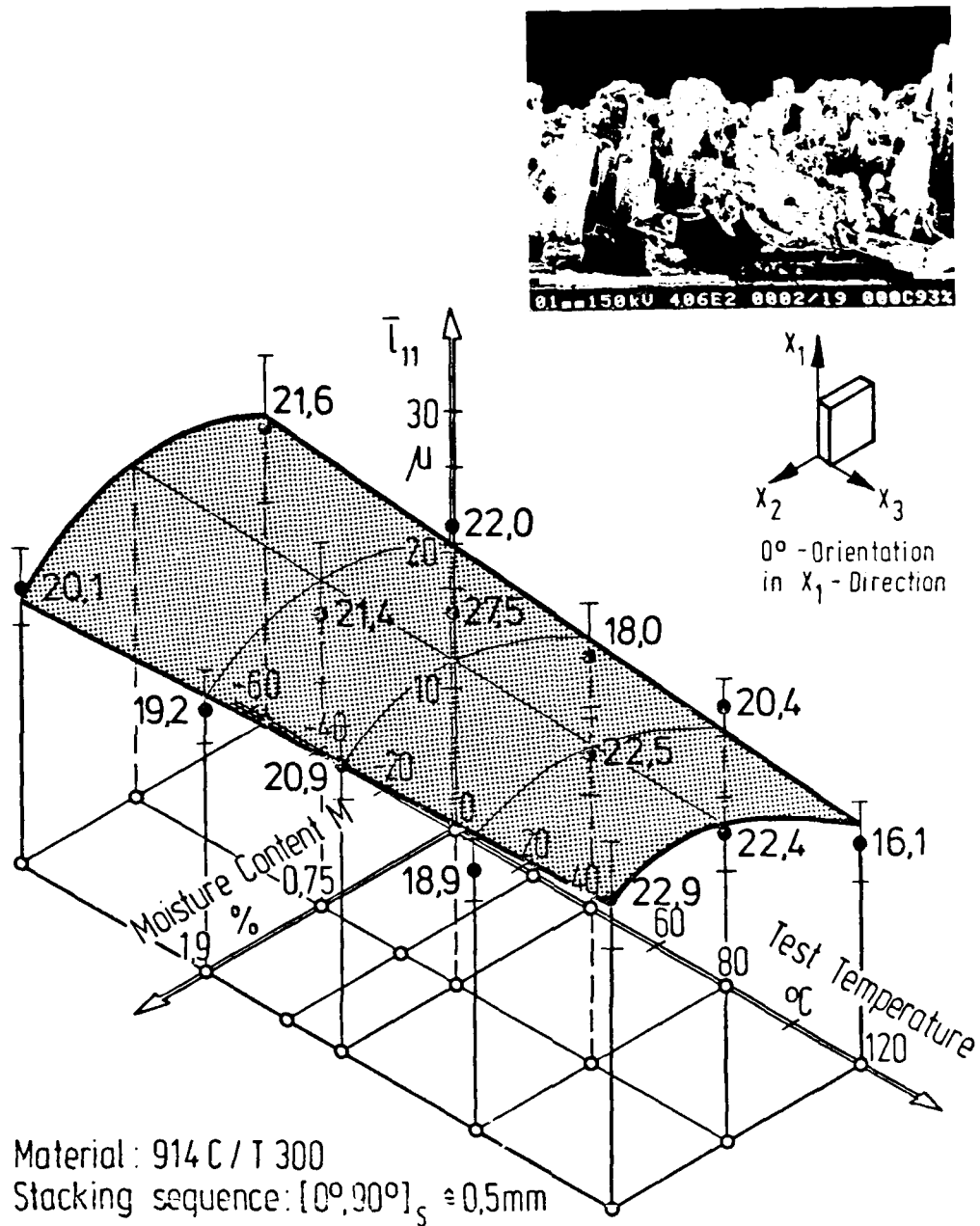
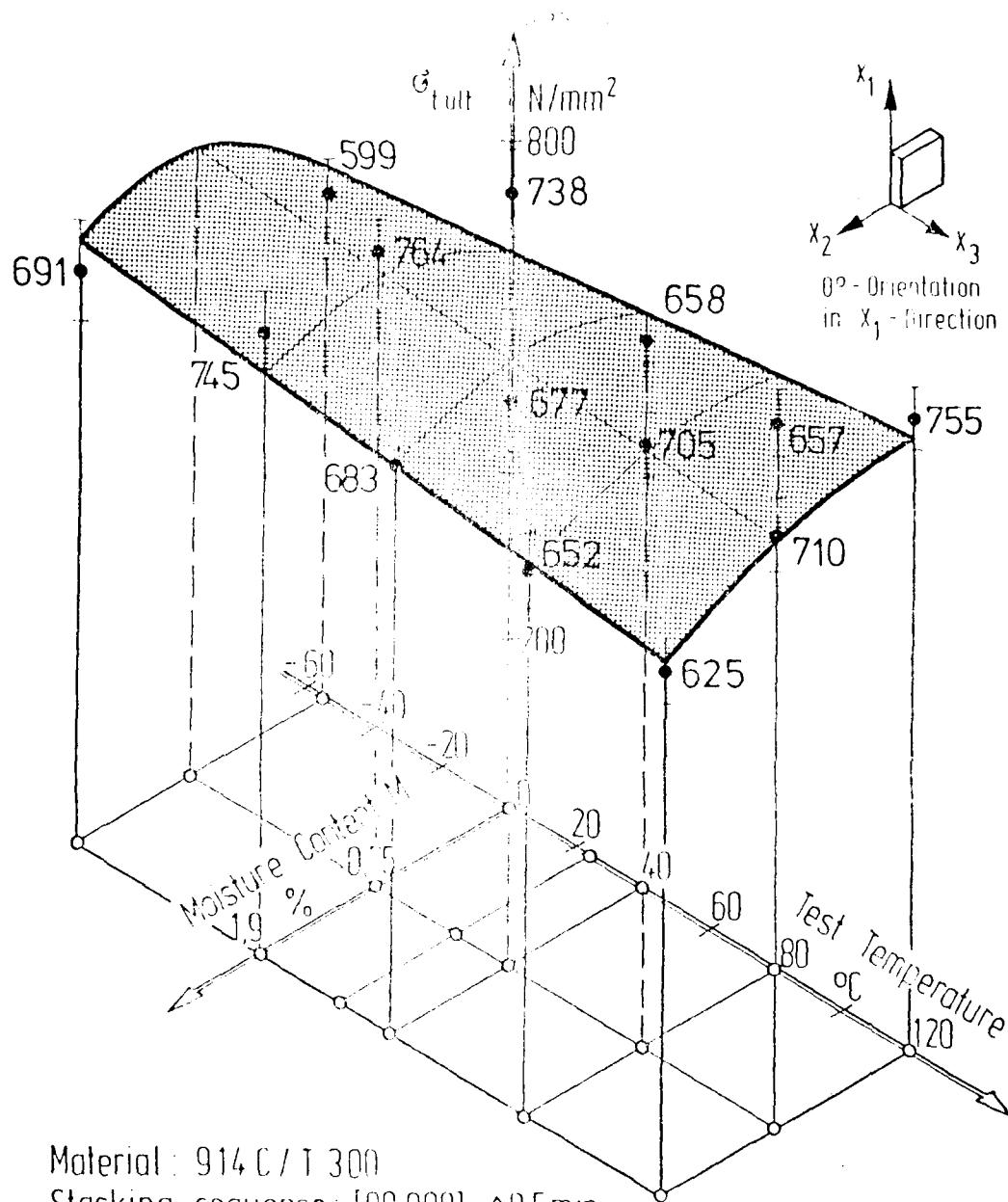


Fig. 13.74 Mean length of fiber pull-out \bar{l}_{11} of 914C/T300-laminates $[0^\circ, 90^\circ]_s$ as a function of test temperature and material moisture content.



Material : 914 C / T 300
Stacking sequence : $[0^{\circ}, 90^{\circ}]_5 \pm 0.5mm$

Average of 6 measurements
with standard deviations

Fig. 13.75 Ultimate tensile strength of multidirectional CFRP-laminates as a function of test temperature and material moisture content.

14. FRACTURE MECHANICS ASPECTS

14.1 Summary

The principles of linear fracture mechanics were originally developed to describe the initiation and progression of cracks in isotropic and homogeneous materials. These principles cannot be applied directly to fiber-reinforced laminate because here, instead of a single crack, a damaged zone develops in which the laminate progressively deteriorates. Fissuring and meandering cracks extending through the thickness of the material form only shortly before ultimate failure, i.e., after the useful life of the laminate. From this premise arises the need for the development of a new discipline - damage mechanics - capable of describing the behavior of damaged zones in fiber-reinforced structures prior to ultimate failure. Generally accepted concepts of damage mechanics are still rare. Known to some extent are individual mechanisms of damage progression but their contributions, single or in combination, to the total state of damage are not well understood. Current research efforts, therefore, are directed toward the definition of characteristic strength parameters for carbon-fiber-reinforced resins by a combination of analysis and test.

14.2 Limits of Fracture Mechanics

From the microstructural point of view, metals consist of assemblies of crystals. Their deformation and fracture characteristics are essentially dependent on the properties of the individual crystals and on their lattice structures, whose normally regular configurations may be disturbed by inclusions and grain boundaries. Under increasing loads the resulting stress concentrations lead first to dislocations and, subsequently, to microcracks oriented perpendicular to the maximum principal stresses. As the number of microcracks increases they tend to merge and may form an arbitrarily oriented macrocrack. The mathematical treatment of the crack progression is relatively simple because the minute dimensions of the metallic microstructures

justify the assumptions of homogeneity and isotropy. On that basis the principles of linear fracture mechanics have been developed.

In contrast to metals, fiber-reinforced resins behave quite differently. In unidirectional on-axis laminates the microcracks in the resin lead to matrix cracks which, because of the low transverse strength of the laminate, are always oriented in the direction of the fibers. Rupture of individual fibers takes place in increasing numbers only shortly before laminate failure and is not considered here. The fiber dimensions are small relative to the laminate thickness, warranting the assumptions of distributed homogeneity and of orthotropy and, on that basis the applicability of linear fracture mechanics with correspondingly high mathematical and numerical effort.

In multidirectional laminates such a simplified approach is not feasible since the development of damage depends not only on the material properties and the stress level but also on the stacking order of the laminate. The propagation of cracks initiating in one of the plies is impeded by adjacent plies with different fiber orientations, resulting in a pattern of many small cracks instead of a massive single crack. The superposition of the crack patterns in all of the plies leads to the concept of a damaged zone which grows with increasing load intensity as depicted by the radiographic records in Fig. 12.1. At high load levels neighboring plies disconnect locally and form delaminations.

Whether the precepts of classical fracture mechanics can be modified or expanded to adequately predict the response of notched multidirectional laminates is a point of continued debate. The simplistic approach of modelling multidirectional laminates as homogeneous orthotropic materials, for instance, defaults because of three major difficulties.

The first is the concept of stress singularities underlying conventional fracture mechanics. Whereas metals may be considered as homogeneous down to dimensions of order 10^{-5} cm, fiber-reinforced resins are homogeneous only down to dimensions of order 10^{-2} cm. Consequently, a continuum analysis which treats multidirectional

laminates as homogeneous and anisotropic materials begins to lose relevance for any characteristic dimension approaching 10^{-2} cm. In other words, it is meaningless to use elasticity solutions to model fracture phenomena located within 10^{-2} cm of the crack tip. Since the local stresses around a crack tip are proportional to $\sqrt{a/r}$ (a , r being the crack length and the distance from the crack tip, respectively), a 1 cm long crack in metals leads to stress intensity factor of over 300 at $r=10^{-5}$ cm, whereas in composites with the same crack length the highest meaningful calculable stress intensity factor is only 10 at $r=10^{-2}$ cm. The former may be considered as infinite for practical purposes, but the latter is not higher than frequently encountered in structural applications.

The second difficulty is the modelling of the size effect of the defect in a composite. Cracks of practical concern in metals are several orders of magnitude larger than the size of a typical heterogeneity, whereas in composites they may be of the same magnitude as the heterogeneity. This leads to the need of treating size effects differently than in standard continuum mechanics predictions.

The third and the most severe difficulty is the inability of classical fracture mechanics to model fracture processes which have more than a single degree of freedom, as in biaxial loading. Candidate models which address this specific aspect, such as the strain energy density function or the critical volume for stress and strength vectors, have not yet been convincingly validated.

14.3 Concepts of Damage Mechanics

For the comprehensive treatment of failure modes and fracture processes in fiber-reinforced laminates the Institute for Structural Mechanics has introduced the term *damage mechanics*, whose concepts by intent and purpose are analogous to those of fracture mechanics of metals. In comparison, however, the issues of damage mechanics are considerably more complex partly because of the inhomogeneous and anisotropic nature of fiber-reinforced materials, and partly because of the large variety of potential failure

modes in the tension and also compression regime. On account of this complexity, a combined empirical-analytical approach to the establishment of valid accept reject repair criteria for industrial composite applications seemed most appropriate. On this premise, the Institute for Structural Mechanics has developed a damage mechanics program which is outlined in Figs. 14.1, 14.2 and 14.3.

Accordingly, much emphasis is placed on the detection and precise identification of potential damages by nondestructive evaluation of the laminates. The objective is not the generation of new techniques for industrial application but rather extreme accuracy for the monitoring of the rate of progression of different kinds of damages in thin laminates.

The major portion of the research work is concerned with the effects of such damages on the load-carrying capabilities of test specimens subjected to increasing static loads or numbers of load cycles. The test specimens are flat laminates made of T300/914C, T300/Code 69 and T300/F550 material with stacking orders typical of aircraft skin covers, chords and webs. A large portion of the test specimens contain artificially introduced damages such as delaminations, notches and cracks. The test program encompasses the application of static and fatigue loads under realistic environmental conditions. The large number of test results allows a comparison of initial and residual material properties, the determination of tolerance levels below which various kinds of damages can be safely ignored, and the rate of progression of damages exceeding the tolerance levels.

In parallel with the empirical investigations, the development of analytical tools is pursued in order to gain insight into the mechanisms of damage progression. The short-term objective of these efforts is the assessment of the three dimensional stress field in the vicinity of discontinuities in multidirectional laminates which currently defy determination both analytically and empirically. Emphasis is placed on the solution of matrix cracks in the 90°-plies of a multidirectional laminate and on delaminations between adjacent plies. These special cases can be addressed on the basis of linear fracture mechanics using nonlin-

ear geometric and constitutive relationships. In a subsequent step it must be decided how the knowledge thus gained can be incorporated into a more general treatment of damage progression. It is envisioned to conduct the related numerical calculations with the specially developed computer program LAMINA described in Section 5.

The long-term objective, of course, is the establishment of hypotheses of damage accumulation from which conclusions can be drawn for the remaining service life of damaged laminates. Since the combined empirical and analytical investigations will only lead to an understanding of flat laminates under uniaxial loading conditions, necessary sequels for the desired formulation of quantitative accept/reject/repair criteria would be an extension of these investigations to biaxial loading conditions and a verification of the conclusions on actual structural components.

14.4 References

- [1] Libowitz, H. Fracture, an advanced treatise.
London, Academic Press, 1968, Vol. 1 - 6.
- [2] Sih, G.C. On cracks in rectilinearly anisotropic
Povis, P.C. bodies.
Irwin, G.R. Int. J. Fracture Mech., 1 (1965),
pp. 189 - 203. pp.189-203.
- [3] Huth, H. Anwendung der Bruchmechanik bei Faserver-
bundwerkstoffen.
LBF-Bericht Nr. 3396 (1978).
- [4] Dharan, C.K.H. Fracture mechanics of composite materials.
J. Eng. Material and Technique,
100 (1978), p. 233.
- [4] Kanninen, M.F. A critical look at current applications of
Rybicki, E.F. fracture mechanics to failure of fiber-
Brinson, H.F. reinforced composites.
Composites 8 (1977), pp. 17 - 22.
- [6] Kanninen, M.F. Preliminary development of a fundamental
Rybicki, E.F. analysis model for crack growth in a fiber-
Griffith, W.I. reinforced composite material.
Testing and Design (4. Conference),
ASTM STP 617 (1977), pp. 53-69.
- [7] Eggers, H. Beitrage zum Verhalten kohlefaserver-
staerkter Verbundstrukturen.
DFVLR-Mitteilung 83-13, S. 191 - 264.
- [8] Eggers, H. Schadensmechanik von faserverstaerkten
Verbundstrukturen.
DFVLR-Mitteilung 81-25, S. 167 - 196.

- [8] Eggers, H. Effektive Substrukturtechnik fuer finite
Elemente, Anwendung auf nichtlineare Probleme.
Vortrag auf dem Strukturmechanischen Kollo-
quium 1984 in Braunschweig. Erscheint als
DFVLR-Mitteilung.

- [9] Wang, A.S.D. Fracture mechanics of sublaminar cracks
in composite laminates.
AGARD-Structurals and Materials Specialists
Meeting, April 10 - 15, 1983, London, UK.

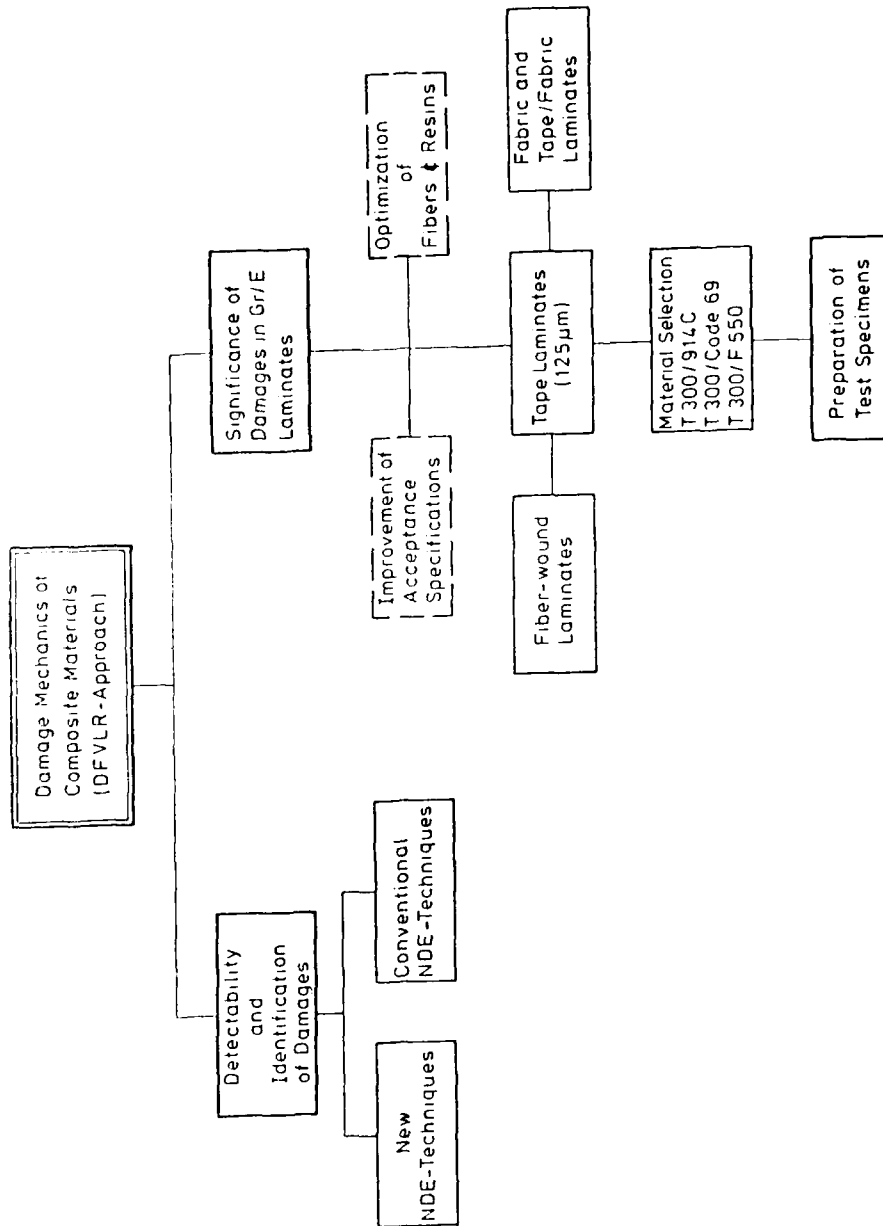


Fig. 14.1 DFVLR Damage Mechanics Program I

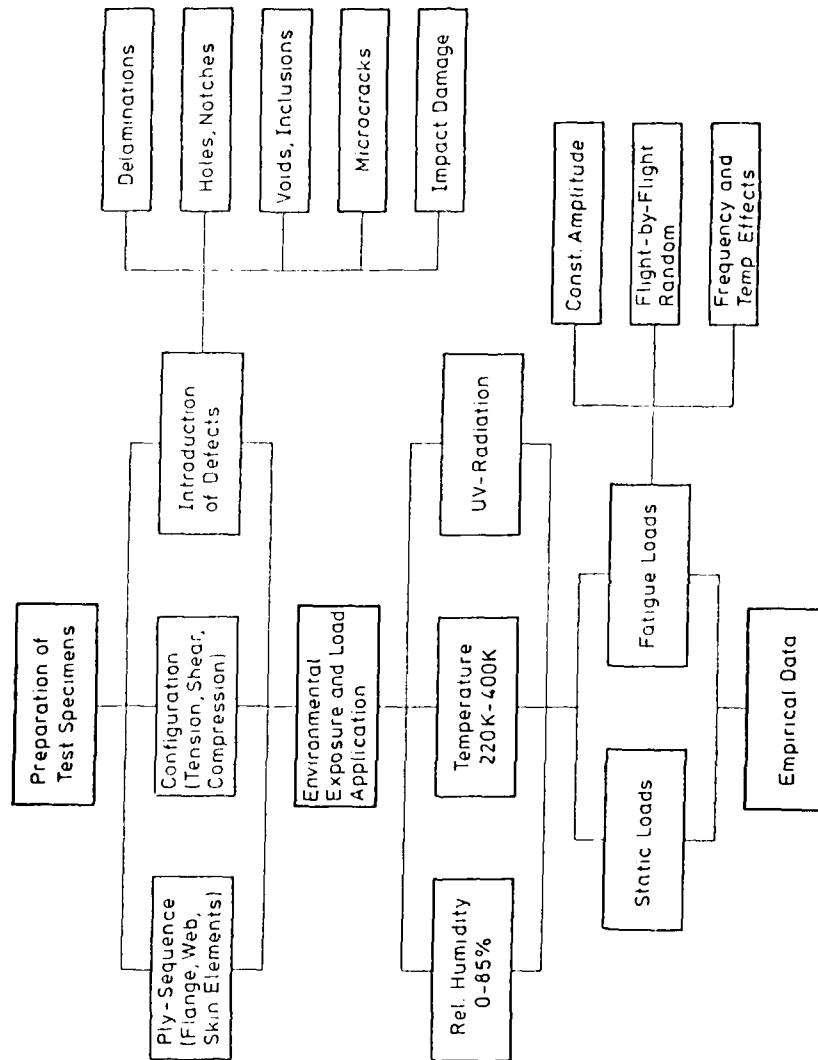


Fig. 14.2 DEVLAR Damage Mechanics Program II

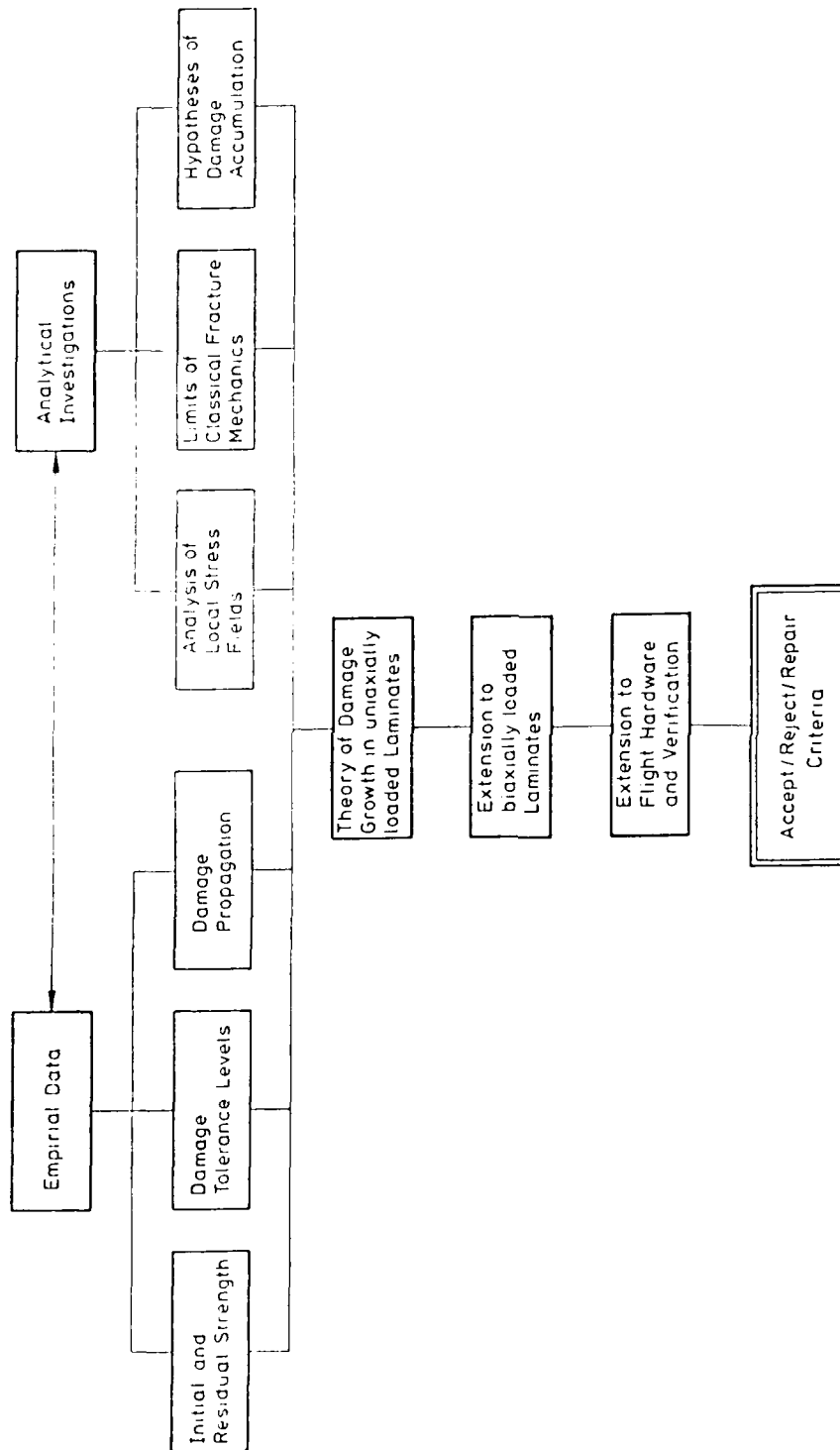


Fig. 14.3 DEVLAR Damage Mechanics Program III

15. EVALUATION OF FRACTURE MODELS

15.1 Summary

For the prediction of the fracture behavior of notched composite laminates, several simplified fracture models have been proposed in recent years. Most of these models extend linear elastic fracture mechanics from metals to composites and do not attempt to address the micromechanical complexities in the crack extension process. Rather, they assume a self-similar crack-extension, and the actual crack tip damage zone size is represented by an 'effective' damage zone size defined as a material parameter to be obtained experimentally. All of the fracture models assume these experimentally determined parameters to be material constants, whereas, in reality, they depend on, e.g. stacking order, constituent properties and fabrication technique as well as on type of loading, specimen geometry and environmental conditions. Consequently, the parameters established for a particular condition are not generally valid and are not transferrable from case to case.

A specific application of any of the investigated fracture models will require a series of independent tests whose number depends on the selected fracture model and on the level of desired accuracy. Since these tests are tailored to the problem under investigation they normally lead to good agreement between the predictions of a particular model and the actual strength of the notched laminates. Most of the models, therefore, are of considerable pragmatic importance even though they do not address the specific failure modes associated with fracture of a given laminate. In order to assess the range of applicability and the accuracy of the more commonly used fracture models, a comprehensive review was conducted [15.1] regarding the notch sensitivity of composite laminates containing centrally located holes and straight cracks, and being subjected to uniaxial loading. The objective of the review was a detailed evaluation of eleven different fracture models against a large amount of published test data. All of the collected experimental notched strength parameters were then compared with the predictions from each of the fracture models.

The subject is discussed in more detail in Appendix H "Notched Strength of Composite Laminates".

15.2 Discussion of Relevant Fracture Models

During the past decade a series of fracture models have been published in the open literature of which the following have been selected for a comprehensive review:

1. M.E. Waddoups, J.R. Eisenmann and B.E. Kaminski [15.2], abbreviated here as the WEK-fracture model. Two models were formulated:
 - a. for laminates containing circular holes, and
 - b. for laminates containing straight cracks.
2. J.M. Whitney and R.Y. Nuismer [15.3, 15.4], abbreviated as the WN-fracture model. Two failure criteria were formulated, i.e. "point-stress" and "average-stress" criteria. Both criteria were formulated for laminates containing holes and straight cracks.
3. R.F. Karlak [15.5], abbreviated as the K-fracture model, modified the WN-"point-stress" criterion for laminates containing circular holes.
4. R.B. Pipes, R.C. Wetherhold, and J.W. Gillespie, Jr. [15.6, 15.7, 15.8], abbreviated as the PWC-fracture model, modified the WN "point-stress" criterion for laminates containing circular holes, and for laminates containing straight cracks.
5. J.W. Mar and K.Y. Lin [15.9], abbreviated as the ML-fracture model, applied to laminates containing both circular holes and straight cracks of various shapes.
6. C.C. Poe and J.A. Sova [15.10], abbreviated here as the PS-fracture model, applied to laminates containing straight cracks.

The application of these models for the prediction of the notched strength of composite laminates containing circular holes and straight cracks requires that certain parameters associated with each fracture model be known a priori. These parameters can be determined from preliminary experiments on notched laminates, and the number of tests that must be conducted depends upon the model itself and the level of accuracy required. Consequently, these models can be considered as semi-empirical fracture models, and it should be expected that they would all compare favorably with the actual experimental results. The only model that might be applied without preliminary testing is the FS-fracture model, and then only providing that the "general fracture toughness parameter" can in fact be considered sufficiently general as to be common to all material systems and laminate configurations.

Most of the models (WEK, WN, K and FWG fracture models) are based upon determination of a characteristic distance ahead of the notch tip at failure. The issue of whether or not this parameter is a material constant has been addressed in detail by each of these investigators and by numerous other experimental investigations as well. Exhaustive studies have been conducted in regard to this subject.

The first two models (WEK and WN) assumed that this parameter is a material constant, and Whitney and Nuismer even hypothesized that it might be independent of material system and/or laminate configuration. Many experimental investigations subsequently attempted to apply the values of the characteristic distances determined by Whitney and Nuismer for certain material systems to the experimental data of different material systems and laminate configurations, however with mixed results. The correlation between the fracture models and the experimental notched strength data reviewed in this report will demonstrate that the characteristic distances depend strongly on material system and laminate configuration and possibly on other parameters as well, such as loading procedures, environment, fabrication procedures, etc. However, for a given type of laminate, most of the experimental results indicate that these characteristic distances are independent of notch size.

Several investigators, however, have concluded that the characteristic distances cannot even be considered as material parameters, i.e. they also depend on notch size. Consequently, the WN-fracture models have been modified and an exponential relationship between the characteristic distances and the notch size has been proposed (K and PWG-fracture models). This assumption led to the introduction of two additional parameters, i.e. the notch sensitivity factor and an exponential parameter which are also to be determined empirically. It has been suggested that these are material parameters, however they also vary significantly for different material systems and laminate configurations. When the pertinent parameters are determined from preliminary testing, these proposed fracture models compare favorably with all experimental results. No attempt has yet been made to generalize these parameters for all types of materials. Instead, a relative notch sensitivity parameter has been introduced which depends directly on the notch sensitivity factor and the exponential parameter, and from which the relative notch sensitivity of any given laminate can be determined.

Finally, a fracture model which does not take into account such characteristic distance ahead of the notch tip has been proposed as well. This model (ML-fracture model) developed an exponential relationship between the notched strength and the size of the discontinuity. The exponential parameter in this model can be determined analytically, depending only on the constituent elastic properties; however, experimental results indicate that it may also depend on the laminate configuration and stacking sequence. Therefore, when this model is applied the exponential parameter is also determined experimentally from testing of notched laminates.

Clearly, all these models should agree with the experimental results, however, the dependence of the various parameters on the type of laminate is of interest. In this report, therefore, all these models are compared with a large volume of notched strength data and conclusions regarding the range of their applicability are discussed.

15.3 Survey of Experimental Data

In order to evaluate the applicability of the different semi-empirical fracture models for predicting the notched strength of composite laminates, the model predictions have to be compared to a large volume of experimental results. Therefore, a literature search has been conducted and published journal papers, conference proceedings, government reports, university internal reports and dissertations have been reviewed. As expected, there have been numerous experimental investigations during the last decade into the fracture behavior of composite laminates containing a variety of discontinuities. The great majority of the investigations dealt with the notched strength of composite laminates when subjected to quasi-static uniaxial tensile loading in ambient temperature and moisture conditions. Among these, the majority of the experiments were conducted on laminates containing either centrally located circular holes or center cracks with their axis perpendicular to the loading direction. Other types of discontinuities were also studied, such as double and single edge cracks, square holes (slots), circular holes with cracks emanating from one or both sides of the hole, straight cracks inclined to the loading directions, etc. Relatively limited data on fracture toughness of composite laminates obtained from the classical tests, such as three-point bend specimens or compact tension specimens, are reported in the literature. Notched strength data from other loading functions such as compression and post-fatigue, or under different environmental conditions of temperature and moisture are quite limited.

Many investigations were concerned with the applicability of the various fracture models and discussed their correlation with experimental results obtained on notched strength. However, in most cases, comparisons were made with selected models only, primarily the WER and WN-fracture models, or else several sets of experimental data were compared with a single fracture model. The objective of this study was to obtain a comprehensive set of experimental results and compare them with all the commonly used fracture models so that a more complete picture of the state of the arts in fracture mechanics of composite laminates could be obtained.

The current review centered on notched strength data for laminates containing circular holes and straight cracks located at the center of the specimen, and is limited to the case of quasi-static uniaxial tensile loading. For these conditions, a considerable amount of experimental data could be found in the literature. Only selected publications were chosen for the purpose of this review so that results would be representative of the different material systems and laminate configurations and be sufficiently numerous to allow an accurate assessment of the effect(s) of these parameters on the notch sensitivity of composite laminates and an evaluation of the various material parameters associated with the different fracture models presented in this report.

Several hundred data sets from notched strength tests were collected and evaluated. Several of the data sets are inconsistent which should be expected considering the complex nature of the subject matter and the fact that each investigator studied a different combination of material system, laminate configuration, type of discontinuity, fabrication procedure and testing procedure.

15.4 Correlation between Notch-Sensitivity and Fracture Model Parameters

The reviewed fracture models utilize a variety of parameters which must be determined experimentally. In all the models it is assumed that these parameters are constant, i.e. independent of notch size, and are to be considered as material parameters. It is of interest to identify which of these parameters can be correlated to the notch sensitivity of composite laminates containing circular holes and straight cracks. For this purpose, the ratio of notched to unnotched strength (σ_N^*/σ_0) at a specific hole size has been recorded from the data such as those listed in Fig. 15.1 and correlated with the various parameters associated with the different fracture models. The correlation between σ_N^*/σ_0 and various other parameters for a graphite/epoxy laminate with $2R/W=0.25$, typically, is shown in Figs. 15.2 through 15.11. Each point in these figures represents a set of notched strength data as shown, for example, in Fig. 15.1. Consequently, these figures

combine all the sets of notched strength data reviewed, irrespective of material system, constituents properties, fabrication procedures, laminate configuration, stacking sequence, specimen geometry, loading procedure, etc. Thus, significant scatter exists in the values of all the parameters and it is emphasized that conclusions regarding the presence or absence of correlation can only be qualitative, i.e. restricted to the specific specimen geometry, loading function, etc. which are analyzed in this study. It should be noted that although the results shown in Figs. 15.2 through 15.10 are for a specific notch size, similar figures and correlations are obtained for all other notch sizes. Evaluating the test data against the different fracture models, the following observations can be made:

1. WEK-fracture model: A correlation exists between notch sensitivity and a_c . The smaller a_c is, the more notch sensitive the subject material (Fig. 15.2).
2. WN-fracture model: A correlation exists between notch sensitivity and d_o (Fig. 15.3) and a_o (Fig. 15.4). The smaller the characteristic distances are, the more notch sensitive the subject material.
3. K-fracture model: No correlation could be found between the notch sensitivity and k_o .
4. PWG-Fracture model: No correlation could be found between notch sensitivity and the exponential parameter, m (Fig. 15.5), the notch sensitivity factor, c (Fig. 15.6), the notch shift parameter, a_c (Fig. 15.7), and the notch sensitivity factor, a_m (Fig. 15.8).
5. ML-Fracture model: No correlation could be found between the exponential parameter, n , and notch sensitivity (Fig. 15.9) with most values for n lying between 0.1 to 0.4. Neither could a correlation be found between the composite fracture toughness, H_C/σ_o , and notch sensitivity (Fig. 15.10).

Finally, another aspect deserves discussion, viz. the effect of model parameters selection on predictions. Many studies address

whether the constants associated with the different fracture models are independent of either material system or laminate configuration. The results shown previously clearly indicate that all the constants strongly depend on laminate configuration as well as other factors such as fabrication procedures, fiber properties, etc.. Consequently, the applicability of a given fracture model parameter is restricted to the specific set of data for which it has been determined. Fig. 15.11 shows representative notched strength data of a $[0_2/\pm 45]_S$ laminate compared with the WN-fracture model using relatively small and large values of d_o and a_o within the range of values listed previously. The characteristic distances, d_o and a_o , of the $[0_2/\pm 45]_S$ laminate have intermediate values. The comparison clearly indicates the degree of error which can result by choosing arbitrary values for d_o and a_o and applying them to all laminate configurations of a given material system.

15.5 References

- | | | |
|--------|---|--|
| [15.1] | Awerbuch, J. | Notched Strength Predictions of Graphite-Epoxy Laminates.
DFVLR-IB 131-83/21 (1983). |
| [15.2] | Waddoups, M.E.
Eisenmann, J.R.
Kaminski, B.E. | Macroscopic Fracture Mechanics of Advanced Composite Materials.
J. Composite Materials 5(1971), pp. 446-454. |
| [15.3] | Whitney, J.M.
Nuismer, R.J. | Stress Fracture Criteria for Laminated Composites Containing Stress Concentrations.
J. Composite Materials 8(1974), pp. 253-265. |
| [15.4] | Nuismer, R.J.
Whitney, J.M. | Uniaxial Failure of Composite Laminates Containing Stress Concentrations.
In: Fracture Mechanics of Composites. ASTM STP 593, 1975 Gaithersburg, Md., pp. 117-142. |
| [15.5] | Karlak, R.F. | Hole Effects in a Related Series of Symmetrical Laminates.
In: Proc. of Failure Modes in Composites, IV., The Metallurgical Society of AIME, 1977 Chicago, pp. 105-117. |
| [15.6] | Pipes, R.B.
Wetherhold, R.C.
Gillespie, J.W. | Notched Strength of Composite Materials.
J. Composite Materials 12(1979), pp. 148-160. |
| [15.7] | Pipes, R.B.
Gillespie, J.W.
Wetherhold, R.C. | Superposition of the Notched Strength of Composite Laminates.
Polymer Engineering and Science 19(1979), No. 16, pp. 1151-1155. |

- [15.8] Pipes, R.B.
Wetherhold, R.C.
Gillespie, J.W.

Macroscopic Fracture of Fibrous Composites.
Material Science and Engineering 45(1980), pp. 247-253.
- [15.9] Mar, J.W.
Lin, K.Y.

Fracture Mechanics Correlation for Tensile Failure of Filamentary Composites with Holes.
J. of Aircraft 14(1977) No. 7, pp. 703-704.
- [15.10] Poe, C.C.
Sova, J.A.

Fracture Toughness of Boron/Aluminum Laminates with Various Portions of 0° and ±45° Plies.
NASA Technical Paper 1707 (1980).

GR/EP	SP-286T300	[0/+45/-45/90]S	15039H.064
2R [mm]	2R/W	STRENGTH [MPa]	STRENGTH RATIO
0.00	0.00	502.0	1.000
0.20	0.00	491.5	0.979
0.40	0.00	434.0	0.865
0.40	0.00	463.0	0.922
1.60	0.01	387.9	0.773
1.60	0.01	380.9	0.759
4.80	0.04	285.6	0.570
4.80	0.04	308.5	0.615
6.40	0.05	281.3	0.562
6.40	0.05	270.3	0.540
12.70	0.10	260.2	0.524
12.70	0.10	244.4	0.492
19.10	0.15	213.6	0.436
19.10	0.15	237.0	0.484
25.40	0.20	199.7	0.416
25.40	0.20	218.8	0.456

GR/EP	SP-286T300	[0/0/+45/-45]S	15052H.064
2R [mm]	2R/W	STRENGTH [MPa]	STRENGTH RATIO
0.00	0.00	802.0	1.000
6.40	0.05	640.3	0.800
6.40	0.05	598.4	0.748
6.40	0.05	412.9	0.516
12.70	0.10	480.8	0.606
12.70	0.10	461.0	0.581
12.70	0.10	409.6	0.516
19.10	0.15	387.2	0.495
19.10	0.15	403.7	0.516
19.10	0.15	353.1	0.451
25.40	0.20	379.2	0.495
25.40	0.20	359.2	0.469
25.40	0.20	425.2	0.555

Fig. 15.1 Typical notched strength data

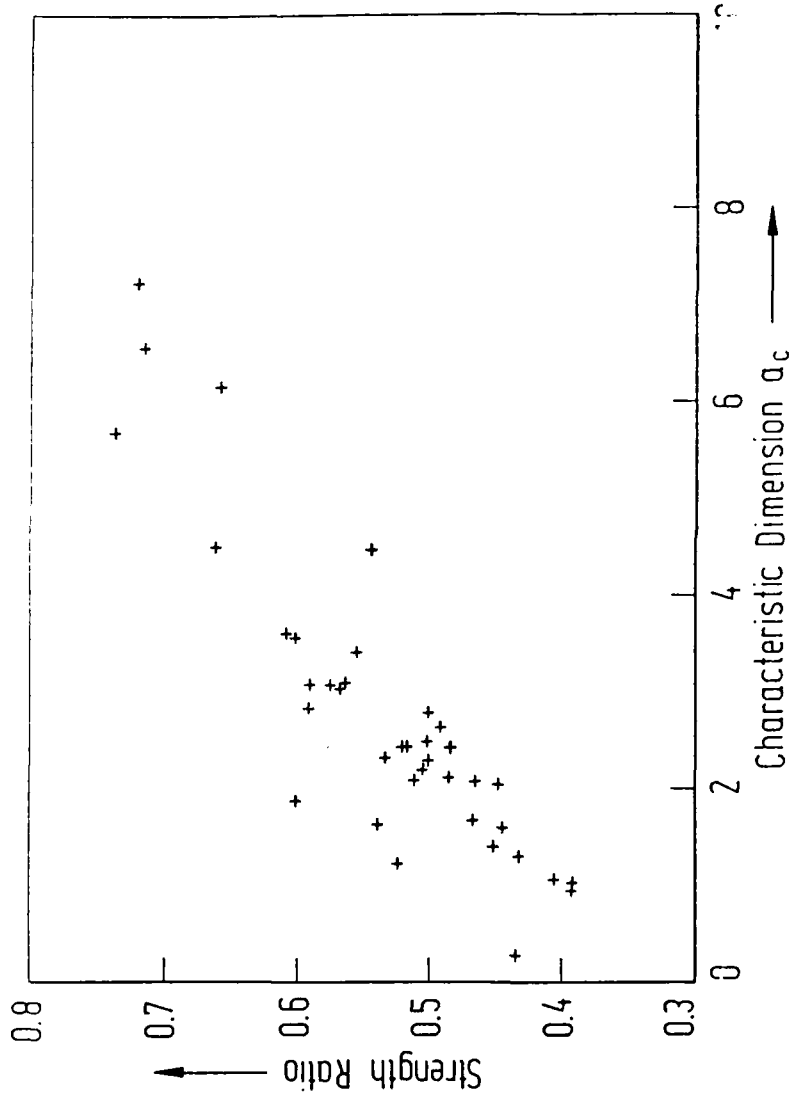


Fig. 15.2 Correlation between notched strength ratio and characteristic dimensions, a_c , (WEK-fracture model) for graphite/epoxy laminates containing circular holes ($2R/W = 0.25$).

DFVLR131-12/B-0034

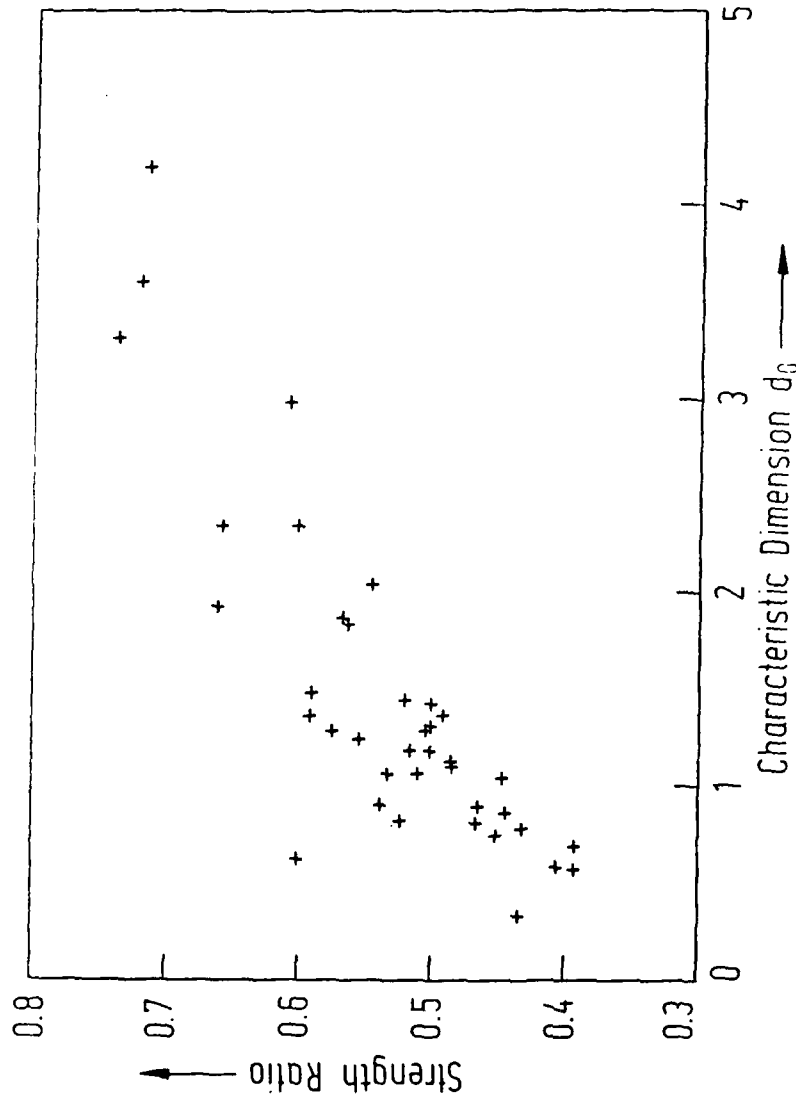


Fig. 15.3 Correlation between notched strength ratio and characteristic dimension, d_0 , (WN-fracture model, "point stress" criterion) for graphite/epoxy laminates containing circular holes ($2R/W = 0.25$).

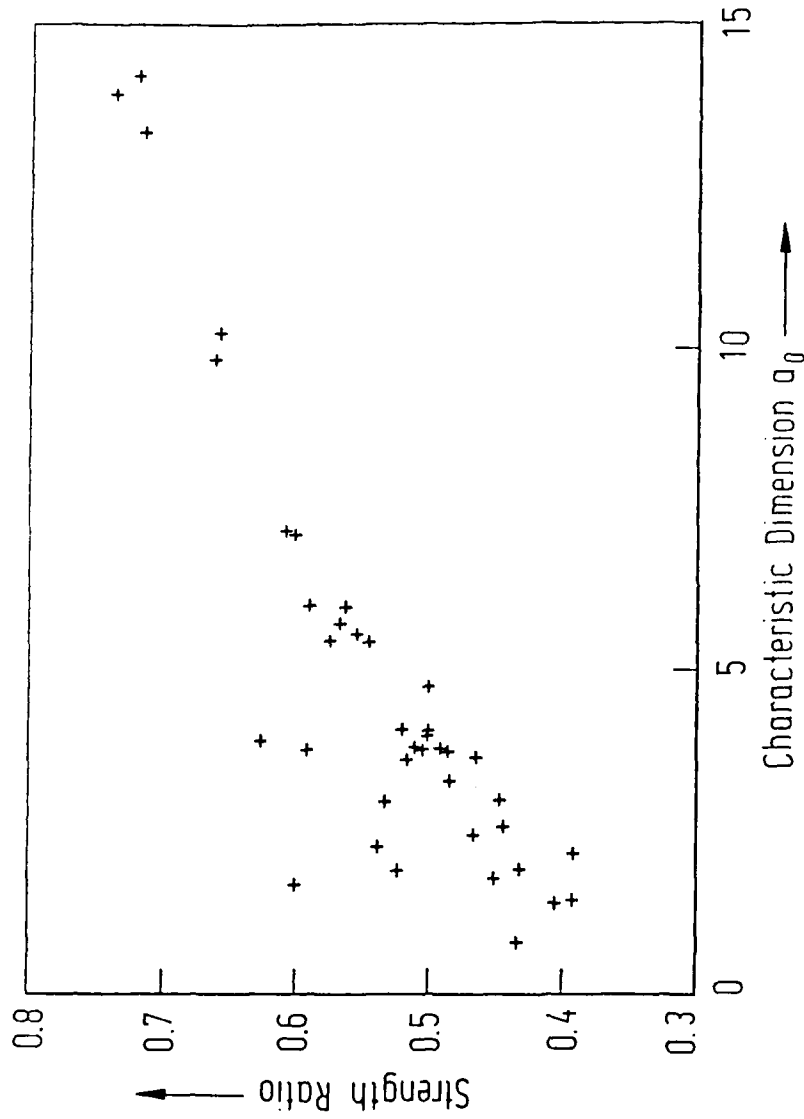


Fig. 15.4 Correlation between notched strength ratio and characteristic dimension, a_0 , (WN-fracture model, "average stress" criterion) for graphite/epoxy laminates containing circular holes ($2R/W = 0.25$).

DFVLR 131-12/R-0036

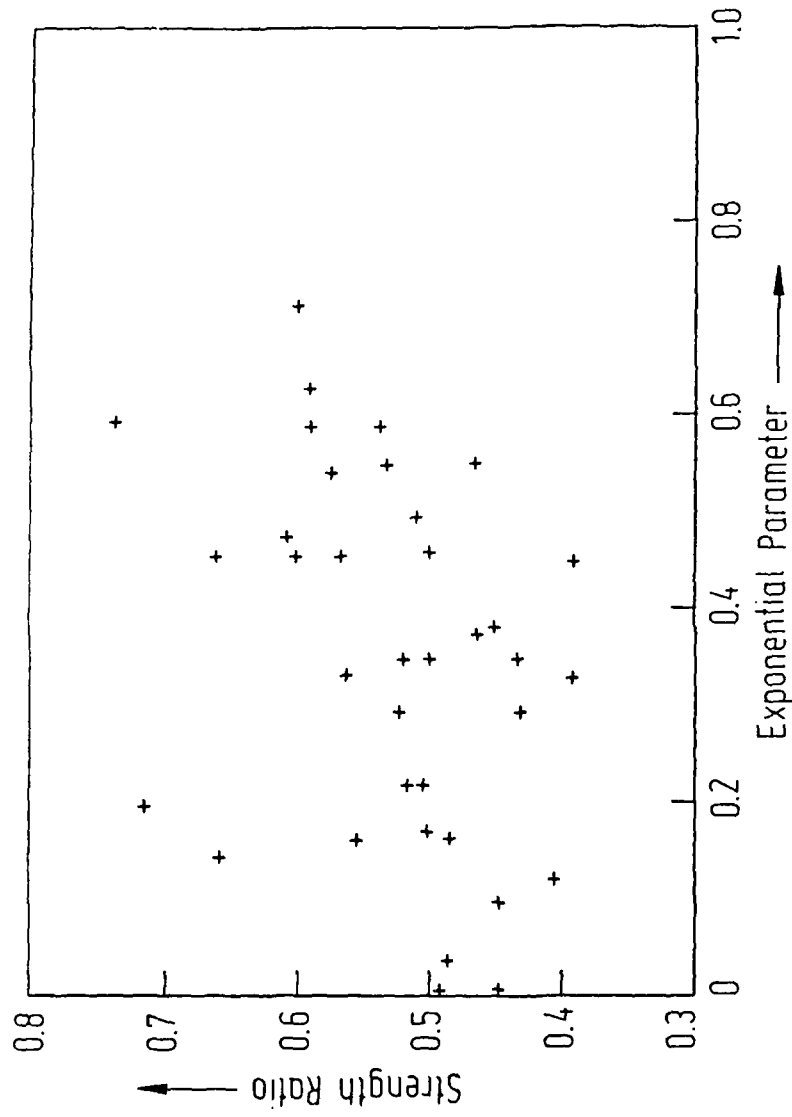


Fig. 15.5 Correlation between notched strength ratio and exponential parameter, m , (PWG-fracture model) for graphite/epoxy laminates containing circular holes ($2R/W = 0.25$).

DFVLR 131-12/B-0037

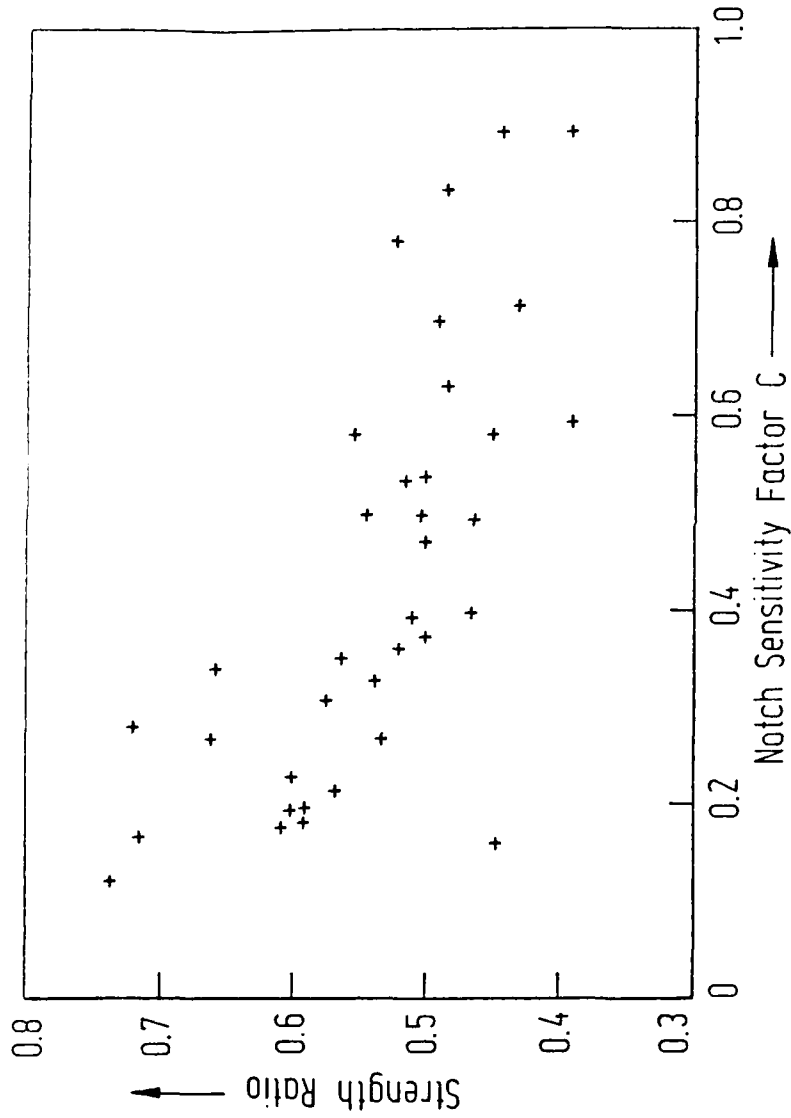


Fig. 15.6 Correlation between notched strength ratio and notched sensitivity factor, C , (PWG-fracture model) for graphite/epoxy laminates containing circular holes ($2R/W = 0.25$).

[DFVIR131-12/B-0038]

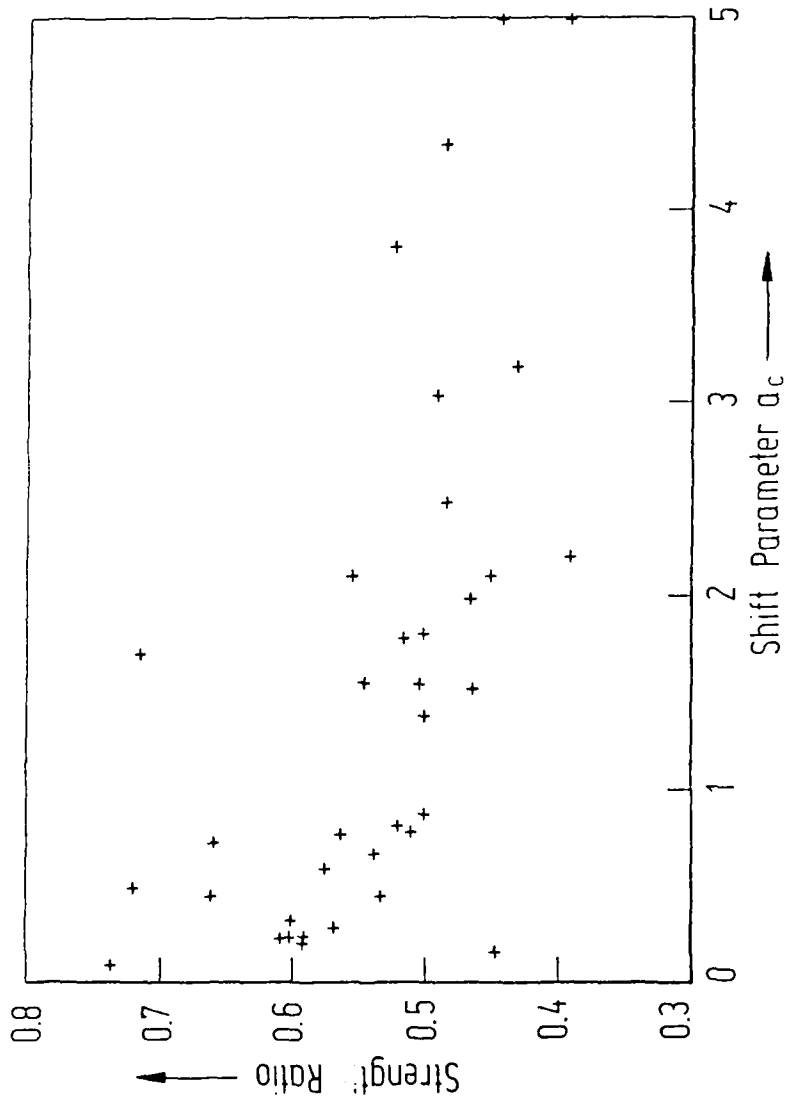


Fig. 15.7 Correlation between notched strength ratio and shift parameter, a_c , (PWG-fracture model) for graphite/epoxy laminates containing circular holes ($2R/W = 0.25$).

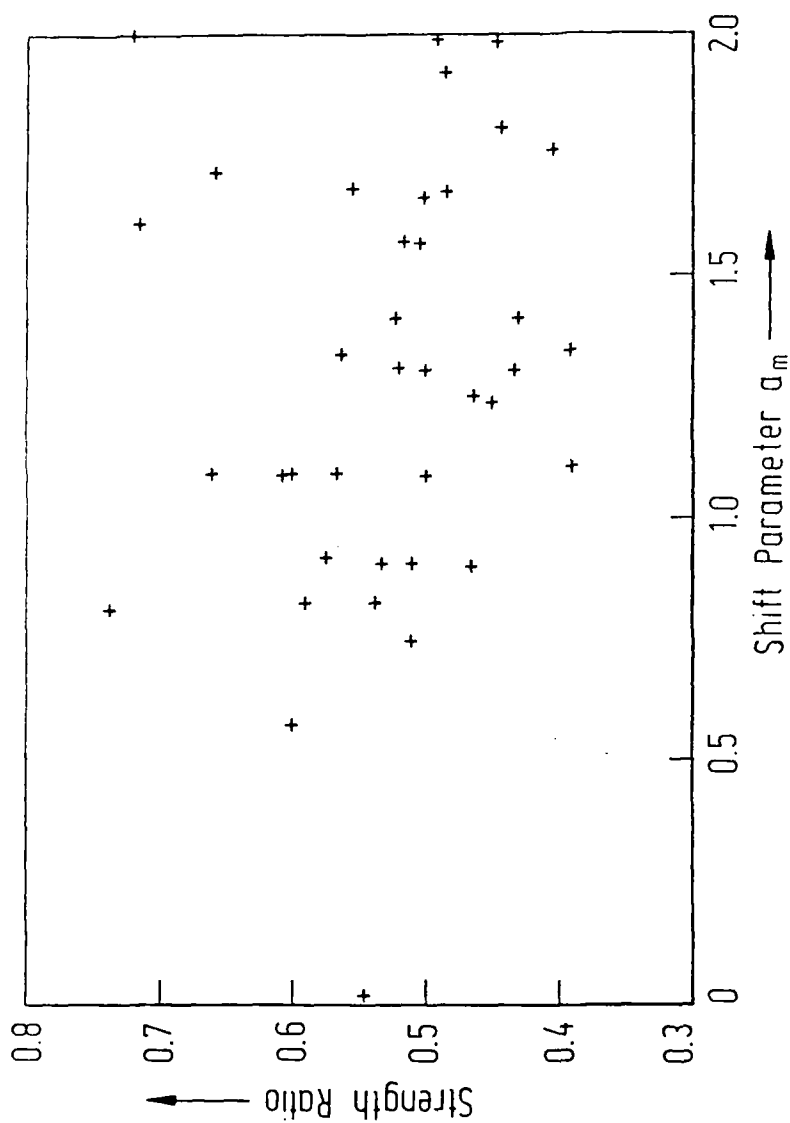


Fig. 15.8 Correlation between notched strength ratio and shift factor, a_m , (PWC-fracture model) for graphite/epoxy laminates containing circular holes ($2R/W = 0.25$).

DFVLR131-12/B-0040

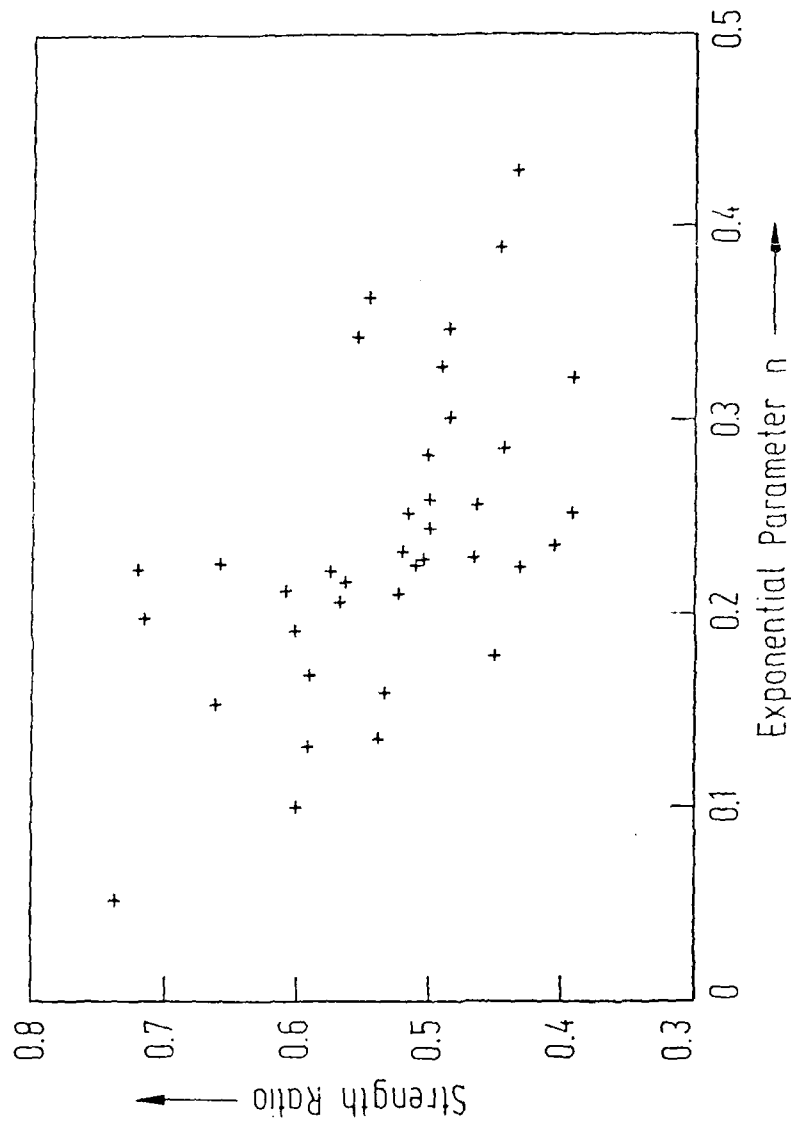


Fig. 15.9 Correlation between notched strength ratio and exponential parameter, n , (ML-fracture model) for graphite/epoxy laminates containing circular holes ($2R/W = 0.25$).

OFVLR131-12/8-0041

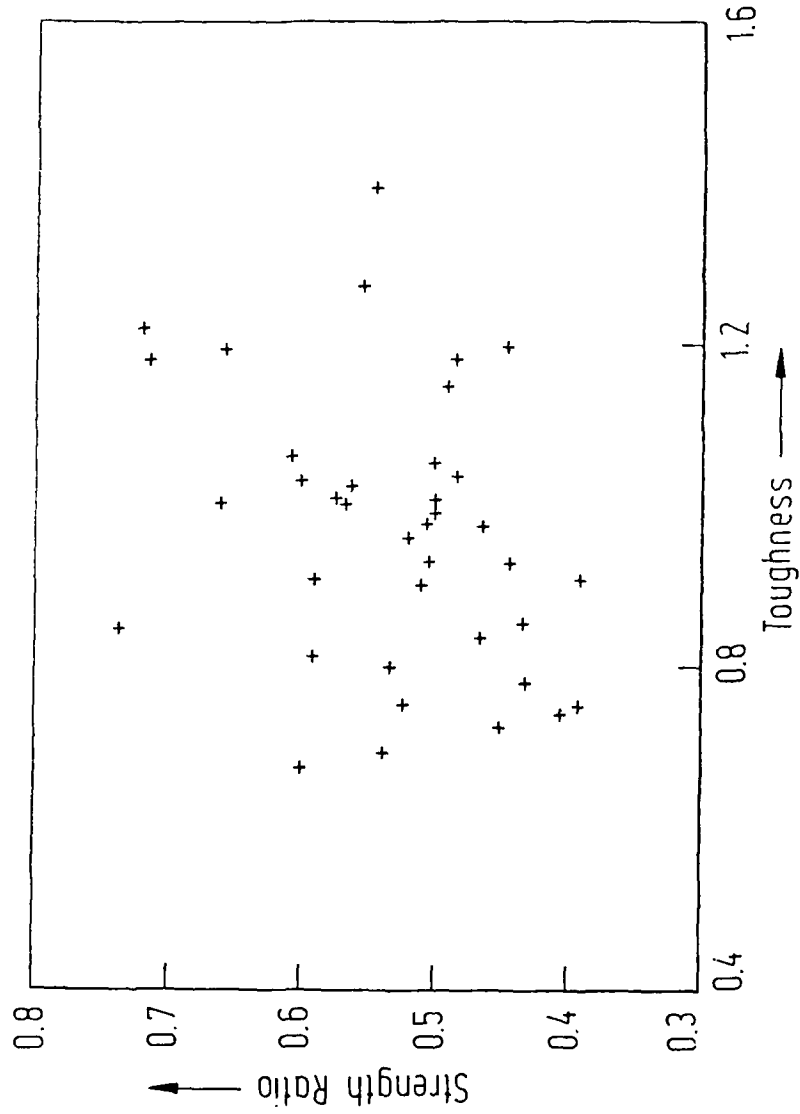


Fig. 15.10 Correlation between notched strength ratio and composite fracture toughness, H_c/a_0 , (ML-fracture model) for graphite/epoxy laminates containing circular holes ($2R/W = 0.25$).

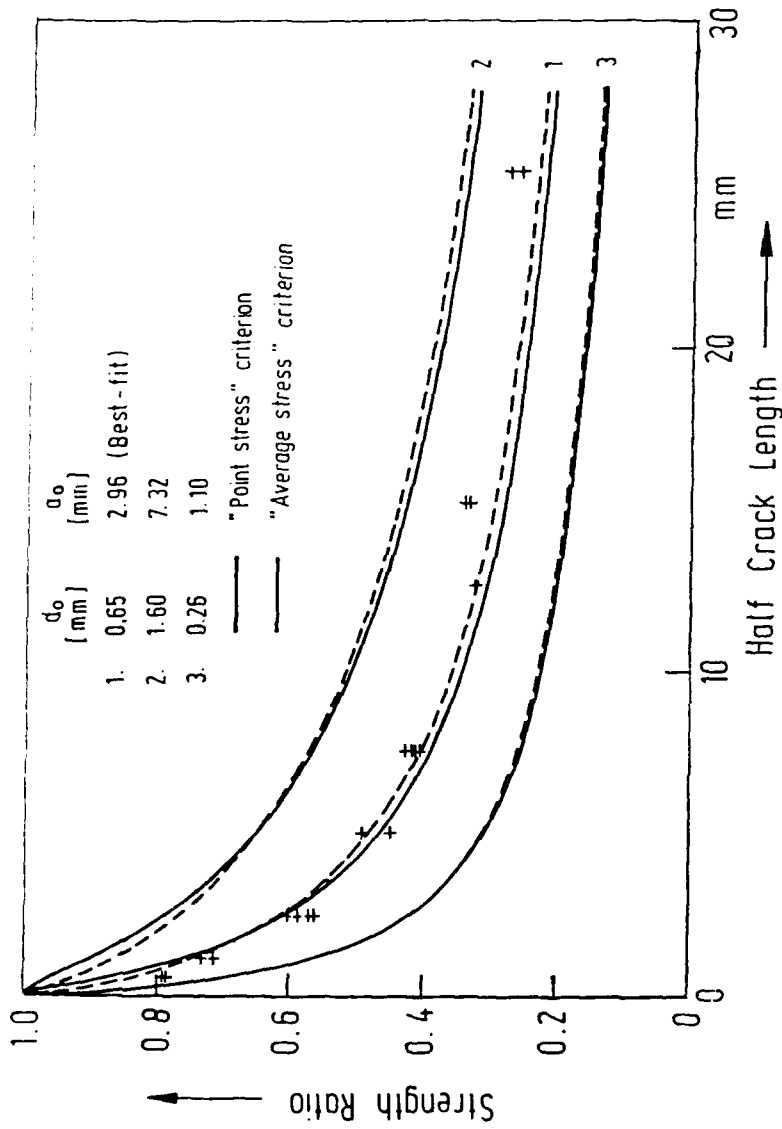


Fig. 15.11 Effect of the characteristic dimensions (WN-fracture model) on notched strength of boron/aluminum laminates containing straight cracks.

16. MECHANISMS OF FRACTURE

16.1 Summary

In contrast to metals where fracture under static or fatigue loads results from the nucleation and growth of a single dominant flaw, the fracture of fiber-reinforced composites is characterized by initiation and progression of multiple failures of different modes such as matrix cracks, interfacial debonding, fiber breaks and delaminations between adjacent plies of the laminates. The kinds of occurring failures, their distribution, time sequence and possible interactions depend on many parameters such as the properties of the fiber/matrix system, the stacking order and curing process, the influence of the environment, etc. The problem is further complicated by the possibility of fatigue failure in the compressive as well as in the tensile load regime, and by different failure modes under static and dynamic load applications. [16.1]. In order to gain insight into the mechanisms of the failure processes, the development of fatigue damage in unnotched multidirectional laminates was investigated under both tension and compression cycling. During and after fatigue loading specimens were examined for damage growth using light microscopy, scanning electron microscopy, ultrasonic C-scans and x-radiography. Matrix cracking and edge delaminations were found to be the dominant types of defects. Under fatigue loading these defects propagated due to unfavorable interlaminar stresses to the point where the specimens ultimately failed by short buckling or shearing. The test effort was accompanied by finite-element calculations for the assessment of the state of stress in critical zones. A damage growth model was developed for edge delaminations which correlates well with the test results.

Appendix I "Growth of Delaminations under Fatigue Loading" and Appendix K "Zur Auswahl eines CFK-Mehrschichtenverbundes für Versuche im Zugbereich" provide further details of this research topic.

16.2 Introduction.

Close observation of unnotched specimens tested under cyclic tension loads indicates that the progression of events follows a more or less distinct pattern. The first discernable damage usually are microcracks at certain intervals in the crossplies of the laminates. With increasing cycles more microcracks develop which tend to turn at the interfaces with neighboring plies and to form small delaminations both inside and, especially, at the free edges of the laminate. Additional delaminations emanate from the locations of fiber or fiber bundle breaks and lead to a damage state depicted in Fig. 16.1.

With respect to compressive loads, critical conditions may arise in the presence of delaminations induced by preceding high tensile loads, by lack of adhesion because of faulty manufacturing, or because of impact damage. Under sufficiently high compressive stresses the reduced stiffness of the separated sections will encourage their buckling and thereby induce a state of stress at the periphery of the delamination which tends to advance the crack front. Continuation of load cycling then leads to damage growth followed by massive separation and subsequent specimen failure.

Accompanying the gradually increasing damage state is a noticeable reduction of the overall laminate stiffness.[16.2]. Depending on the stacking order, this reduction may be as pronounced as shown in Fig. 16.2 for a matrix-controlled $[\pm 45]_{2S}$ -laminate, or as subtle as in the case of the fiber-controlled $[0_2, +45, 0_2, -45, 0, 90]_S$ -laminate shown in Fig. 16.3. In both instances, however, a particularly critical combination of local failure modes develops finally which leads to a rapid deterioration of the stiffness in only a few additional cycles and to what is commonly referred to as "sudden death" of the specimen. The sequence of the damage progression and the nature of the ultimate failure of fiber-reinforced laminates were the objectives of combined empirical and analytical investigations.

16.3 Test Procedure

The majority of the tests was performed with specimens dimensioned as shown in Fig. 16.4. The specimens were stored at 25°C and 50% RH for 3 to 6 months prior to testing. All tests were conducted on closed-loop servohydraulic testing machines. The machines were controlled by digital process computers allowing fast data acquisition and on-line monitoring of relevant test parameters. Strain gages were mounted to the specimens for displacement measurements. For the measurement of transverse contractions and of crack-opening displacements, magnetic-field-dependent resistors (DEVLR-MDR-transducers) were used. Special anti-buckling guides were designed for the lateral support of compression-loaded test specimens.

After prescribed static load steps or prescribed numbers of load cycles the specimens were removed from the testing machines and the extent of the growing delaminations were determined by ultrasonic scans. Dye-penetrant enhanced radiography was used to observe the onset and propagation of cracks. An evaluation was made of the topography of fracture surfaces by scanning electron microscopy.

16.4 Microcracks

The normally used epoxy resins exhibit very limited strain capabilities. In addition, the discrepant thermal expansions of the fibers and the resins induce adverse prestresses as a result of the curing process. Under these conditions the formation of microcracks can be expected in those plies of a laminate which are mechanically or thermally stressed beyond the critical strain values of the resin [16.3]. Typical examples of microcracks, observed radiographically in the crossplies of $[0,90]_g$ -laminates during a tension test, are shown in Fig. 16.5. Repeated exposures to high mechanical loads or to low temperatures will aggravate the state of damage. Fig. 16.6 shows that in $[\pm 45]_{2s}$ -specimens subjected to thermal cycling between +90°C and -155°C the cracks turn at the interfaces of adjacent plies and form local delaminations which tend to grow with increasing numbers of thermal

cycles. It stands to reason that a similar effect occurs in specimens subjected to sufficiently high mechanical load cycles. Delaminations of this kind occur most severely along the free edges but are likely to occur in the interior of the test specimens as well.

16.5 Edge Delaminations

During static tension tests as well as in tension-tension fatigue tests of $[0_2/+45/0_2/-45/0/90]_S$ -laminates similar types of damages were observed. First, a few isolated transverse cracks developed in the 90° -plies propagating in the transverse direction. With the formation of new cracks the average crack distance decreased. This was followed almost immediately by the onset of small delaminations along the tips of the transverse cracks as seen in Fig. 16.7. During increasing static load or number of cycles, the size of the initially discrete delaminations increased and led to the interconnection with other delaminations. The delaminations then grew rapidly and extended eventually over the entire length of the specimen. No significant differences were observed in this respect between static tension tests and tension-tension fatigue tests.

In tension-compression fatigue tests delaminations appeared between the 90° - and 0° -plies as well as between the 45° - and 0° -plies as shown in Fig. 16.8. After 30 000 cycles at a stress amplitude of 500 N/mm^2 and $R = -1$, a delamination between the 0° - and 90° -plies occurred with a crack opening size of about 0.1 mm. After unloading an opening size of about 0.02 mm remained because of the prestresses induced in the curing process of the laminate.

Growth of transverse cracks and edge delaminations simultaneously could be observed by means of penetrant-enhanced X-radiography, requiring the interruption of the test and the removal of the test specimen from the testing-machine. During monitoring of the decreasing compressive and tensile stiffness under fatigue load ($R = -1$) with type I-specimens the test was stopped and x-radiographs were taken at defined levels of stiffness loss. Fig. 16.9 shows the damage progression after a decrease of the

compressive secant modulus to 80% and 70% of the initial value. The transverse cracks form the characteristic pattern (CDS) and the average crack-length corresponds to the delamination size in the transverse direction. A view of the delamination at the right-side edge shows the distribution of cracks in both 90°-plies and the development of the edge delamination over the length of the specimen. In order to avoid an interruption of testing for non-destructive evaluation, an indirect method of damage growth measurement was developed. By means of the aforementioned DEVLR-MDR-transducer the transverse displacement c_m in the thickness direction of the specimen, which is indicative of the crack opening displacement of the edge delamination, could be measured on-line during static and fatigue loading [16.4].

The displacement c_m as a function of time is displayed under two constant stress levels in Fig. 16.10. The static loading was sporadically interrupted by unloading-loading intervals for measuring the opening displacements caused by the presence of the curing stresses. The curves show that the residual displacements grow to a more or less stationary value after approximately 160 min. A typical stress-displacement response during tension-tension fatigue test is plotted in Fig. 16.11. The display of the displacement envelope in Fig. 16.12 shows an increase of both amplitude and mean value as well as the onset of delamination growth after about 2200 cycles. The delamination size was monitored by C-scan and the distance between the crack tip of the delamination and the edge of the specimen was established by SEM.

16.6 Stress Analysis

The delaminations of unnotched laminates are initiated by very intense interlaminar stresses present at the free edges. A quasi-three-dimensional finite element analysis was performed by use of the FE-program ASKA in order to support quantitative predictions of onset and growth of the delaminations [16.5] [16.6]. Appendix K "Zur Auswahl eines CFK-Mehrschichtenverbundes für Versuche im Zugbereich" provides further details of this research topic.

Because of its double-symmetry only one quarter of the section needed to be analyzed. The model and its coordinate system are shown in Fig. 16.13. Fig. 16.14 illustrates the distribution of tensile stresses σ_{11} in the individual layers, which are up to 40% higher than the far field stress of 1000 N/mm^2 without significant increase towards the free edge of the test specimen. Fig. 16.15 shows the shear stress σ_{12} within and between the layers.

Whereas the transverse stresses σ_{22} and the shear stresses σ_{23} are going to zero at the edge, the peeling stress σ_{33} in the 90° -layer exhibit a stress peak between the 90° - and the 0° -layer as demonstrated in Fig. 16.16. Similarly, the shear stresses σ_{13} show peaks at the edge in both directions as can be seen in Fig. 16.17. With the aid of these stress distributions the crack initiation and the crack propagation during static and fatigue testing can be explained. Calculations were also carried out for test specimens with a delamination at the edge between the 90° -plies showing the peeling stress σ_{33} and the shear stress σ_{13} at the crack tip to be of the same order compared with the corresponding edge effect stresses.

Although a good correlation exists between these stress distributions, the deformation of the cross section and the observed damage it is useful only for special cases of modelling damage growth. An alternative approach was based on the yield stress criterion and on the assumption of nonlinear stress-strain behaviour in a small plastic zone around the stress concentration. The result is an equation for the delamination opening displacement c_m as a function of delamination size and axial stress, whose derivation is given in Appendix I "Growth of Delamination under Fatigue Loading".

The corresponding calculations of the delamination size as a function of the displacement c_m were compared with C-scans of different delamination states and, additionally, with the measurement of the delamination size by a scanning electron microscope after sectioning the test specimen in the transverse direction. In all cases the calculated delamination size agreed very well with the observed size. A comparison between the measured stress-displacement curves of tension-tension fatigue,

displayed in Fig.16.11, and the calculated results at selected different delamination states is shown in Fig. 16.18. The dashed lines represent the calculated stress-displacement curves for different sizes of delaminations, demonstrating the good correlation between experimental and analytical results.

16.7 Fatigue and Residual Strength Model

It is well known that under quasi-static as well as compressive fatigue loading, failure occurs by buckling or kinking of individual fibers, fiber bundles or fiber layers due to insufficient support by the matrix. The supporting effect is reduced as the delamination propagates, and the buckling of a portion of the cross-section finally leads to the fracture of the remaining cross-section. The delamination state of a multidirectional test specimen containing 90°-plies has no significant influence on the residual tensile strength or tensile fatigue. Contrarily there is a remarkable sensitivity to compressive loading. In all tests performed under tension-compression loading ($R = -1$), monitoring of the last cycles before failure showed the failure of the specimen to occur during a compression cycle as shown in Fig. 16.3.

Therefore, an approach to the assessment of residual fatigue strength was developed by correlating the delamination growth or damage state, and the residual compressive strength. The growth of the delamination can be compared with the growth of a crack length given by the well known equation from fracture mechanics:

$$(1) \quad \frac{da}{dN} = g \bar{\sigma}^{\kappa} a^m$$

where a is the delamination size, N the number of cycles, σ a reference stress in the vicinity of the delamination crack tip and g , κ and m constants to be determined empirically. The number of cycles N_d corresponding to the delamination size a_d is given after integration by;

$$(2) \quad N_d = (a_d^{(1-m)} - a_{N=0}^{(1-m)}) / (1-m) g \bar{\sigma}^{\kappa}$$

It is now assumed that a critical delamination size a_F causes the failure of the test specimen. The derivation of this relation is described in Appendix I:

$$(3) \quad \sigma_F = \left(1 - \frac{G_F}{G_c}\right) \frac{A}{h} \frac{E}{E_i}$$

where σ_F is the critical compressive stress, σ_c the compressive strength of the virginal specimen, A the cross section, h the thickness of the delamination strips, E the modulus of the non-delaminated and E_i the modulus of the delaminated cross section. In the same way a critical damage size a_R can be expressed for the residual strength by:

$$(4) \quad \sigma_R = \left(1 - \frac{G_R}{G_c}\right) \frac{A}{h} \frac{E}{E_i}$$

where σ_R is the residual compressive strength at a given number of cycles N_R . The damage state D generally can be formulated as a function of the ratio N_R and N_F

$$(5) \quad D = f\left(\frac{N_R}{N_F}\right)$$

Substitution of N_R and N_F by Eqs. 2, 3, and 4 leads to

$$(6) \quad D = f\left(\frac{G_c - G_F}{G_c - G_R}\right)^{1-m}$$

This relation can be simplified in order to obtain a first approach for the damage state:

$$(7) \quad D = \left(\frac{G_c - G_R}{G_c - G_F}\right)^{1-m}$$

The validity of this formula was examined by comparison to results of fatigue tests. Fig. 16.19 shows the S-N-curve and the residual strength after tension-compression cyclic loading. Whereas the residual tensile strength remains nearly constant without significant changes, the residual compressive strength diminishes continuously to the fatigue stress σ_F associated with the number of cycles to failure, N_F . Because of the scatter of the test results equation (6) was expanded by correction terms to

$$(8) \quad D = \alpha + (1-\alpha) \left(\beta \frac{G_c - G_R}{G_c - G_F}\right)^{1-m}$$

where $\alpha = \alpha_1 + \bar{\alpha}$

α_1 = statistical scatter for a given failure probability based on static strength;

$\bar{\alpha}$ = average damage of a virgin specimen with 50% probability of failure;

β = statistical scatter for a given probability of survival based on the load cycles to failure.

The corresponding scatter distributions are displayed in Fig. 16.20 represented by curves of equal probability of survival of 90%, 50% and 10%. The damage D to be determined in the residual strength investigation was calculated from equation (5) and entered into Fig. 22. Evaluation of test results determined the exponent m to be approximately 0.45. Taking into account the scattering of the test results, Fig. 16.20 shows that the delamination progress can be described by means of equations (3), (4) and (5) as a first approach to a correlation between the delamination size and the residual compression strength.

16.8 Central Delaminations

Apart from the free edges of a laminate, delaminations may occur in the central regions as a consequence of microcrack formation and growth, or because of local lack of adhesion between adjacent plies caused either by a processing fault or by impact damage during service. The response of such delaminations under static and cyclic loads is a major aspect of the damage mechanics program.

The introduction of delaminations in test specimens is possible by the inclusion of an outgassing agent, by the imbedment of a very thin teflon disk prior to curing, or by controlled impacting after curing. The former has the advantage of providing a well-defined geometry and location and was adopted for the majority of the studies. Numerous tests have proven that the somewhat blunted crack front does not significantly retard the eventual growth of the delamination [16.7].

Fig. 16.21 shows, in terms of ultrasonic records, the progressive growth of a delamination under a gradually increasing compressive

load in a standard test specimen. The 0.1 mm thick teflon disk was placed between the 90°-plies at the midplane of the specimen. Up to approximately 85% of ultimate load the delamination is seen to be stable and to then grow in the direction of the fibers of the neighboring plies. The same kind of test specimen loaded in tension exhibits a very different behavior. Fig. 16.22 shows that, while the central delamination remains unchanged up to failure of the specimen, edge delaminations occur along the free boundaries at approximately 80% of ultimate load which subsequently gradually increase. Fig. 16.23, finally, illustrates the response of a test specimen under cyclic load with $R = -1$ and a stress level of ca. 50% of its static strength. After 20,000 cycles the first evidence of central delamination growth and onset of edge delaminations is noticeable, which gradually increase in severity until failure after 140,000 cycles. Fig. 16.23 also indicates the formation and random distribution of an increasing number of local delaminations, not to be found under static loads.

Variations of the diameter of the delaminations or of their location within the laminate stacking order, obviously, will produce different results. Fig. 16.24 summarizes some of the accumulated test data which indicate that the size of the delaminations is less significant than their location. A ready explanation is the increasing tendency of the thinner of the separated section to buckle outwards and to thereby aggravate the state of stress at the perimeter of the delamination.

16.9 Fiber Breaks and Fiber Debonds

Observable also on an initially microscopic level are failure modes such as fiber breaks and fiber debonds.

In highly stressed laminates fibers may rupture prematurely, individually or in small bundles, because of their imperfect shapes or imperfect alignment. Especially in fiber-controlled stacking orders the resulting redistribution of stresses in the vicinity of such discontinuities may initiate the type of local failure modes which affect the fracture behavior of the laminate. Fig. 16.25 depicts the observation of the break of a fairly mas-

sive fiber bundle by the grid-reflection technique as well as the associated spalling and cracking of the affected zone.

The loss of adhesion between fiber and matrix is often referred to as debonding. The cause may be a locally faulty surface treatment, or the gradual deterioration of an initially good bond by mechanically or thermally induced fatigue. An example of latter is given in Fig. 16.26, showing the fracture surfaces of tension-loaded specimens before and after severe thermal cycling. While prior to cycling the many specks of resin adhering to the fiber surfaces indicate a reasonably strong bond, the much smoother surfaces after cycling seem to signal the loss of it. It may be expected that similar degradations take place under mechanical cycling. As a consequence of progressive debonding, a gradual deterioration of the laminate stiffness might be expected. Fig. 16.27 seems to lend credence to this argument although it is not clear to what extent additional cracking contributes to the stiffness degradation.

16.10 References

- [16.1] Jube, G. Characterization, analysis and significance of defects in composite materials. AGARD-CP-355 (1983), 21 individual reports.
- [16.2] Prinz, R. Experimental and analytical study of strength degradation during fatigue of graphite/epoxy laminates. ICAF-DOC No.1336 (1983) pp. 2.3/1-2.3/33. Edited by GEAT, Toulouse.
- [16.3] Hartung, W. Effects of simulated space environment on the properties CFRP. Composite Technology Review (1984)
- [16.4] Prinz, R. Growth of delamination under fatigue loading. In [16.1] AGARD-CP-355 (1983) pp. 5.5 - 5.27
- [16.5] Rohwer, K. On the determination of edge stresses in layered composites. Nuclear Engineering and Design 70(1982) pp. 57 - 65
- [16.6] Rohwer, K. Stresses and deformations in laminated test specimens of CFRP. CFRP. DFVLR-Forschungsbericht 82-15 (1982).
- [16.7] Prinz, R. Damage propagation in CFRP under cyclic loading. ESA-TT 758 Dec.1982 pp. 128-173.

16-13

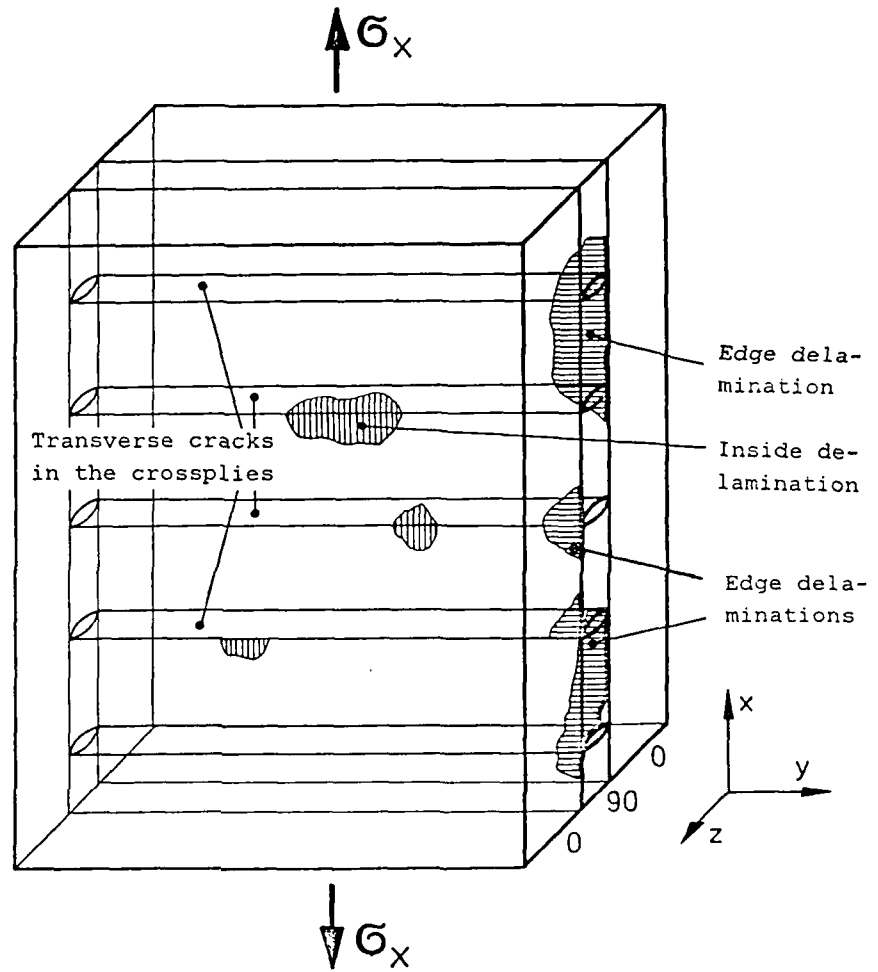


Fig. 16.1 Matrix cracks in the crossplies and onset of delaminations both inside the specimen and on its free edges.

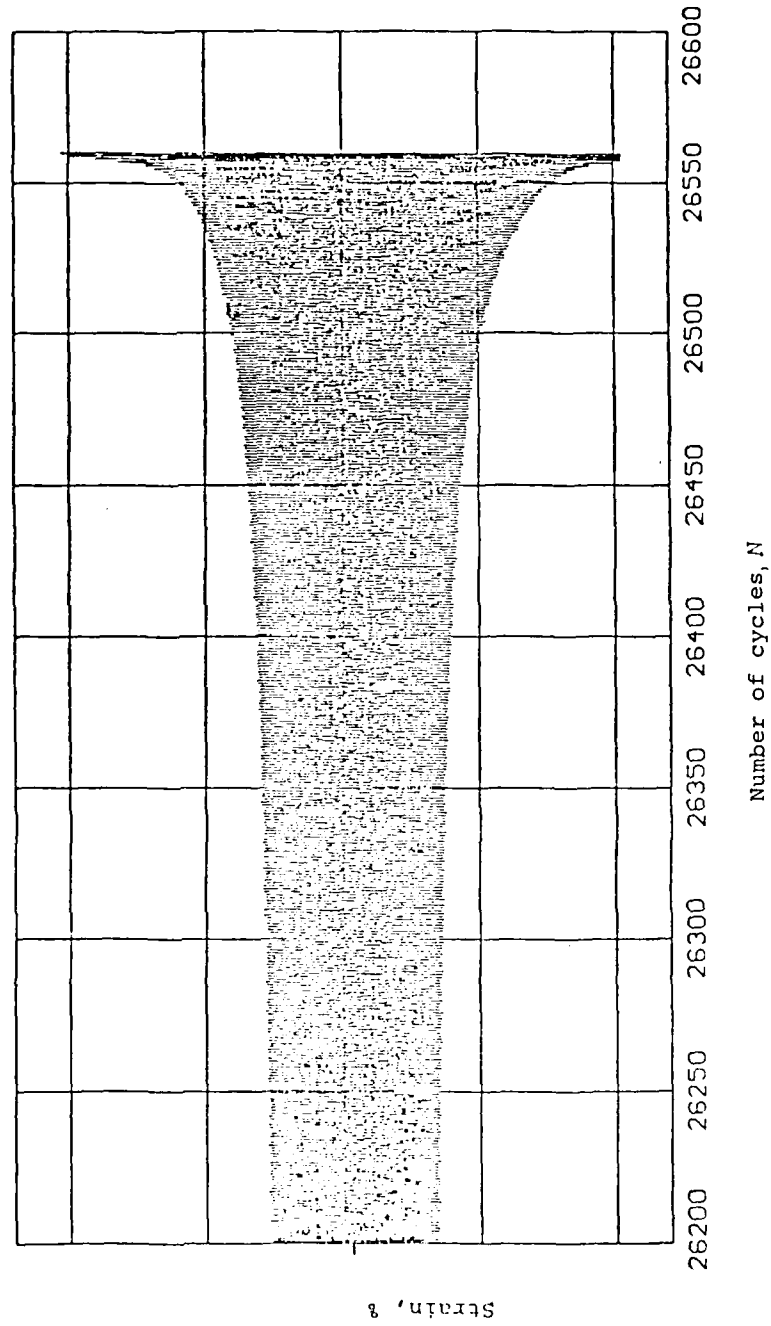


Fig. 16.2 Gradual increase of strain during load-controlled tension-compression test. Laminate Stacking order $[\pm 45^\circ]_{2s}$.

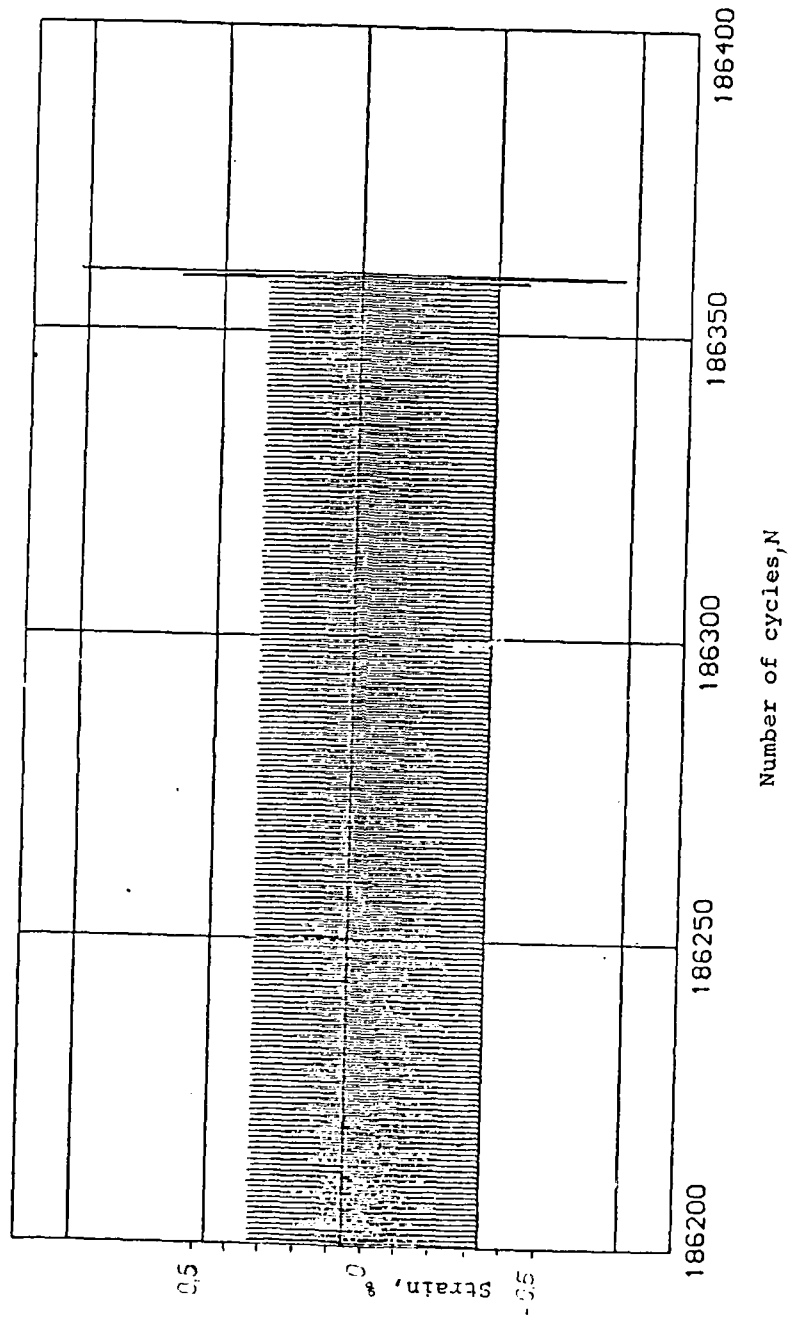
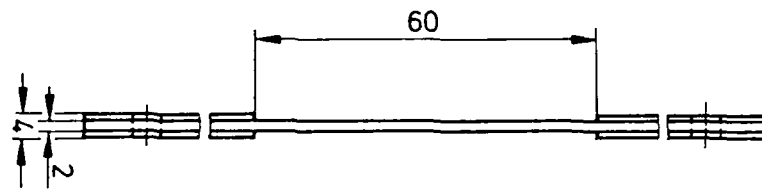
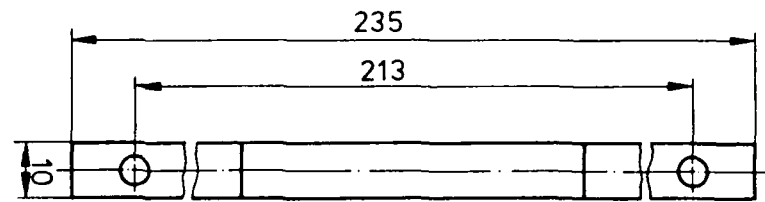
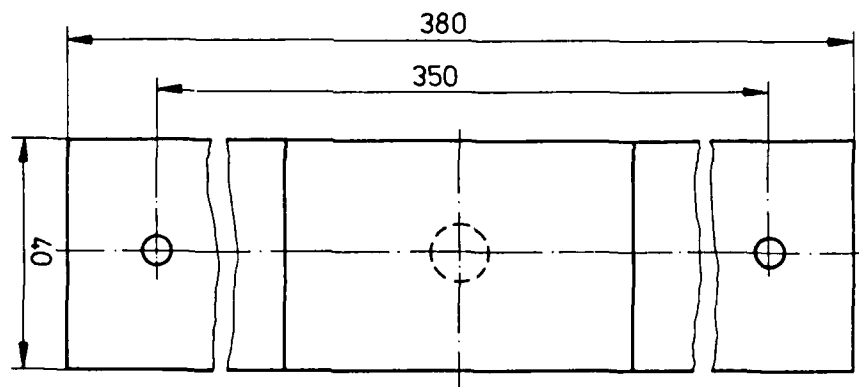
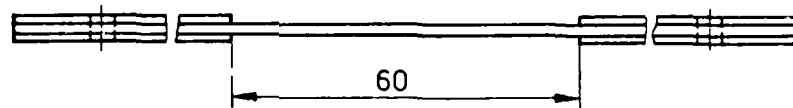


Fig. 16.3 Sudden increase of strain during the last two cycles before failure in load-controlled tension-compression test. Laminate stacking order $[0_2, +45, 0_2, -45, 0, 90]_s$.

16-16



Type II



Type I

Fig. 16.4 Types of test specimen.

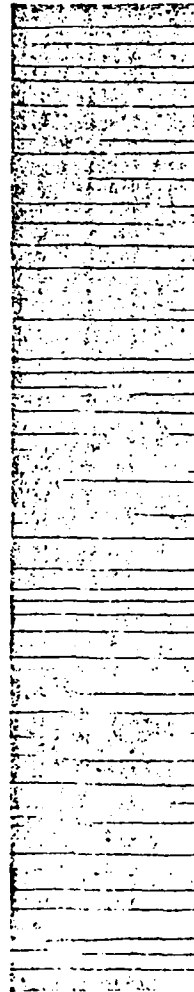
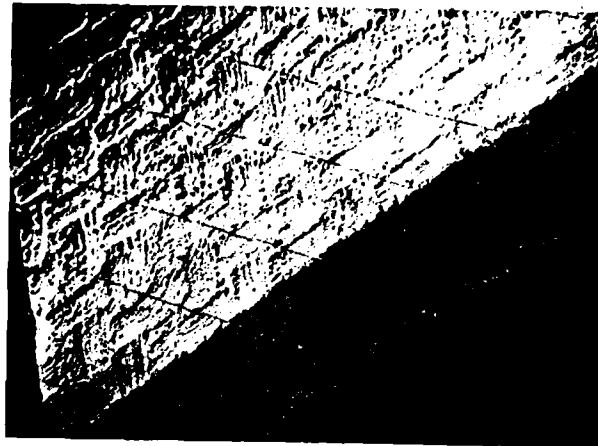


Fig. 16.5 X-ray photograph of a cross-ply laminate after static tension loading.



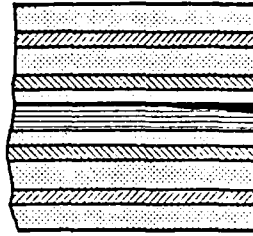
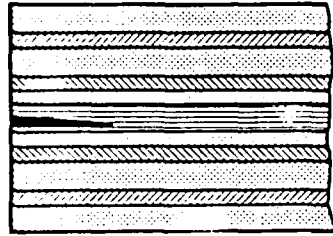
Surface and Cross Section (30x)



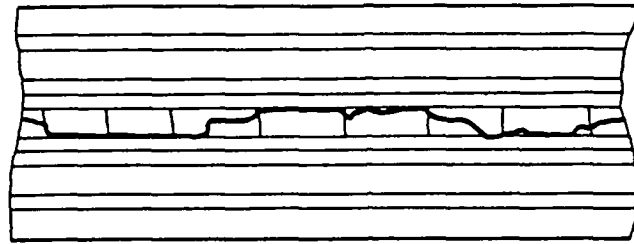
Cross Section (400x)

Fig. 16.6 Damage state of thermally cycled $[\pm 45^\circ]_{2s}$ -specimen.

$0_2/-45/0_2/-45/0/90_2/0/-45/0_2/-45/0_2$

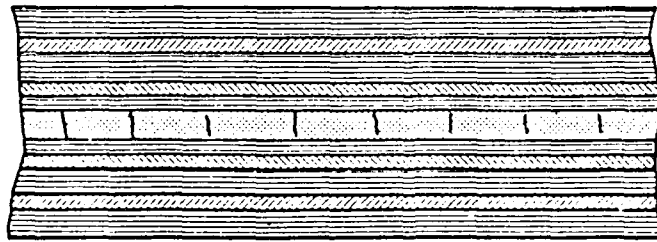


Cross Section



Edge Delamination
Onset Spanning the Entire Length

$0_2/-45/0_2/-45/0/90_2/0/-45/0_2/-45/0_2$



Transverse Cracks

Fig. 16.7 Development of an edge delamination under static tension load.

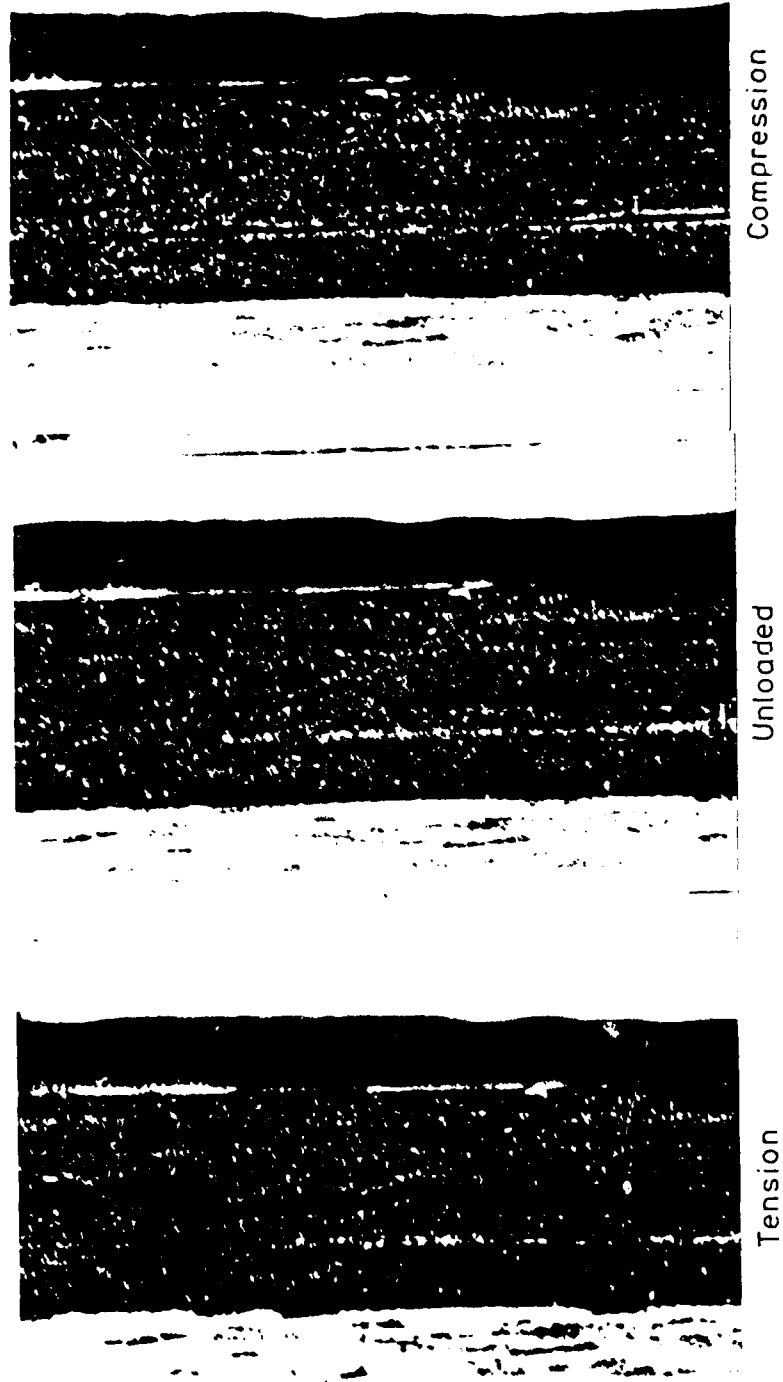
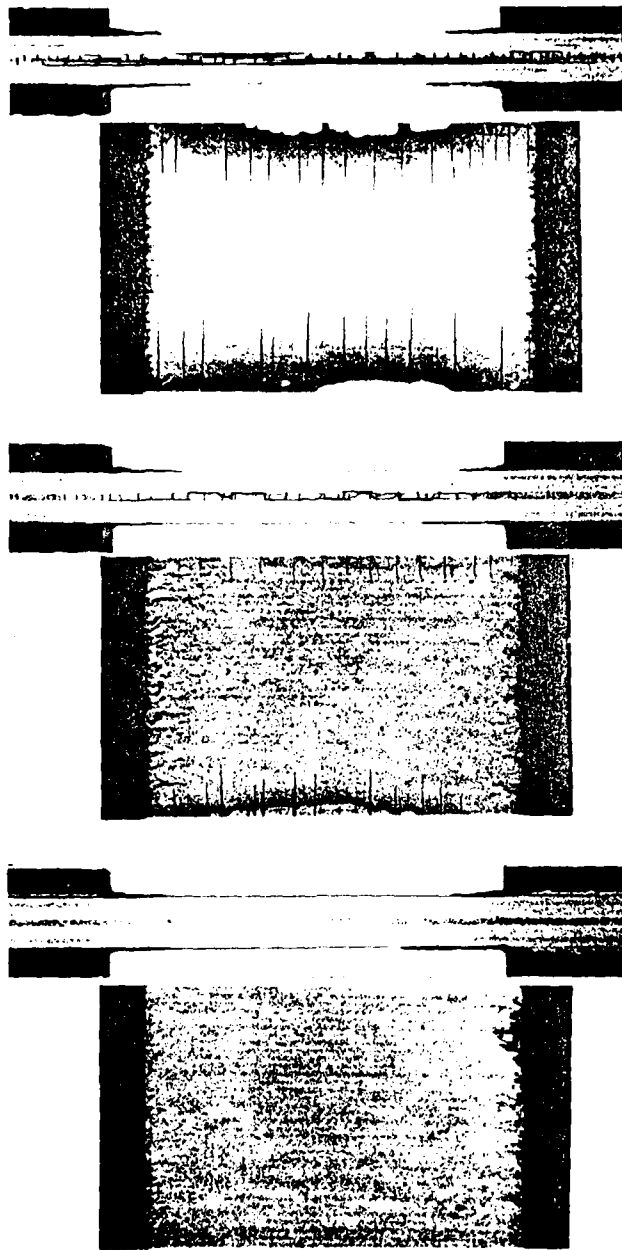


Fig. 16.8: Crack opening micrographs under tension-compression loading, $\sigma = \pm 500 \text{ N/mm}^2$.



Steifigkeit : 100%

80%

70%

Fig. 16.9 X-radiographs after tension-compression fatigue.

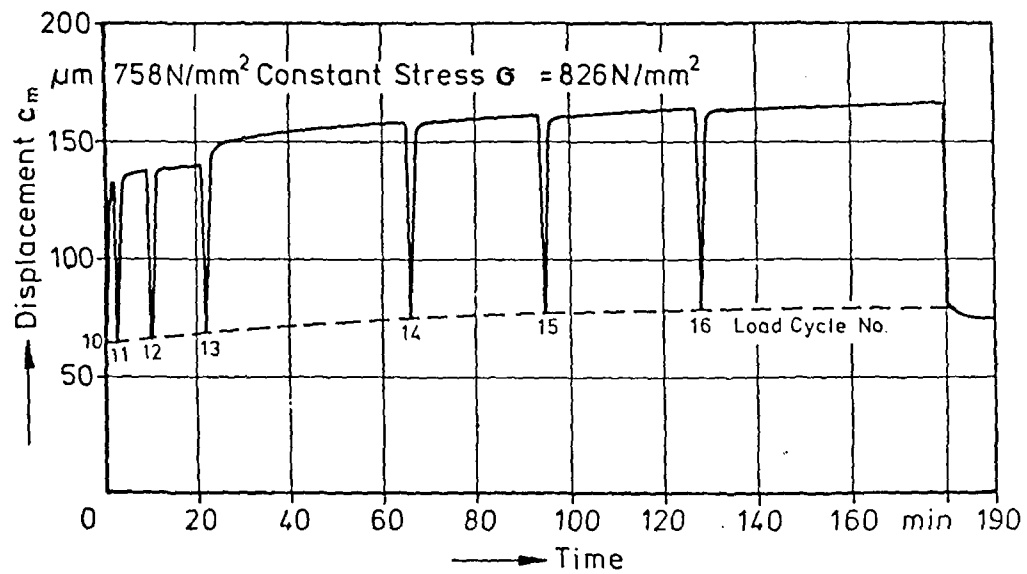
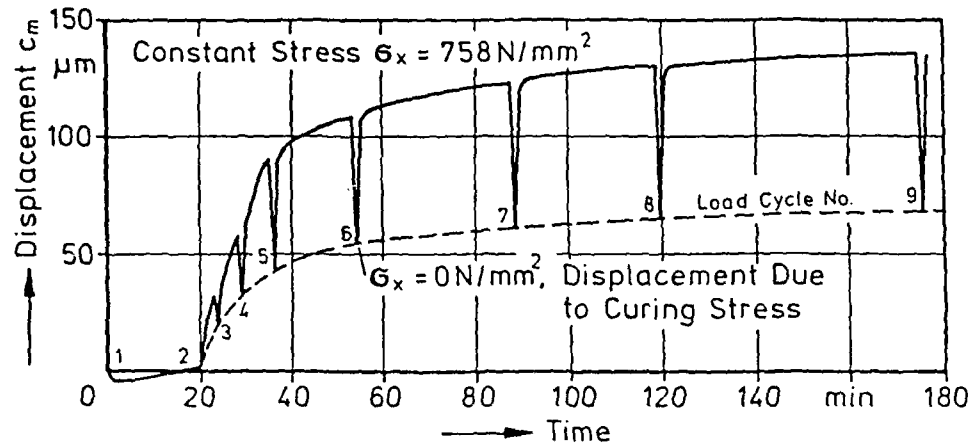


Fig. 16.10 Displacement c_m as function of time under constant stress levels.

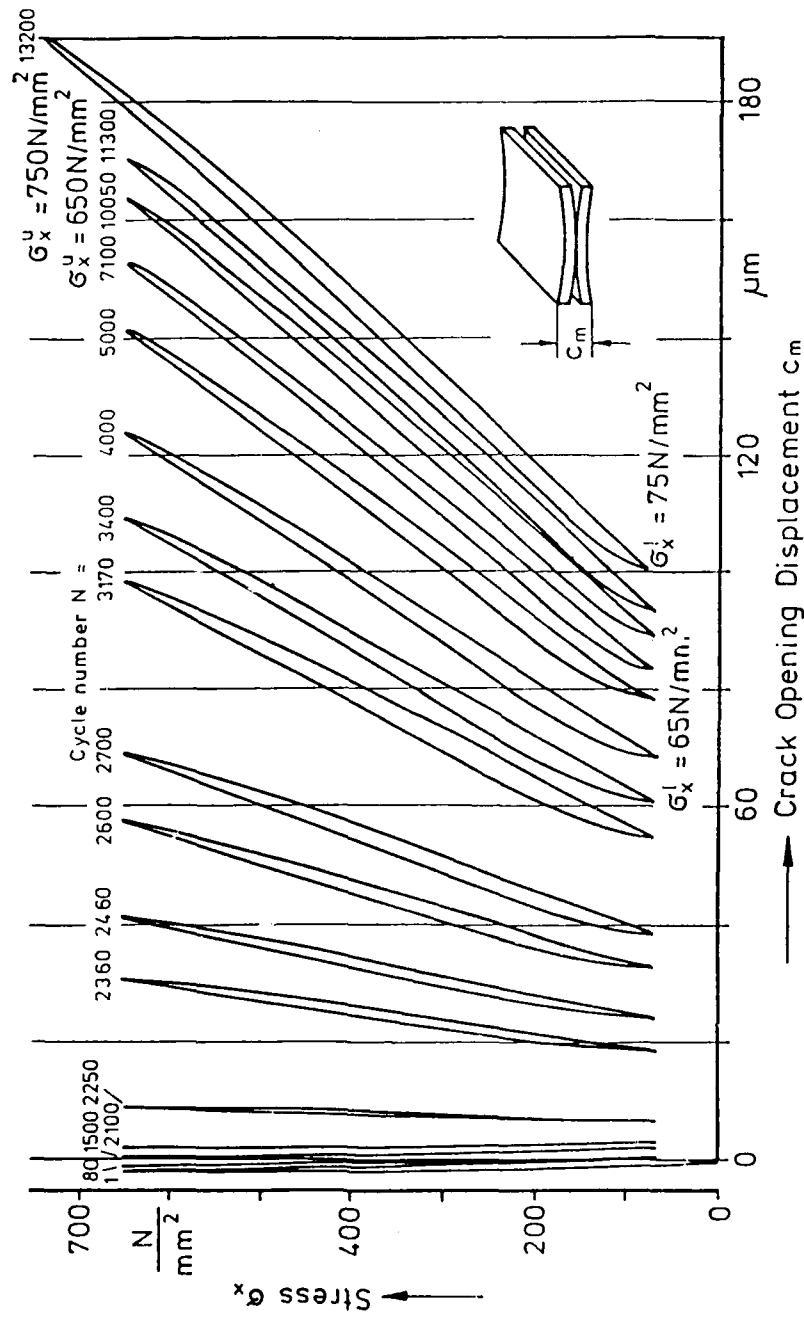


Fig. 16.11 Typical stress-displacement response for various numbers of load cycles in tension-tension fatigue test

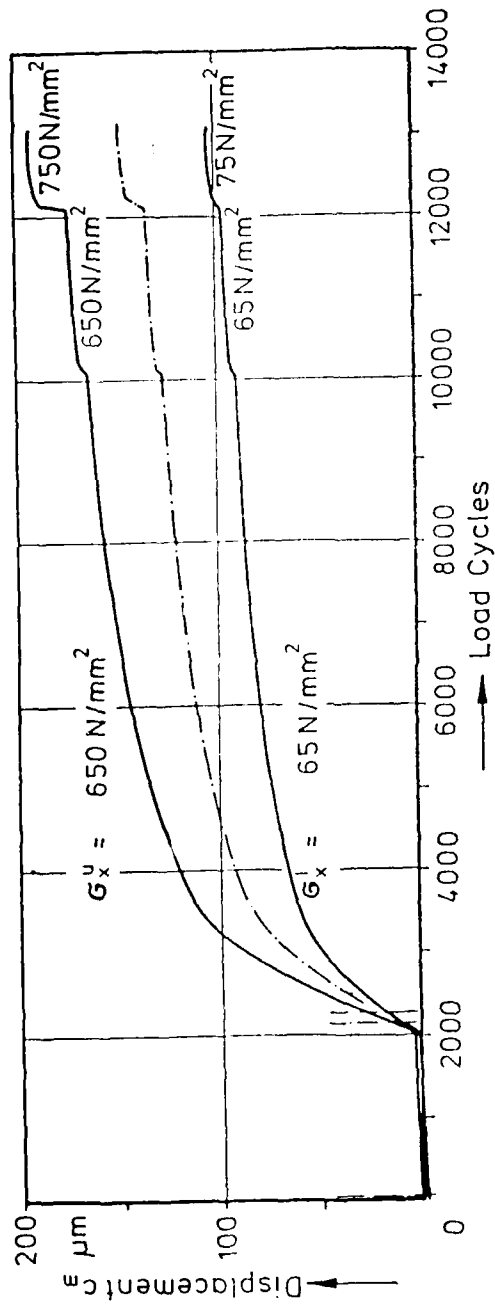


Fig. 16.12 Envelope of displacement c_m at the upper and the lower stress levels during tension-tension fatigue.

16-25

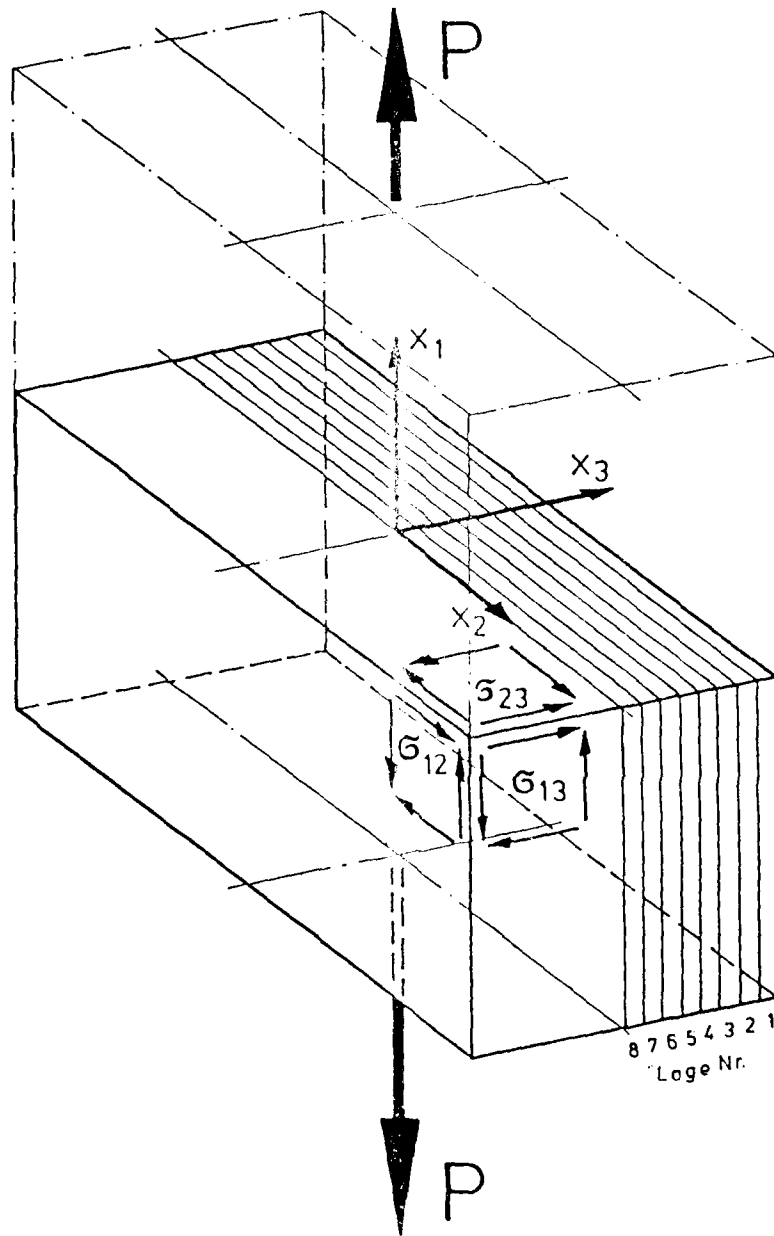


Fig. 16.13 Coordinate system and stress directions.

AD-A168 003

DEVELOPMENT OF FRACTURE MECHANICS MAPS FOR COMPOSITE
MATERIALS VOLUME 2 (U) DEUTSCHE FORSCHUNGS- UND
VERSUCHSANSTALT FUER LUFT- UND RAUMF... H W BERGMANN
DEC 85 AFMRL-TR-85-4156-VOL-2

3/3

UNCLASSIFIED

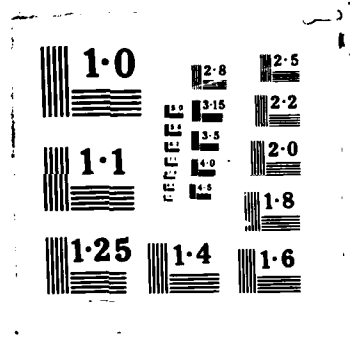
F/C 11/4

NL

END

FILE

6-58



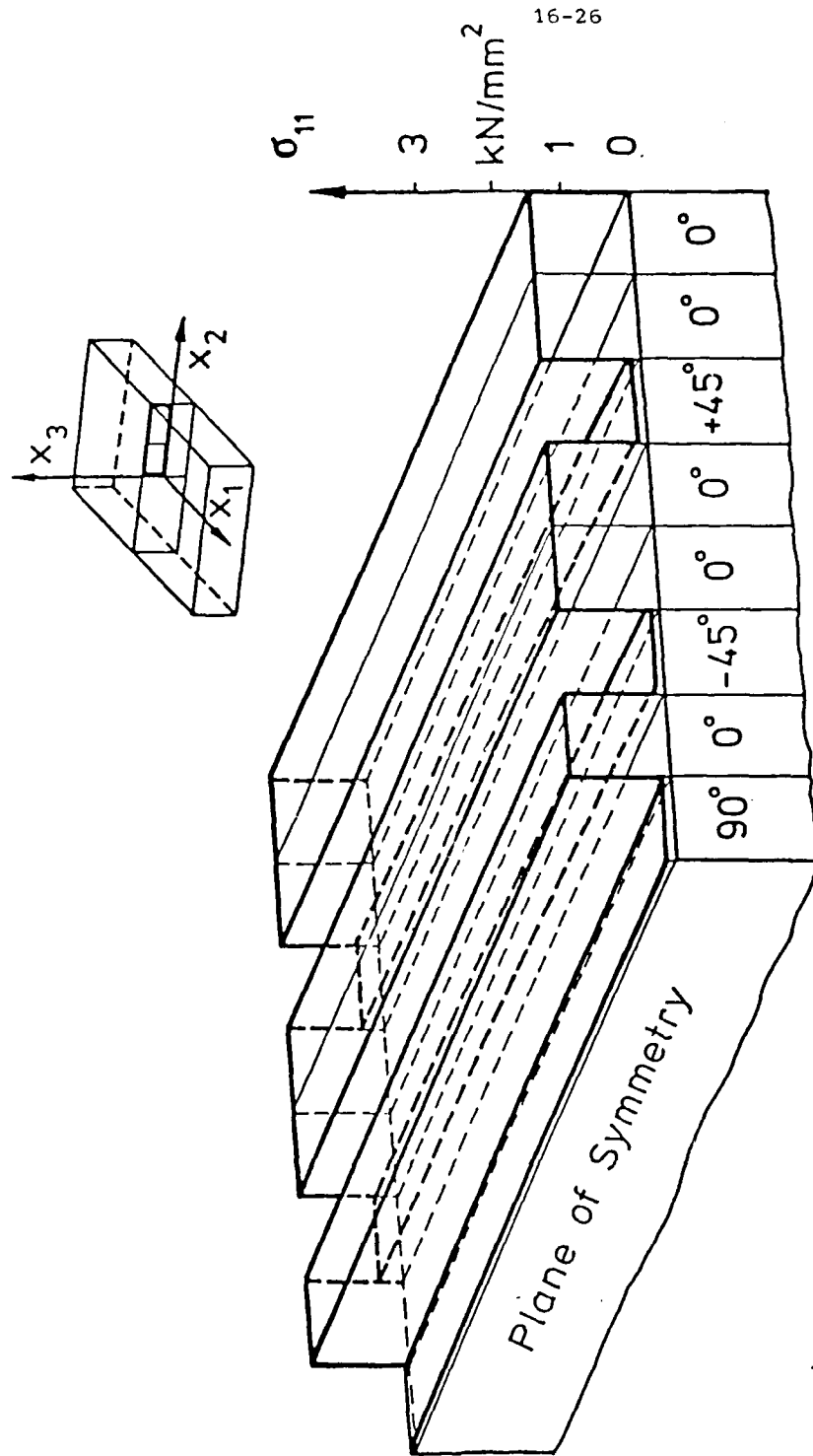


Fig. 16.14 Normal stresses σ_{11} in individual layers resulting from far field stress $\sigma'_x = 1000 \text{ N/mm}^2$.

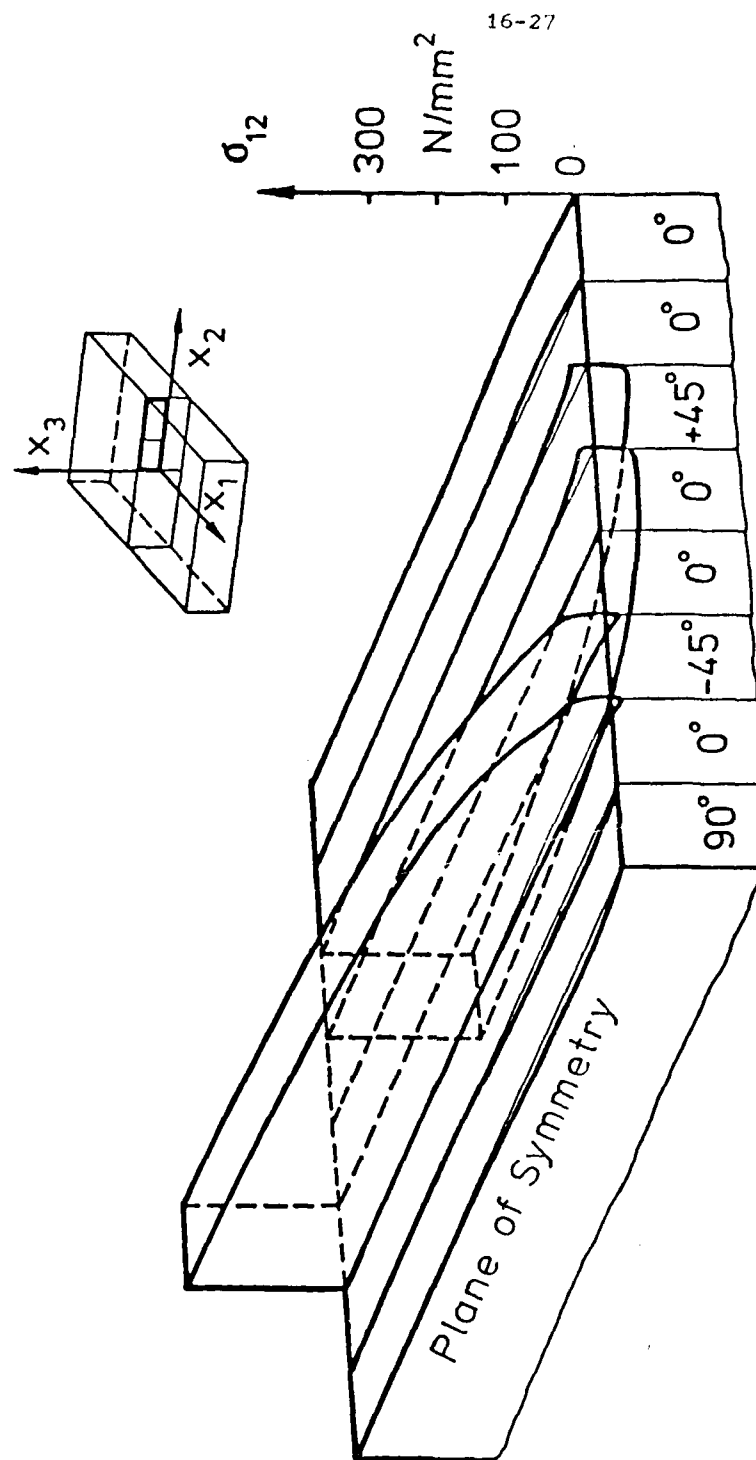


Fig. 16.15 Shear stress σ_{12} resulting from far field stress $\sigma_x = 1000 \text{ N/mm}^2$.

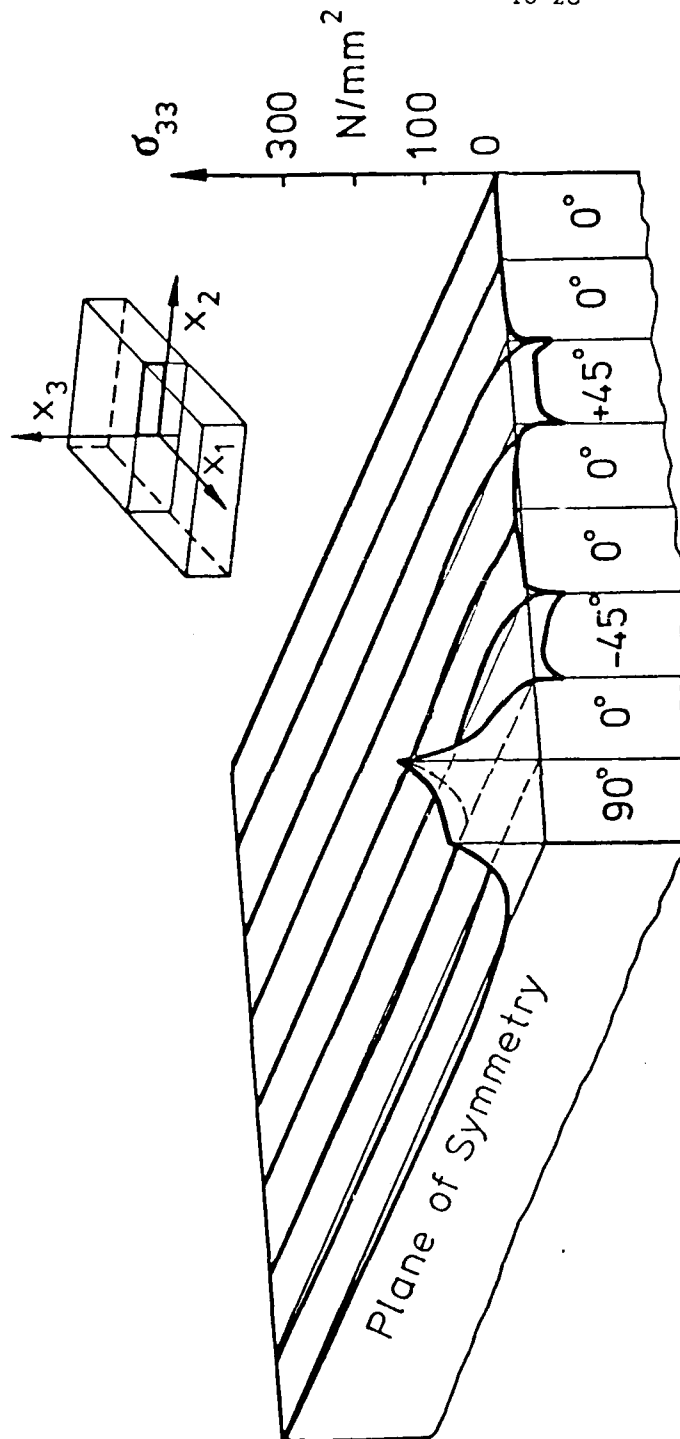


Fig. 16.16 Shear stress σ_{33} resulting from far field stress $\sigma_x = 1000$ N/mm².

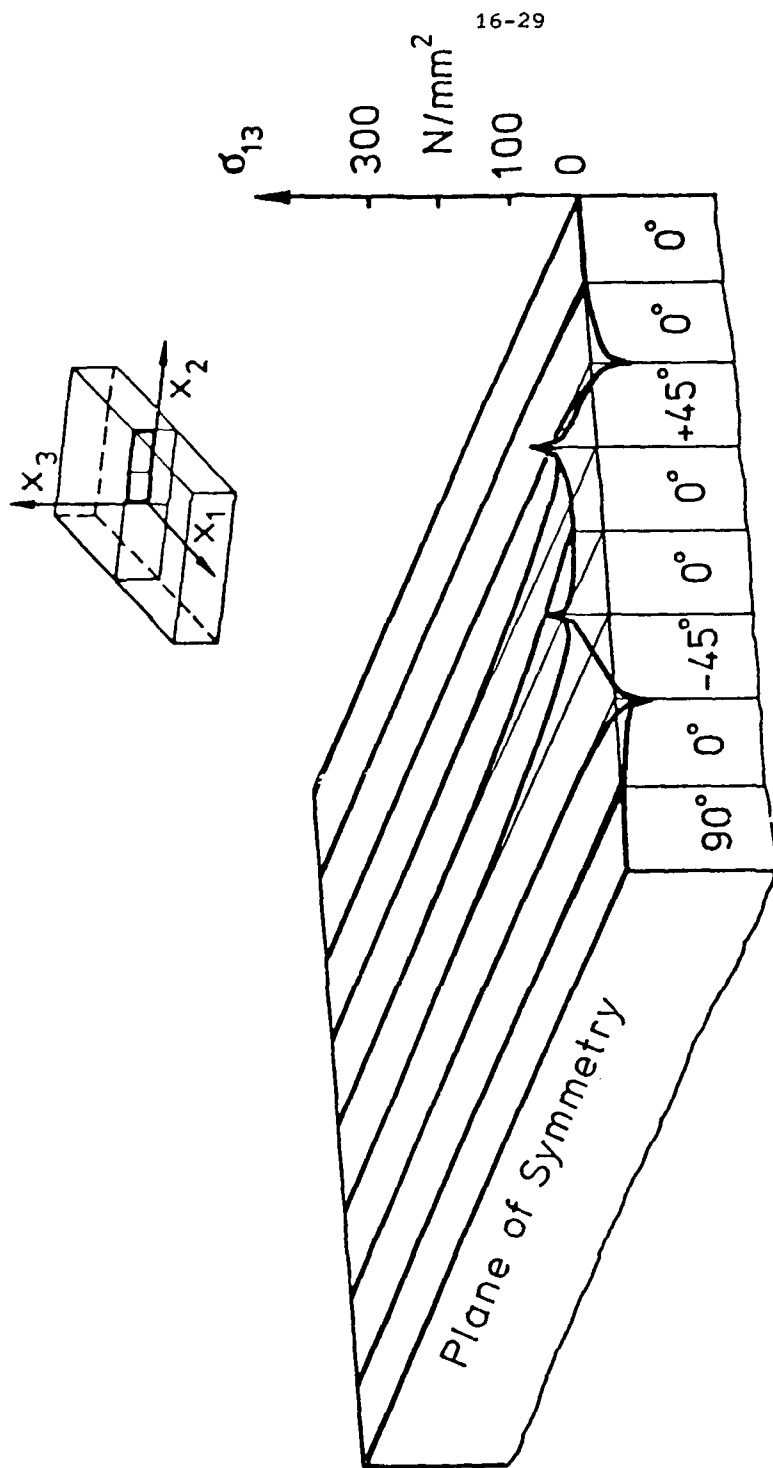


Fig. 16.17 Shear stress σ_{13} resulting from far field stress $\sigma_x = 1000 \text{ N/mm}^2$.

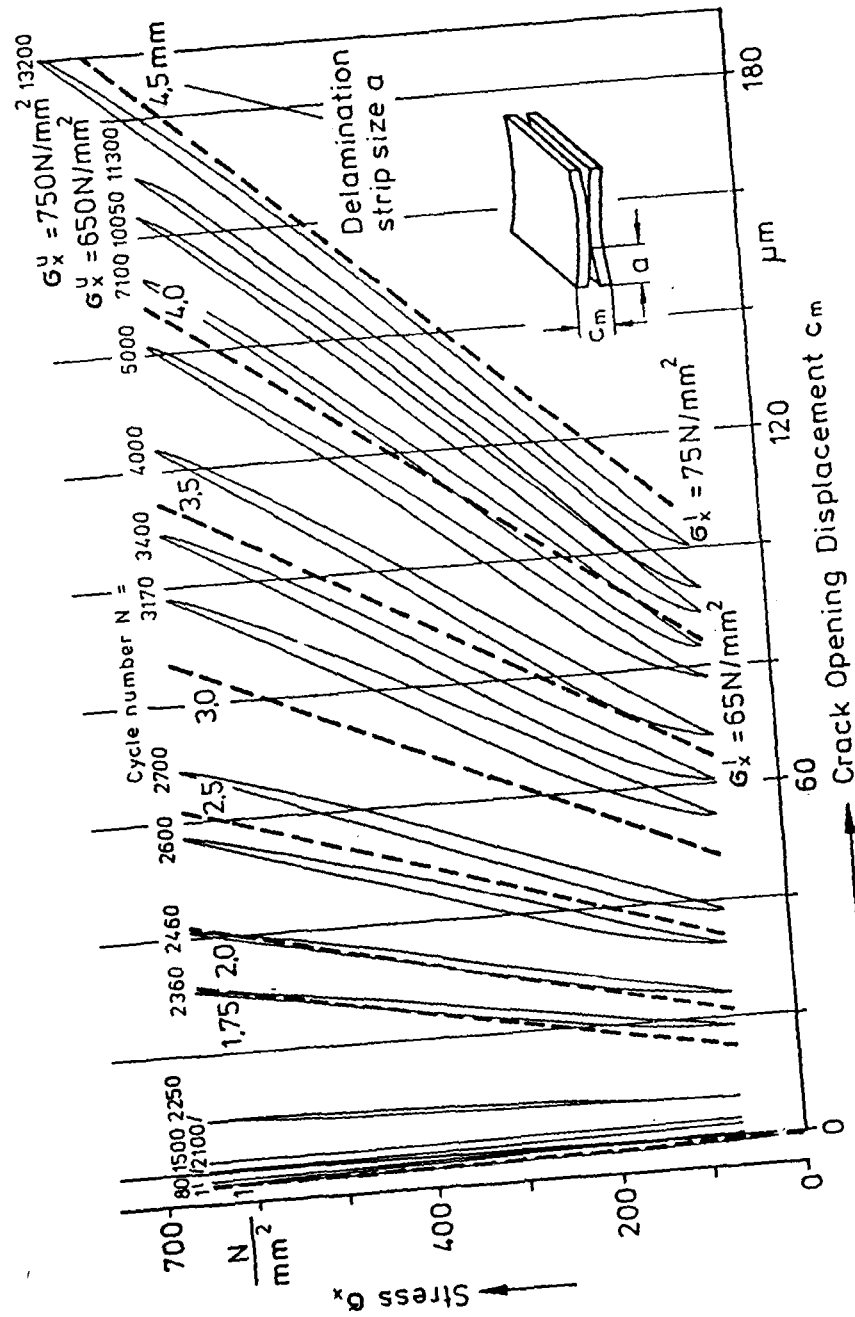


Fig. 16.18 Measured and calculated stress-displacement response.
 Calculated curves — — —.

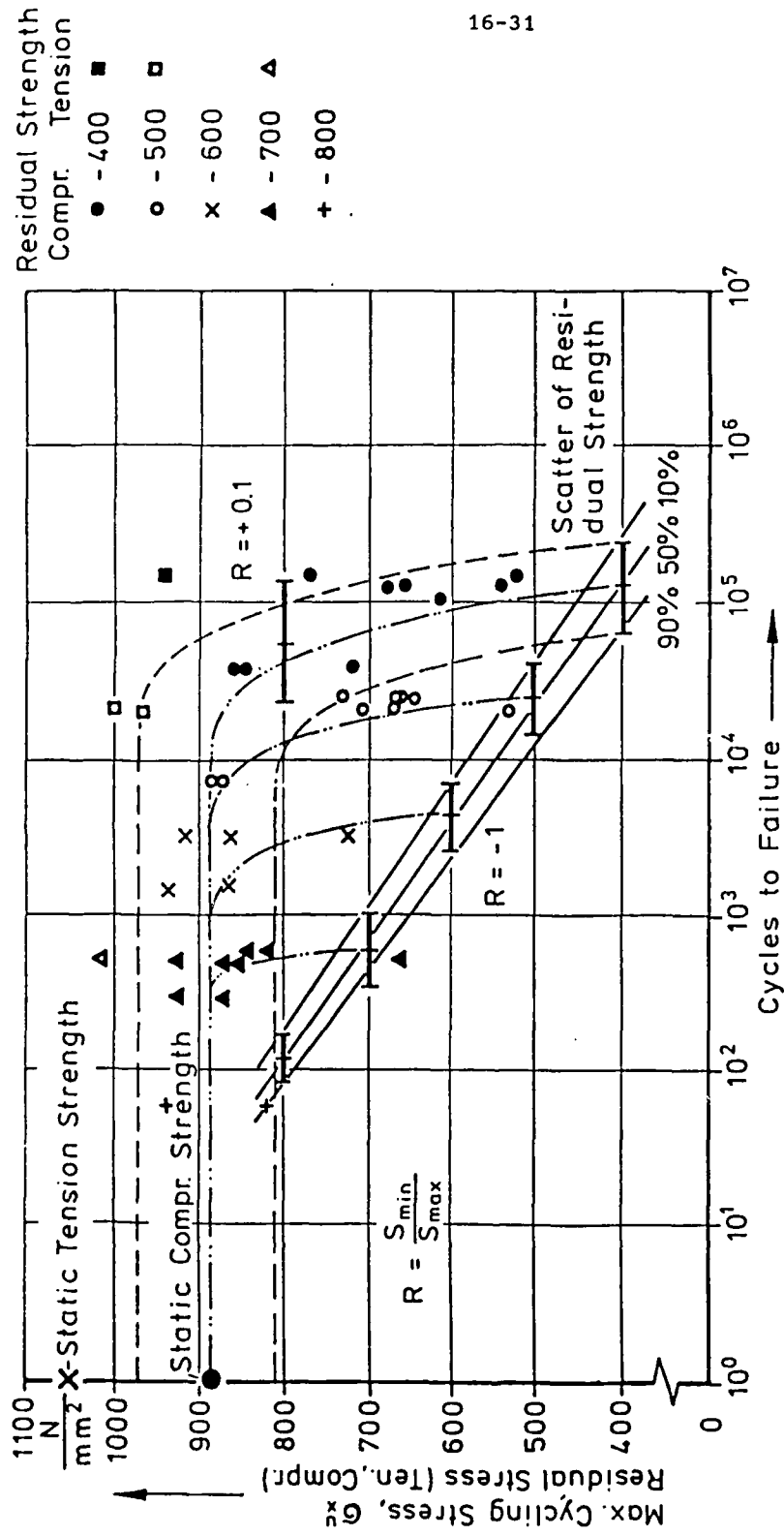


Fig. 16.19 S-N-curve and residual strength vs. cycles to failure

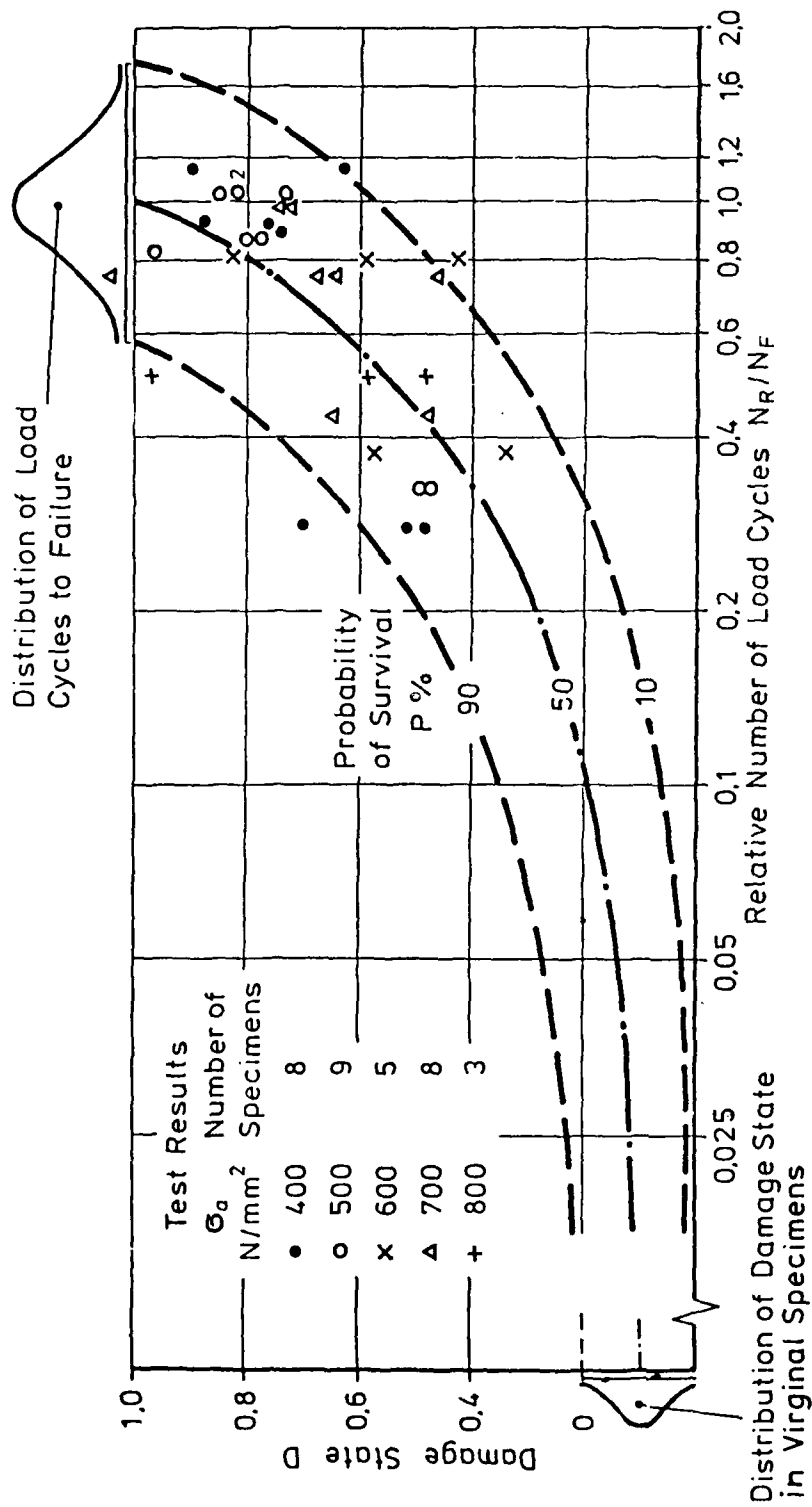


Fig. 16.20 Damage state determined from compressive residual strength.

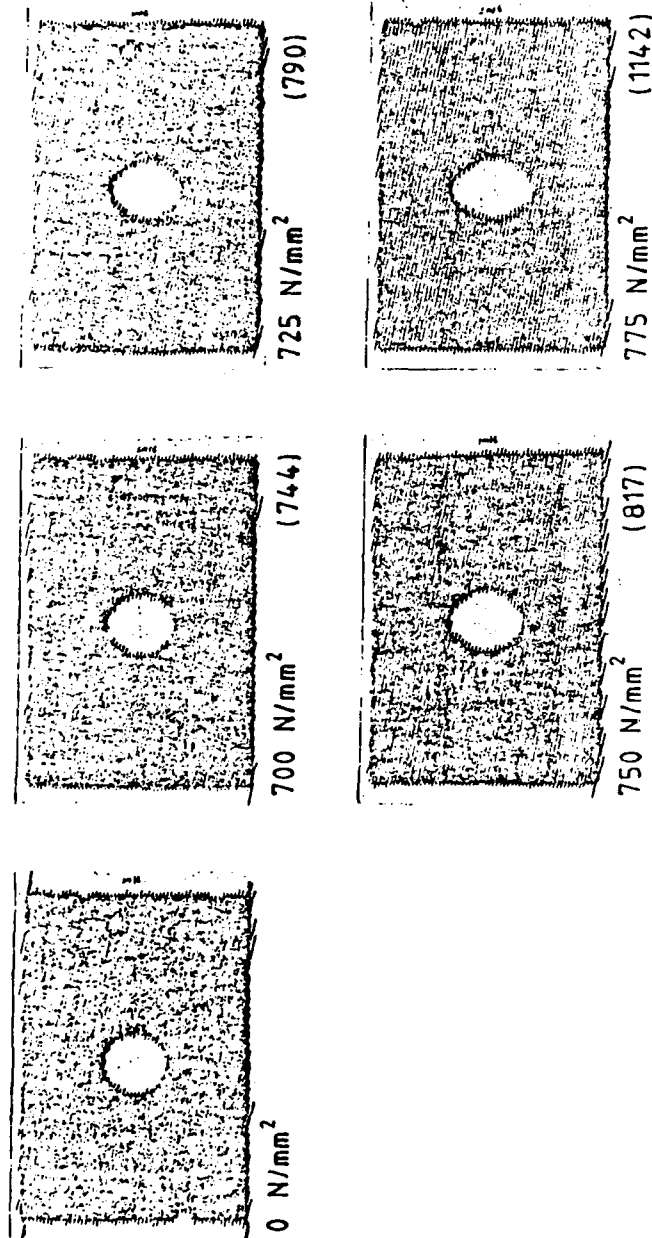


Fig. 16.21 Ultrasonic C-scans showing the growth of a delamination during compressive loading. A 0.1 mm teflon disk was placed between the 90°-plies in the midplane of the $[0_2, +45, 0_2, -45, 0, 90]_S$ -specimen.

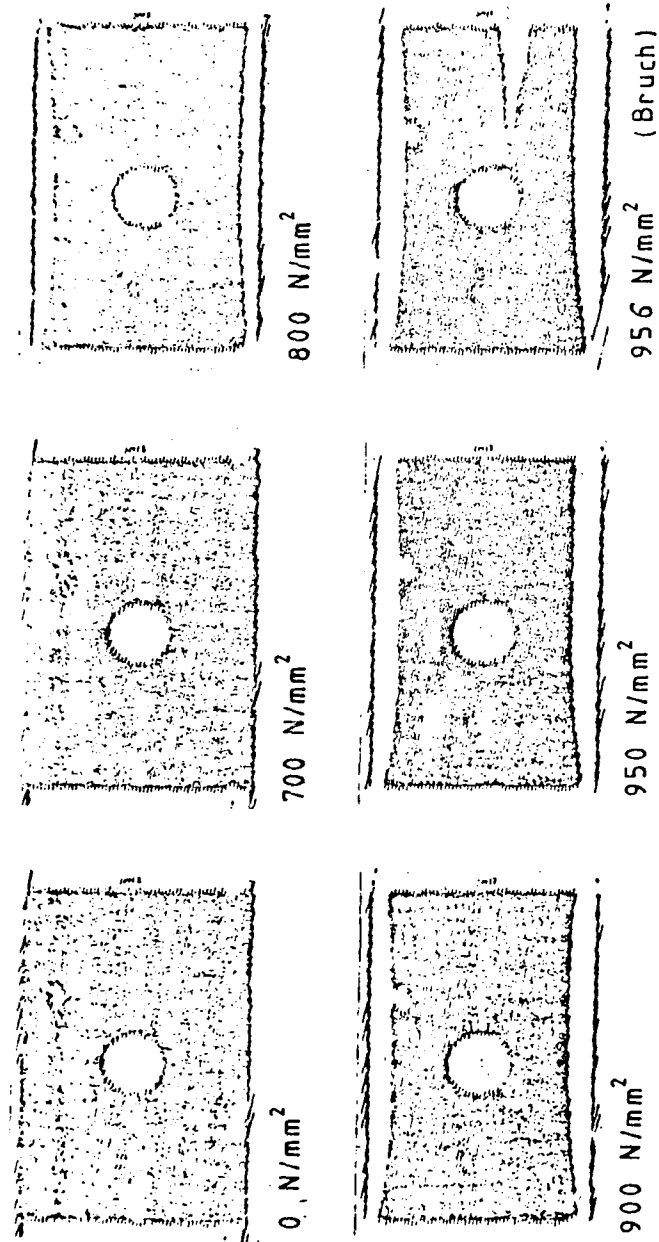


Fig. 16.22 Ultrasonic C-scans showing the delamination growth during tension loading. A 0.1 mm teflon disk was placed between the 90°-plies in the midplane of the $[0_2, +45, 0_2, -45, 0, 90]_s$ -specimen.

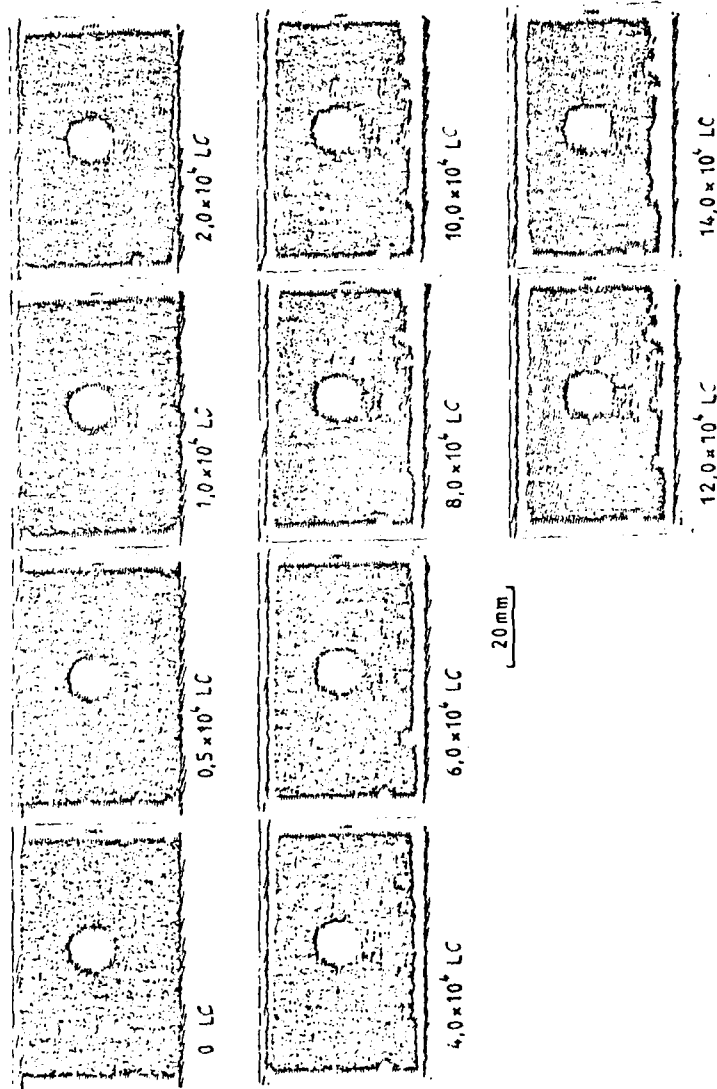


Fig. 16.23 Ultrasonic C-scans showing the delamination growth during tension-compression fatigue testing. A 0.1 mm disk was placed between the 90° -plies in the midplane of the $[0_2, +45, 0_2, -45, 0, 90]_S$ -specimen.

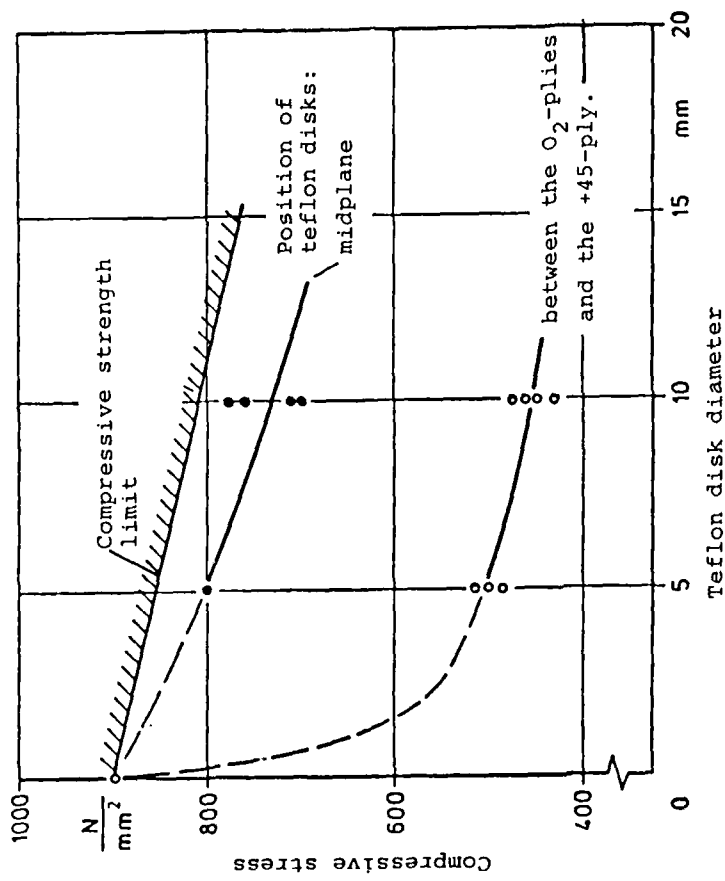
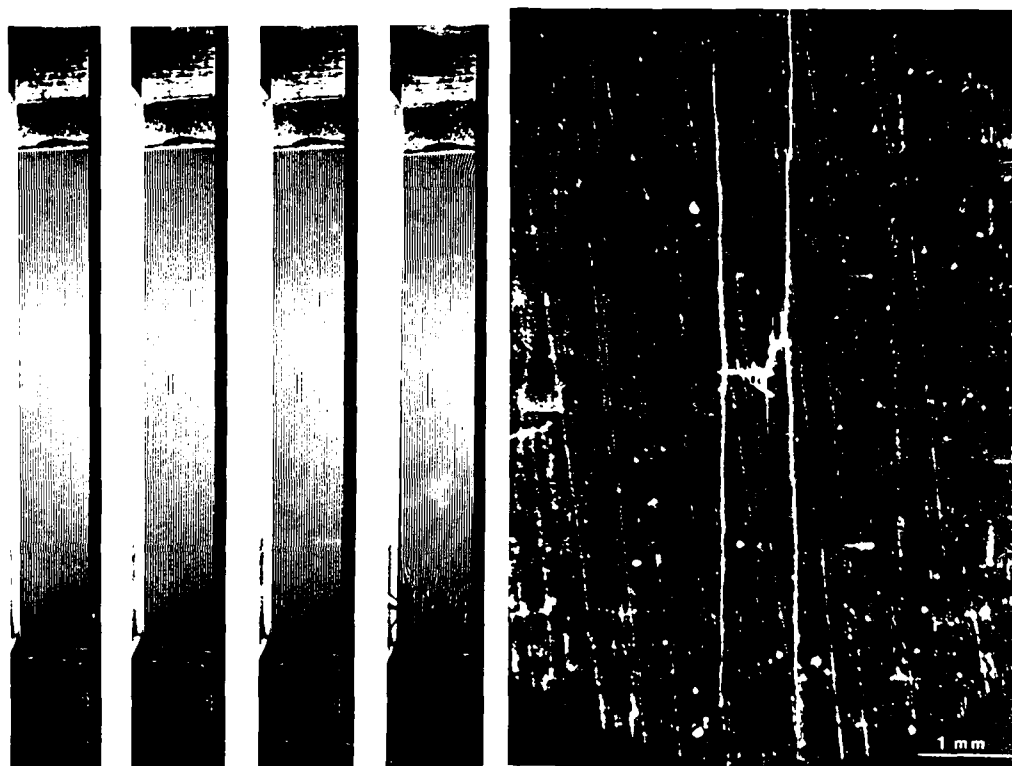


Fig. 16.24 Stress limits for the onset of progressive delamination growth during increasing compressive load. Stacking sequence $[0_2, +45, 0_2, -45, 0, 90]_s$.



a. Grid reflection showing the discontinuity of the reflection lines at the center of the sample.

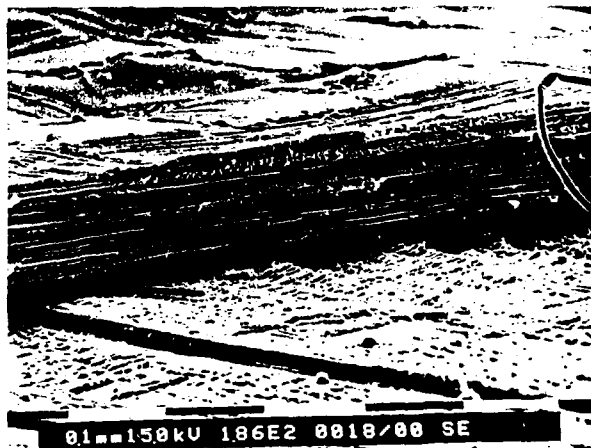
b. SEM-photograph of the broken fiber bundle.

Fig. 16.25 Local failure of a fiber bundle in the outside 0° -layer observed by grid reflection method.



Prior to Cycling

186x



After 3480 Thermal Cycles

186x

Fig. 16.26 Typical fracture areas of 914 C-specimens before and after thermal cycling.

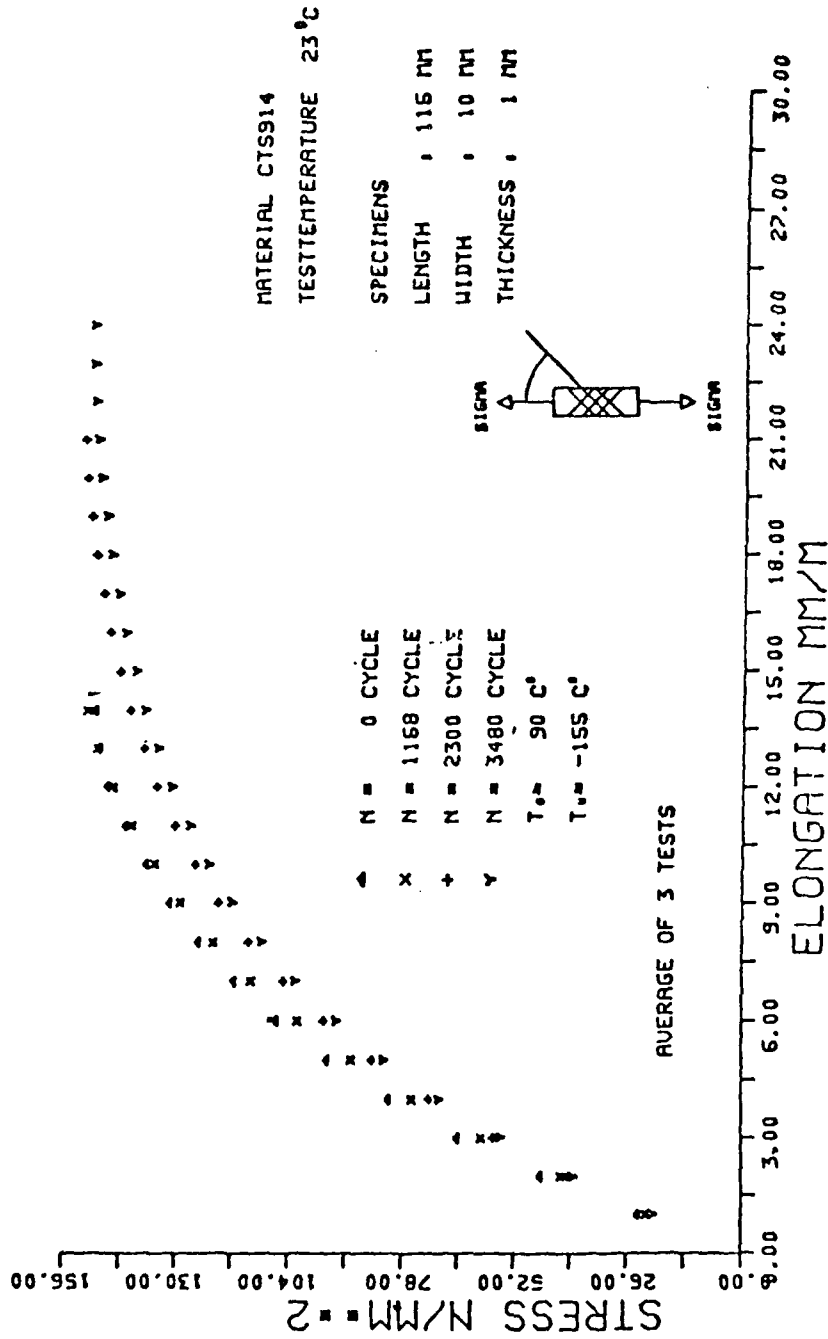


Fig. 16.27 Stress-strain curves from tension tests of $[+45^\circ]_{2s}$ specimens after thermal cycling.

END

DATE
FILMED

6 - 86